DEVELOPMENT OF DEGRADABLE POLYMERIC NANOSCOPIC PLATFORMS FOR IMAGING AND DRUG DELIVERY APPLICATIONS

A Dissertation

by

RICHEN LI

Submitted to the Office of Graduate and Professional Studies of
Texas A&M University
in partial fulfillment of the requirements for the degree of

DOCTOR OF PHILOSOPHY

Chair of Committee,	Karen L. Wooley
Committee Members,	Marcetta Y. Darensbourg
	Jodie L. Lutkenhaus
	Hong-Cai Joe Zhou
Head of Department,	Simon W. North

December 2018

Major Subject: Chemistry

ABSTRACT

Degradable polymers have gained increasing interest in the molecular probe and nanomedicine research, which avoid safety concerns of non-degradable materials after long-term accumulation in the human body. This dissertation focuses on the rational design and synthesis of biocompatible polymers, based on polyphosphoesters (PPEs) and poly(glucose carbonate)s (PGCs), which are capable of serving as non-immunotoxic antifouling coatings for molecular nanoprobes to accurately image tumors, or formulating well-defined functional nanocarriers for therapeutics to effectively treat osteosarcoma lung metastasis or bacterial infections.

In the first study, zwitterionic PPEs (zPPEs) were developed as coating materials for gold nanoparticles (AuNPs), which showed minimal immunotoxicity and advanced antifouling property. The PPE was synthesized by a rapid organocatalyzed ring-opening polymerization (ROP), followed by post-polymerization modification *via* the thiol-yne click reaction to afford the zPPEs. Degradability of the zPPEs was investigated in nanopure water (pH 5-6), which proceeded to *ca*. 75% after 2 d, and *ca*. 90% by 7 d, consistent with the degradation profiles of the zPPE-coated AuNPs. Compared to their counterparts coated with poly(ethylene glycol) (PEG), the zPPE-coated AuNPs showed similar sizes and low immunotoxicity. Moreover, significantly reduced cytokine adsorption was observed for the zPPE-coated nanoparticles. The degradability, biocompatibility and advanced antifouling property demonstrate the zPPE to be a potential PEG alternative coating material for molecular nanoprobes.

To circumvent potential drawbacks of our previous PPE system, namely the production of ethylene glycol and phosphoric acid upon hydrolytic degradation, sugar-derived PGC-based polymers were developed in the second study, which was utilized to formulate functional

nanocarriers for anticancer drugs to treat osteosarcoma (OS) lung metastases. Two PGC-based block polymers and one dimeric paclitaxel pro-drug (diPTX) were designed to be co-assembled into nanoparticles with tunable sizes and surface charges as a redox-responsive nanomedicine. The formulation showed sustained release of the PTX free drug in the presence of glutathione, a reducing agent existing at high levels in tumor tissues, thereby resulting in significant selectivity in killing cancer cells over healthy cells. Both *in vitro* and *in vivo* anticancer studies confirmed the capability of the formulation to penetrate tumor tissues and inhibit tumor cell growth, indicating its promise for the treatment of OS lung metastases.

In the third study, a novel PPE-based triblock polymer was designed and synthesized, which avoided the hydrolytic degradation product ethylene glycol, and allowed for facile construction of silver-loaded Janus nanoparticles as a potential antimicrobial. The polymer was synthesized by a one-pot sequential organocatalyzed ROP of a cyclic phosphotriester and L-lactide with PEG as the macroinitiator, followed by post-polymerization modification *via* the thiol-ene click reaction. Biocompatibility of the polymer was confirmed by cytotoxicity assays. The well-defined silver-loaded Janus nanoparticles were then prepared by simply irradiating the mixture of the PPE-based polymer and silver acetate solutions under UV for a few minutes. Within 2 h dialysis against nanopure water, *ca*. 50% of silver was released from the Janus nanoparticles, with the remaining silver released in a much slower manner over 40 h, which could be beneficial in treatment of bacterial infections.

DEDICATION

To my family and friends

ACKNOWLEDGEMENTS

I would like to thank my Ph.D. advisor Prof. Karen L. Wooley, for her great guidance, support, encouragement and patience in my graduate study at Texas A&M University. From her I have learnt tremendous knowledge and techniques for the chemistry research, and great passion and dedication for science. Without her helpful advice this work could not have been accomplished. It was great experience to study and work in her group, and I feel fortunate and proud to be one of her students.

I would also like to thank my committee members, Prof. Marcetta Y. Darensbourg, Prof. Jodie L. Lutkenhaus, and Prof. Hong-Cai Joe Zhou for their valuable advice and support throughout the course of this research.

I would thank Prof. Yongjian Liu at Washington University and his lab member Dr. Gyu Seong Heo, for the insightful discussions and great collaboration on the nanoparticle coating material project. The collaboration with Prof. Gamal Akabani and his lab members, Ryan Clanton, Soleil Hernandez, Andrew Butters at Texas A&M University, and Dr. Ronan MacLoughlin at the Aerogen, Ltd and Trinity College from Ireland on the osteosarcoma lung metastasis project is also acknowledged.

I would like to thank Dr. Fuwu Zhang for his great mentorship and help. I have also learnt tremendous knowledge from the collaboration with Dr. Lu Su, Mr. Justin Smolen, and Dr. Mahmoud Elsabahy. I would appreciate all the past and current Wooley group members for the helpful and friendly environment they created.

Finally, I would like to thank my family for their love, understanding and support.

CONTRIBUTORS AND FUNDING SOURCES

Contributors

This dissertation was supervised by a committee of researchers at Texas A&M: Prof. Karen L. Wooley (advisor) of the Departments of Chemistry, Chemical Engineering, and Materials Science & Engineering; Prof. Marcetta Y. Darensbourg (committee member) of the Department of Chemistry; Prof. Jodie L. Lutkenhaus (committee member) of the Departments of Chemical Engineering; Prof. Hong-Cai Joe Zhou (committee member) of the Departments of Chemistry, and Materials Science & Engineering.

In Chapter II, biological studies were performed with the help of Dr. Mahmoud Elsabahy and Sarosh Khan of the Department of Chemistry. Transmission electron microscopy, dynamic light scattering, atomic force microscopy experiments were conducted in part by Ms. Yue Song, Mr. Hai Wang, Dr. Lu Su, Dr. Rachel A. Letteri, and Dr. Guorong Sun of the Department of Chemistry. The functional poly(ethylene glycol) was designed and provided by Dr. Gyu Seong Heo and Dr. Yongjian Liu of the Department of Radiology, Washington University.

In Chapter III, synthesis of monomers and polymers were performed with the help of Dr. Lu Su. Biological studies were performed with the help of Mr. Justin Smolen and Ms. Sarosh Khan. The mouse nose-only nebulization system was designed by Dr. Akabani's group (Mr. Ryan Clanton, Ms. Soleil Hernandez, Mr. Andrew S. Butters, and Dr. Gamal Akabani) of Departments of Nuclear Engineering, Veterinary Integrative Biosciences and Texas A&M Institute for Preclinical Studies, Texas A&M University, which was in collaboration with Aerogen, Ltd (Dr. Ronan MacLoughlin). Dynamic light scattering, high performance liquid chromatography, Fourier transform infrared spectroscopy, and transmission electron microscopy

experiments were conducted in part by Dr. Fuwu Zhang, Mr. Yen-Nan Lin, Ms. Yue Song, Mr. Hai Wang, and Dr. Jingwei Fan of the Department of Chemistry.

In Chapter IV, cytotoxicity studies were performed with the help of Ms. Sarosh Khan. Transmission electron microscopy, inductively coupled plasma mass spectrometry, dynamic light scattering experiments were performed in part by Dr. Lu Su, Mr. Hai Wang, Ms. Yue Song, Dr. Fuwu Zhang, Mr. Yen-Nan Lin, Ms. Mei Dong, and Dr. Jingwei Fan of the Department of Chemistry. Insightful advice on the design of chemical structures and experiments were provided by Dr. Lu Su, Dr. Fuwu Zhang, and Dr. Shiyi Zhang of the Department of Chemistry.

All other experiments were carried out independently by the student.

Funding Sources

The work in Chapter II was supported by the National Science Foundation (CHE-1610311, and DMREF-1629094), and the Welch Foundation through the W. T. Doherty-Welch Chair in Chemistry (A-0001).

The work in Chapter III was supported by the National Science Foundation (CHE-1610311), and the Welch Foundation through the W. T. Doherty-Welch Chair in Chemistry (A-0001).

The work in Chapters IV was supported by National Heart Lung and Blood Institute of the National Institutes of Health as a Program of Excellence in Nanotechnology (HHSN268201000046C), the National Science Foundation (DMR-1105324, DMR-1309724, CHE-1610311 and DMREF-1629094), and the Robert A. Welch Foundation through the W. T. Doherty-Welch Chair in Chemistry (A-0001).

The contents are solely the responsibility of the authors and do not necessarily represent the official views of the National Science Foundation, the Welch Foundation, or Texas A&M University.

NOMENCLATURE

AFM	Atomic force microscopy
ATR-IR	Attenuated total reflectance infrared spectroscopy
$CDCl_3$	Deuterated chloroform
CuAAC	Copper(I)-catalyzed azide-alkyne cycloaddition
DCM	Dichloromethane
DLS	Dynamic light scattering
DMF	*N*,*N*-Dimethylformamide
DMSO	Dimethyl sulfoxide
D_2O	Deuterium oxide
DSC	Differential scanning calorimetry
EPR	Enhanced permeability and retention
FT-IR	Fourier transform infrared spectroscopy
HPLC	High performance liquid chromatography
ICP-MS	Inductively coupled plasma mass spectrometry
M_n	Number-average molar mass
MWCO	Molar mass cutoff
NIR	Near-infrared
NMR	Nuclear magnetic resonance spectroscopy
PBS	Phosphate buffered saline
PEG	Poly(ethylene glycol)
PGC	Poly(glucose carbonate)
PTX	Paclitaxel

ROP	Ring-opening polymerization
TBD	1,5,7-Triazabicyclo[4.4.0]dec-5-ene
TEA	Triethyl amine
TEM	Transmission electron microscopy
T_g	Glass transition temperature
TGA	Thermogravimetric analysis
THF	Tetrahydrofuran
UV	Ultraviolet

TABLE OF CONTENTS

Page

LIST OF FIGURES

Page

CHAPTER I

INTRODUCTION

Nanoparticles have been extensively investigated for biomedical applications in disease diagnosis and therapeutic delivery, due to their unique characteristics associated with the nanoscale sizes, such as high surface-to-volume ratios, tunable nanostructures, and optimal physical and chemical properties.[1-5] By labeling with imaging agents, such as near-infrared (NIR) dyes and radioactive isotopes, nanoparticles are capable of serving as molecular nanoprobes for accurate diagnosis after they are accumulated in the diseased sites of the human body. Nanomedicine has also shown great potential for the treatment of a wide range of diseases. Compared to free drugs, nanocarriers can offer many advantages, including protection of the drug from degradation, prevention of the drug from premature interactions with the biomolecules, and improvement of the pharmacokinetic and tissue distribution profiles of the drug. One of the advantages of molecular nanoprobes and nanomedicine is the enhanced permeability and retention (EPR) effect, which is an important benefit of nanoscopic agents in cancer diagnosis and therapy. The EPR effect results from the extravasation of nanoparticles through tumor blood vessels into the tumor interstitial space due to the high permeability of the tumor vasculature. The nanoparticles will then remain and accumulate in the tumor because of the compromised lymphatic filtration. In comparison to low-molar-mass agents, which are not retained in the tumor because of their diffusion back to circulation, nanoparticles show selectivity for tumors over normal organs and tissues, thereby leading to increased efficacy and reduced side effects. In addition to passive targeting, active targeting of molecular nanoprobes and nanomedicine can be realized by the introduction of target ligands. Targeted nanoparticles are responsive to

biomarkers on the diseased tissue cells or pathogens, which is able to increase treatment efficacy and minimize the off-target effects in the non-targeted organs. Yet, recently, the biomedical research of nanoparticles has drawn a few concerns, including high costs arising from the sophisticated structures, relatively low outcome in the efficacy improvement, and possible batch-to-batch variations.[6] Therefore, development of nanoplatforms with enhanced chemical and physical properties from facile and well-controlled approaches is highly desirable.

Rapid construction of nanoparticles can be realized through the assembly of amphiphilic polymers, with their structures finely designed and tuned to introduce versatile functionalities and achieve desirable properties.[7] Moreover, polymers can be also be utilized as the coating materials to stabilize inorganic nanostructures, combining the advantages of both the organic polymeric coatings and inorganic metal cores to formulate advanced hybrid materials. Degradable polymers, such as polyesters,[8] polypeptides,[9] polyphosphoesters (PPEs),[10-11] and polycarbonates,[12] have gained increasing interest in biomedical applications, which are capable of avoiding safety concerns of non-degradable materials after long-term accumulation in the human body. PPEs are biocompatible, degradable and structurally similar to biomacromolecules, which have been applied for rapid construction of diverse functional nanostructures as gene and drug delivery systems. Our group has developed a series of PPEs to formulate nanoparticles for drug delivery applications, with their degradability, biocompatibility, versatile functionality, and facile and controlled synthetic approaches.[13-19] Rational design and optimization of the chemical structures of PPEs have been conducted, which are further investigated on their applications in tumor imaging and drug delivery. Recently, functional glucose-derived PGCs are also employed by our group to construct nanostructures with tunable sizes, surface charges, and morphologies, and that are, notably, capable of degradation into natural products, *e.g.*, glucose, carbon dioxide,

ethanol.[20] The PGC-derived nanostructures as nanocarriers were expected to circumvent potential drawbacks of our previous PPE system, namely the production of ethylene glycol and phosphoric acid upon hydrolytic degradation, while maintaining the advantages. Ring-opening polymerization (ROP) is a facile, highly repeatable, and well-controlled technique to obtain these polymers. Organocatalysts have been reported by many groups to be able to promote ROPs of cyclic monomers, including esters, phosphoesters, and carbonates, which will eliminate the use of traditional environmentally sensitive metallic catalysts and leave no residual metal contaminants. The organic catalysts, 1,8-diazabicyclo[5.4.0]undec-7-ene (DBU), and 1,5,7-triazabicyclo[4.4.0]dec-5-ene (TBD), have been applied for the preparation of polymers in this dissertation. Click chemistry is a class of highly selective and bioorthogonal reactions that yields no side products under a variety of mild reaction conditions. The click-type reactions have been utilized to conveniently install specific functionalities and charges to the polymers under investigation.

Despite the rapid development of modern pharmaceutical research, cancers and bacterial infections remain great threats to human lives globally.[21] Cancer is reported by the World Health Organization (WHO) to be the second leading cause of deaths worldwide, resulting in *ca*. 9.6 million deaths in 2018.[22] It is estimated that 1 in 6 deaths globally is due to cancer. Bacterial infection is another cause for significant morbidity or mortality if not properly treated.[23] Antimicrobial resistance developed by bacteria is one of the key factors for the treatment failures and increased severity of infections. According to the Centers for Disease Control and Prevention (CDC) of the United States, more than two million patients are infected with antibiotic-resistant bacteria each year, which directly results in at least 23000 deaths nationwide, with an estimated direct and indirect cost of 55 billion dollars.[24-25] Therefore, the development

of novel therapeutics and strategies for the diagnosis and treatment of cancers and bacterial infections are of critical need. One of our target diseases is osteosarcoma (OS), which is the most common primary cancer of bone in children and adolescents aged 10-20 years and the third most common cancer overall in adolescents, with no proven etiology and a high fatality rate (70% survival at 5 years for non-metastatic patients, and less than 30% for those presenting with metastasis).[26-28] The predominant site of metastasis is the lung, followed by other bones. Once micrometastases grow into recurrent, overt disease, tumors are often resistant to conventional chemotherapy, and unresectible recurrent disease is fatal. Therefore, there is a pressing need to develop effective approaches to the prevention and treatment of the metastatic disease. Another target disease under our investigation for treatment is the pulmonary infection associated with the antibiotic-resistant bacteria, such as *Pseudomonas aeruginosa*. Lower respiratory infections are reported to be the most deadly communicable disease, leading to 3.0 million deaths in the world in 2016.[23] The increasingly serious health threat from pulmonary infections associated with the continually evolving resistant pathogens has made imperative the development of novel antimicrobials and innovative delivery strategies.

This dissertation will describe the rational design, synthesis and biomedical applications of polymers comprised of the degradable and biocompatible PPEs or PGCs. Well-defined nanoparticles were fabricated from the polymers with their unique chemical and physical properties to serve as molecular nanoprobes for tumor imaging, or to deliver the anticancer drug PTX for cancer therapy, and silver-based antimicrobials for treatment of bacterial infections. In Chapter II, a zwitterionic PPE (zPPE), specifically L-cysteine-functionalized poly(but-3-yn-1-yloxy)-2-oxo-1,3,2-dioxaphospholane (zPBYP), has been developed as a poly(ethylene glycol) (PEG) alternative coating material for gold nanoparticles (AuNPs), the most extensively-

investigated metal nanoparticulate platform towards molecular imaging, photothermal therapy, and drug delivery applications. ^{31}P NMR studies in D_2O revealed *ca*. 20% hydrolysis of the phosphoester moieties of the repeat units had occurred during the work-up and purification by aqueous dialysis at pH 3 over *ca*. 1 d, as observed by the ^{31}P signal of the phosphotriesters resonating at *ca.* -0.5 to -1.7 shifting downfield to *ca*. 1.1 to -0.4 ppm, attributed to transformation to phosphates. Further hydrolysis of side chain and backbone units proceeded to an extent of *ca.* 75% over the next 2 d in nanopure water (pH 5-6). The NMR degradation results were consistent with the broadening and red shift of the surface plasmon resonance (SPR) observed by UV-Vis spectroscopy of the zPPE-coated AuNPs in water over time. All AuNP formulations in this study, including those with citrate, PEG, and zPPE coatings, exhibited negligible immunotoxicity, as determined by cytokine overexpression in the presence of the nanostructures relative to those in cell culture medium. Notably, the zPPE-coated AuNPs displayed superior antifouling properties, as assessed by the extent of cytokine adsorption, relative to both the PEGylated and citrate-coated AuNPs. Although nanomedicines have been pursued for nearly twenty years, fundamental chemical strategies that seek to optimize both the drug and drug carrier together in a concerted effort remain uncommon, yet may be powerful. In Chapter III, two block polymers and one dimeric pro-drug molecule were designed to be co-assembled into degradable, functional nanocarriers, where the chemistry of each component was defined to accomplish important tasks. The result is a PEG-protected redox-responsive dimeric PTX (diPTX)-loaded cationic poly(D-glucose carbonate) micelle (diPTX@CPGC). These nanostructures showed tunable sizes and surface charges and displayed controlled PTX drug release profiles in the presence of reducing agents, such as glutathione (GSH) and dithiothreitol (DTT), thereby resulting in significant selectivity for killing cancer cells over healthy cells. Compared to free

PTX and diPTX, diPTX@CPGC exhibited improved tumor penetration and significant inhibition of tumor cell growth towards osteosarcoma (OS) lung metastases with minimal side effects both *in vitro* and *in vivo*. In Chapter IV, a facile, rapid and conveniently-controlled approach to synthesize silver-loaded PPE-based Janus nanoparticles is developed. A biocompatible triblock polymer, methoxy poly(ethylene glycol)-*block*-poly(2-ethoxy-4-vinyl-1,3,2-dioxaphospholane-2-oxide)-*block*-poly(L-lactide) (mPEG-*b*-PE4VP-*b*-PLLA), was designed and synthesized by a one-pot ring-opening polymerization (ROP), followed by post-polymerization modification *via* a thiol-ene click reaction. Self-assembly was investigated by directly dissolving the polymer into the MOPS buffer (pH = 7.4) to form anionic nanoparticles, which showed reduced cytotoxicity compared to previously reported PPEs. The solutions of the anionic PPE-based nanoparticles and silver acetate (10 wt% Ag relative to the polymer) were allowed to stir and irradiated under UV (365 nm, 500 μJ/cm^2). Rapid formation of snowman-like Janus nanoparticles was confirmed by TEM and AFM images, with the reaction progress controllable by the irradiation time. Within 2 h dialysis against nanopure water, *ca*. 50% of silver was released from the Janus nanoparticles, with the remaining silver released in a much slower manner over 40 h, which could be beneficial in treatment of bacterial infections.

CHAPTER II

FUNCTIONAL, DEGRADABLE ZWITTERIONIC POLYPHOSPHOESTERS AS BIOCOMPATIBLE COATING MATERIALS FOR METAL NANOSTRUCTURES*

2.1 Introduction

Metal and metal oxide (MO) nanoparticles (NPs) have been extensively explored for imaging, photothermal therapeutic, and drug delivery applications, due to their tunable photophysical properties, accessed by feasible syntheses that allow for control over their sizes and morphologies.[29-30] To improve the aqueous stability and decrease the undesirable non-specific protein adsorption (opsonization) of NPs, both of which are critical factors that affect *in vivo* fate, various hydrophilic natural and synthetic polymers have been developed and used as coating materials to construct polymer-metal/MO hybrid nanostructures through ligand displacement reactions.[31-32] Moreover, the incorporation of polymer components also provides facile pathways for introducing cell targeting and/or multimodule imaging functionalities, enabling responsive properties, and enhancing the loading and release performance of NP delivery platforms

Poly(ethylene glycol) (PEG) represents the "gold standard" polymeric coating material for polymer-metal hybrid nanostructures.[33] It has been well-established that the PEG can

* Reprinted (adapted) with permission from "Functional, degradable zwitterionic polyphosphoesters as biocompatible coating materials for metal nanostructures" by Li, R.; Elsabahy, M.; Song, Y.; Wang, H.; Su, L.; Letteri, R. A.; Khan, S.; Heo, G. S.; Sun, G.; Liu, Y.; Wooley, K. L., *Langmuir* 2018, DOI: 10.1021/acs.langmuir.8b02033. Copyright 2018 American Chemical Society.

improve NP water solubility, inhibit colloidal aggregation, and reduce the NP opsonization under physiological conditions.[34-35] However, recent research has indicated that PEGylated biomaterials could lose stealth functions and undergo accelerated blood clearance by mononuclear phagocyte system (MPS) organs after repeated doses, due to the production of anti-PEG antibodies by the immune system.[36-38] Additionally, conventional telechelic PEGs are non-biodegradable and lack feasibility for introduction of multiple functional moieties. Therefore, the development of alternative coating materials that provide comparable stabilization and stealth capabilities, evade recognition by the immune system, offer degradability, and impart functionalizable groups is highly desirable for nanoscopic polymer-metal hybrid biomaterials.

Zwitterionic antifouling polymers, *e.g.*, poly(carboxybetaine) (PCB),[39] poly(phosphorylcholine)[40-41] and poly(sulfobetaine),[42] are potential alternatives to PEG-based coatings, as they are highly resistant to nonspecific protein adsorption.[43] However, our previous results showed that, despite the comparable *in vivo* stealth properties of PCB to PEG, in certain circumstances, PCB-coated polymeric NPs could exhibit elevated immunotoxicity, in comparison with their PEGylated analogues.[44] Biodegradable polymers, such as polyesters,[8] polyphosphoesters (PPEs)[10-11, 45] and poly(glucose carbonate)s (PGCs),[46] have been studied as promising materials for biomedical applications, which reduce the potential for long-term accumulation and associated adverse effects. Our group has developed degradable zwitterionic polymers, including PPE,[19] and PGC,[20, 47] to address the immunotoxicity issues.[48] Interestingly, polymeric NPs with L-cysteine-functionalized, degradable zwitterionic PPE (zPPE)-based shells[16, 18-19] exhibited noticeably-decreased immunotoxicities, particularly after shell crosslinking. Based upon these results, we hypothesized that the utilization of zPPEs as coating materials for metal NPs would enable low immunotoxicity of resulting hybrid NPs while

maintaining the favorable antifouling properties of PCB.[49] Moreover, the cysteine-derived carboxylic acids and amines in the zPPE corona provide opportunities for crosslinking to enhance the rigidity and stability of the composite nanomaterials.

In this report, a degradable zPPE, namely L-cysteine-functionalized poly(but-3-yn-1-yloxy)-2-oxo-1,3,2-dioxaphospholane (zPBYP), was synthesized and explored as a PEG-alternative coating material for gold NPs (AuNPs), the most extensively-investigated metal nanoparticulate platform towards molecular imaging, photothermal therapy, and drug delivery applications.[50] Although the utilized zPBYP experienced minor amounts of degradation during the purification process, its capabilities of stabilizing AuNPs, avoiding long-term accumulation by further degradation, realizing minimal immunotoxicity, and decreasing cytokine adsorption relative to AuNPs coated with PEG and citrate, were demonstrated. Our investigation also supported that the ultrasmall gold nanoclusters (AuNPs with hydrodynamic diameter < 10 nm) could be potential platforms for *in vivo* diagnostic and theranostic applications.

2.2 Materials and methods

2.2.1 Materials

Dichloromethane (DCM) and *N*,*N*-dimethylformamide (DMF) were purified by a solvent purification system (J. C. Meyer Solvent Systems, Inc., Laguna Beach, CA). Nanopure water (18 MΩ·cm) was acquired from a Milli-Q water filtration system (Millipore Co.). Phosphate-buffered saline (PBS) was purchased as a 10× solution from VWR and diluted to a concentration of 1× in nanopure water. Thioctic acid-terminated PEG (TA-PEG-OMe, 750 Da) was purchased from Quanta BioDesign, Ltd. (Plain City, OH). Other reagents were used as received from

Sigma-Aldrich, Co. (St. Louis, MO) unless otherwise noted. Dialysis membrane tubing with a molar mass cut-off (MWCO) of 3.5 kDa was purchased from Spectrum Laboratories, Inc. (Rancho Dominguez, CA) and soaked for 5 min in nanopure water at room temperature (rt) before use.

2.2.2 Instrumentation

^{1}H NMR, ^{13}C NMR and ^{31}P NMR spectra were acquired on a Varian Inova 500 spectrometer interfaced to a UNIX computer using VnmrJ software. Chemical shifts in the ^{1}H NMR and ^{13}C NMR spectra were referenced to the residual solvent resonance signals, while those in the ^{31}P NMR spectra were referenced to an external standard, 85% H_3PO_4 in D_2O. FT-IR spectra were recorded on an IR Prestige 21 system (Shimadzu Corp., Japan), equipped with an attenuated total reflectance (ATR) accessory, and analyzed using IRsolution v. 1.40 software. Ultraviolet-visible (UV-Vis) spectroscopy measurements were performed on a Shimadzu UV-2550 spectrophotometer.

Size exclusion chromatography (SEC) eluting with DMF was conducted on a Waters Chromatography, Inc. (Milford, MA) system equipped with an isocratic pump (model 1515), a differential refractometer (model 2414), and a four-column set, including a 5 μm Guard column (50 × 7.5 mm), a Styragel HR 4 5 μm DMF column (300 × 7.5 mm), a Styragel HR 4E 5 μm DMF column (300 × 7.5 mm), and a Styragel HR 2 5 μm DMF column (300 × 7.5 mm). The system was equilibrated at 50 °C in pre-filtered DMF containing 0.05 M LiBr with the flow rate set to 1.00 mL/min. Data collection and analysis were performed with Discovery32 v. 1.039.000 software (Precesion Detectors, Inc.). Molecular weights were determined relative to polystyrene standards (615-442800 Da) purchased from Polymer Laboratories, Inc. (Amherst, MA). Polymer

solutions were prepared at a concentration of *ca.* 3 mg/mL with 0.05 vol% toluene added as a flow marker, and an injection volume of 200 μL was used.

Thermogravimetric analysis (TGA) was performed under Ar atmosphere using a Mettler-Toledo model TGA/DSC 1 with a heating rate of 10 °C/min. Glass transitions (T_g) were measured by differential scanning calorimetry (DSC) on a Mettler-Toledo DSC822® (Mettler-Toledo, Inc., Columbus, OH) under $N_{2(g)}$. DSC measurements were performed with a heating rate of 10 °C/min and analyzed using Mettler-Toledo Star^e v. 10.00 software. The T_g was taken as the midpoint of the inflection tangent of the second heating scan.

Electrospray ionization mass spectrometry (ESI-MS) experiments were performed using a Thermo Scientific LCQ-DECA instrument. The sample was directly infused at a flow rate of 6 μL/min. The spray voltage was set to -4.5 kV, and the sheath gas and auxiliary gas flow rates were set to 50 and 10 arbitrary units, respectively. The transfer capillary temperature was held at 250 °C. Xcalibur 2.0 software was used for data acquisition and processing.

Inductively coupled plasma-mass spectrometry (ICP-MS) was performed on a PerkinElmer SCIEX ICP mass spectrometer ELAN DRC II, equipped with a high-speed quadrupole, dynamic reaction cell (DRC) and axial field technology (AFT) to eliminate polyatomic interference, using 1% HNO_3 as the matrix and rhodium as the internal standard. The amount of Au in each sample was determined by ICP-MS after dilution with 1% HNO_3.

High-resolution scanning transmission electron microscopy (STEM) was conducted on a FEI Tecnai G^2 F20 FE-TEM coupled with energy-dispersive X-rays (EDX), operating at a voltage of 200 kV and equipped with a Gatan CCD camera. Samples for TEM were prepared as follows: 10 μL of a dilute NP solution in nanopure water was deposited onto a carbon-coated

copper grid, and after 1 min, excess solution was quickly wicked away by a piece of filter paper, and the samples were left to dry under ambient conditions overnight.

Dynamic light scattering (DLS) measurements were conducted using a Delsa Nano C instrument from Beckman Coulter, Inc. (Fullerton, CA) equipped with a laser diode operating at 633 nm. Scattered light from 0.5 mL samples in a disposable polystyrene cell (0.9 mL capacity) was detected at 165° and averaged over 70 accumulations. The photomultiplier aperture and attenuator were adjusted automatically to obtain a photon count rate of *ca.* 10 kcps. The particle size distribution and distribution averages *(i.e.*, the intensity-, volume- and number-average hydrodynamic diameters) were calculated using CONTIN particle size distribution analysis routines in Delsa Nano 2.31 software. All measurements were repeated 10 times.

Atomic force microscopy (AFM) was performed using a Multimode 8 system (Bruker) in PeakForce® tapping mode using a ScanAsyst-Air Silicon Nitride probe (k = 0.4 N/m, f_0 = 70 kHz, Bruker). AFM images were processed with Nanoscope Analysis 8.15 software (Bruker). Samples were prepared by deposition of a solution of nanoparticles in nanopure water (50 μL, 0.2 mg/mL) onto freshly cleaved mica substrates. After 1 min, excess solution was wicked away by a piece of filter paper, and the mica surface was allowed to dry in air.

2.2.3 Experimental procedures

Synthesis of PBYP. Synthesis and characterization of the cyclic phosphotriester monomer BYP was performed according to a previously reported procedure.[19] A solution of BYP (0.9910 g, 5.631 mmol) and 3-azido-1-propanol (48.4 mg, 0.479 mmol) in anhydrous DCM (2 mL) was transferred *via* syringe into a flame-dried vial equipped with a stir bar and rubber septum under $N_{2(g)}$ at rt. A solution of organocatalyst 1,8-diazabicyclo[5.4.0]undec-7-ene (DBU)

(82.3 mg, 0.592 mmol) in anhydrous DCM (0.2 mL) was injected quickly into the vial. After stirring for 20 min, the reaction vial was opened to air, and quenched by addition of excess acetic acid. An aliquot of the reaction mixture was withdrawn and diluted with $CDCl_3$ to determine the BYP monomer conversion by ^{31}P NMR spectroscopy, by comparison of the relative integrations of the peaks at 17.97, and between -0.20 and -1.89 ppm, corresponding to cyclic and ring-opened phosphoester resonances, respectively. PBYP was purified by precipitation from DCM into diethyl ether and then dried under vacuum to afford a colorless liquid (893.6 mg, 85 % yield). ^1H NMR (500 MHz, $CDCl_3$): δ 4.47-3.93, 3.83-3.66 (m, POCH_2CH_2O, POCH_2CH$_2$C≡CH, $N_3CH_2CH_2CH_2$), 3.42 (t, N_3CH_2, J = 5.0 Hz), 2.64-2.51 (br, CH_2C≡CH), 2.18-2.02 (br, $CH_2C{\equiv}CH$), 1.92 (q, $N_3CH_2CH_2$, J = 5.0 Hz) ppm. ^{13}C NMR (126 MHz, CDCl3): δ 79.56, 70.84, 66.46, 65.82, 65.02, 47.58, 29.63, 20.64 ppm. ^{31}P NMR (202 MHz, $CDCl_3$): δ -0.2 to -1.89 ppm. FT-IR (ATR) 3700-3100, 3100-2700, 2100, 1711, 1647, 1456, 1375, 1271, 1230, 1009, 964, 800, 733 cm^{-1}. T_g = -37 °C. TGA in Ar: 170-310 °C, 57% mass loss; 310-500 C, 14% mass loss, 29% mass remaining at 500 °C. SEC (0.01 M LiBr in DMF, PS standards): M_n = 14.9 kDa, $Đ$ = 1.22.

Post-polymerization modification of PBYP with L-cysteine *via* thiol-yne reaction to afford zwitterionic PBYP (zPBYP). PBYP (941.8 mg, 5.1 mmol alkyne groups), L-cysteine (9.0595 g, 51.580 mmol), 2,2-dimethoxy-2-phenylacetophenone (DMPA, 395.0 mg, 1.541 mmol), and concentrated HCl (11.65 M, 4.4 mL, 51 mmol) were dissolved in *N*,*N*-dimethylacetamide (DMAc, 35 mL), deoxygenated under $N_{2(g)}$ for 10 min, and irradiated under UV light (365 nm) for 2.5 h with stirring. The resulting solution was transferred to dialysis tubing (MWCO 3.5 kDa) and dialyzed against nanopure water adjusted to pH 3 with HCl at 4 °C for 1 d to remove excess thiol and photoinitiator. The solution was then lyophilized to afford zPBYP as a white solid (1.3318 g, 61% yield). ^1H NMR (500 MHz, D_2O): δ 4.59-4.18 (br,

$N_3CH_2CH_2CH_2$, $POCH_2CH_2O$, $POCH_2CH_2CH$), 4.18-3.91 (br, $CH_2CH(NH_3)COOH$, $POCH_2CH_2CH$), 3.91-3.70 ($POCH_2CH_2$ in the anionic repeat units), 3.51 (t, N_3CH_2, J = 5.0 Hz), 3.40-2.61 (br, $SCHCH_2S$, $SCHCH_2S$, CH_2SCHCH_2S, $SCHCH_2SCH_2$), 2.40-2.14, 2.06-1.72 (br, $N_3CH_2CH_2$, $POCH_2CH_2CH$) ppm. ^{13}C NMR (126 MHz, CDCl3): δ 172.06, 68.02, 67.21, 66.35, 65.22, 64.50, 53.40, 47.28, 36.61, 36.21, 31.49, 29.03 ppm. ^{31}P NMR (202 MHz, $CDCl_3$): δ 1.10 to -1.70 ppm. FT-IR (ATR) 3140-2780, 2670, 2460, 1780, 1655, 1593, 1514, 1472, 1362, 1285, 1207, 1097, 991, 912, 843, 760 cm^{-1}. T_g = -64 °C. TGA in Ar: 150-200 °C, 11% mass loss; 200-400 °C, 46% mass loss, 43% mass remaining at 500 °C.

Synthesis of citrate-coated AuNP (AuNP@citrate). Into a 20 mL glass vial equipped with a stir bar, nanopure water (5 mL), $HAuCl_4$ (10 mM, 500 µL) and sodium citrate solution (20 mM in nanopure water, 500 µL) were added and allowed to stir.[51] Ice-cold, freshly-prepared sodium borohydride solution (20 mM in nanopure water, 1 mL) was then quickly added to the mixture while vigorously stirring at rt. The solution turned pink after a short time, indicative of formation of AuNPs, and was stirred for an additional 0.5 h. The AuNPs were then purified by centrifugal filtration (MWCO 10 kDa) with nanopure water three times at 3500 rpm.

Preparation of zPBYP-coated AuNP (AuNP@zPBYP). In a typical reaction, zPBYP (1.0 mg) was dissolved in 1× PBS (pH = 7.4, 1 mL). A solution of AuNP@citrate (2 mL, 0.14 mg/mL Au as determined by ICP-MS) in nanopure water was then added dropwise into the solution of zPBYP using a syringe pump over 5 min while stirring. The reaction mixture was stirred for 3 h, and the polymer-coated NPs were purified by centrifugal filtration (MWCO 10 kDa) with nanopure water three times at 3500 rpm.

Preparation of PEG-coated AuNPs (AuNP@PEG). In a typical reaction, TA-PEG-OMe (1.0 mg, 1.3 µmol) was dissolved in 1× PBS (pH = 7.4, 1.0 mL). A solution of

AuNP@citrate (2 mL, 0.14 mg/mL Au) was then added dropwise into the solution of TA-PEG-OMe using a syringe pump over 5 min while stirring. The reaction mixture was stirred for 3 h, and the PEG-coated NPs were purified by centrifugal filtration (MWCO 10 kDa) with nanopure water three times at 3500 rpm.

Preparation of shell-crosslinked zPBYP-coated AuNP (AuNP@X-zPBYP). To a solution of AuNP@zPBYP (2 mL, 0.14 mg/mL Au, 0.44 μmol of carboxylic acids, 0.44 μmol of amines), a solution of 1-[3-(dimethylamino)propyl]-3-ethylcarbodiimide methiodide (EDCI, 650 μL, 0.10 mg/mL in water) was added. The reaction was allowed to stir overnight at rt, and the crosslinked nanostructures were purified by centrifugal filtration (MWCO 10 kDa) with nanopure water three times at 3500 rpm.

Hydrolytic degradation of zPBYP. In a typical study, a lyophilized sample of zPBYP (15.1 mg) was dissolved in D_2O (0.4 mL) and transferred into an NMR tube. The sample was maintained in a New Brunswick™ Innova® 44 incubator shaker (37 ºC, 60 rpm) and characterized by ^{31}P NMR to monitor the degradation progress at predetermined times (0 h, 1 d, 2 d, 3 d, 4 d, 6 d). The study was repeated in triplicate. After 6 d, an aliquot of the sample was diluted with methanol and further characterized by ESI-MS for identification of small-molecule degradation products. The remaining sample was dialyzed against nanopure water in dialysis tubing (MWCO 1 kDa), followed by lyophilization to determine the amount of residual material retained in the dialysis tubing.

Degradation study of AuNP@zPBYP, in comparison to AuNP@citrate, AuNP@PEG, and AuNP@X-zPBYP. In a typical study, a solution of AuNP@zPBYP was kept in the incubator shaker (37 ºC, 60 rpm) and characterized by UV-Vis spectroscopy at predetermined times (0 d, 1 d, 2 d, 4 d, 6 d, and 14 d). Similarly, the stability of AuNP@citrate,

AuNP@PEG, and AuNP@X-zPBYP in the incubator shaker was evaluated by monitoring the surface plasmon resonance (SPR) over 14 d.

Cytokine multiplex assay. The multiplex assay was performed as reported previously.[49] RAW 264.7 (2×10^4 cells/well) mouse macrophages were plated in a 96-well plate in Dulbecco's Modified Eagle Medium (DMEM) (10% fetal bovine serum and 1% penicillin/streptomycin) and incubated at 37 ºC and 5% CO_2 for 24 h. The medium was then replaced with fresh medium 1 h prior to the addition of 20 µL of each of the samples (medium (control), AuNP@citrate, AuNP@zPBYP, AuNP@PEG, and AuNP@X-zPBYP (5 µg/mL Au in each sample)). After a 24 h incubation, the supernatants were collected and centrifuged for 10 min at 13000 rpm. Serial dilutions of cytokine standards (Bio-Rad Laboratories, Inc., Hercules, CA) were prepared in cell-culture medium to generate a calibration curve with which to determine cytokine concentration. The cytokine standard and cells treated with culture medium (control, 50 µL) and NPs (50 µL) were incubated with antibody-conjugated magnetic bead solution (50 µL) for 30 min in the dark. After washing, the detection antibody solution (50 µL) was added to the wells and incubated in the dark for 30 min under continuous shaking (300 rpm). After washing, streptavidin-phycoerythrin solution (50 µL) was added to each well and incubated while protected from light for 10 min under continuous shaking (300 rpm). Finally, after several cycles of washing, re-suspension in the assay buffer and shaking, the expression of the mouse cytokines, interleukin (IL)-1α, IL-1β, IL-2, IL-3, IL-4, IL-5, IL-6, IL-9, IL-10, IL-12 (P40), IL-12 (P70), IL-13, IL-17, eotaxin, granulocyte-colony-stimulating factor (G-CSF), granulocyte macrophage-colony stimulating factor (GM-CSF), interferon-γ (IFN-γ), keratinocyte-derived chemokine (KC), monocyte chemotactic protein (MCP)-1, macrophage inflammatory protein (MIP)-1α, MIP-1β, regulated upon activation normal T-cell expressed and presumably secreted (RANTES) and

tumor necrosis factor-α (TNF-α) were measured immediately using a Bioplex 200 system, equipped with high-throughput fluidics (HTF) and a Pro II Wash station, and the data were analyzed using Bioplex Data Pro software. Cytokine expression was reported relative to that by cells in culture medium.

Cytokine adsorption assay. Adsorption of the mouse cytokines, IL-1α, IL-1β, IL-2, IL-3, IL-4, IL-5, IL-6, IL-9, IL-10, IL-12 (P40), IL-12 (P70), IL-13, IL-17, Eotaxin, G-CSF, GM-CSF, IFN-γ, KC, MCP-1, MIP-1α, MIP-1β, RANTES and TNF-α onto the AuNPs, was measured using a Bioplex 200 system equipped with HTF and a Pro II Wash station. Specific concentrations of the cytokine standards were determined either in cell culture medium (DMEM) or when mixed with the various NPs (5 μg/mL) in the same medium, as described previously.[44, 52] The values are reported in Figure 6 as the ratio of the cytokine concentration in the cytokines/NP mixtures to that in samples without NPs treated and subjected to the same rinsing procedures.

2.3 Results and Discussion

2.3.1 Design and synthesis of the zwitterionic polyphosphoester, zPBYP

The zPBYP was designed as an alternative AuNP coating material to PEG, with zwitterions in the side chains to prevent biofouling and undesired immune system responses, and an azide group at the chain end to enable attachment of drugs, targeting moieties, and imaging agents (Figure II.1). A PPE backbone was selected due to its previously reported biocompatibility, degradability, and chemical versatility.[19] The chain length was set to be relatively short, with a target degree of polymerization (DP_n) of 12, to allow comparison with the

previously-reported TA-PEG-OMe (DP_n = 12), which stabilized ultrasmall NPs, with number-average hydrodynamic diameters ($D_{h(number)}$) < 10 nm postulated to promote effective renal clearance *in vivo*.[53] The azide group on the chain end, while not utilized in this work, provides opportunities for further modification of the polymer *via* azide-alkyne click reactions to expand the utility and scope of the NPs.

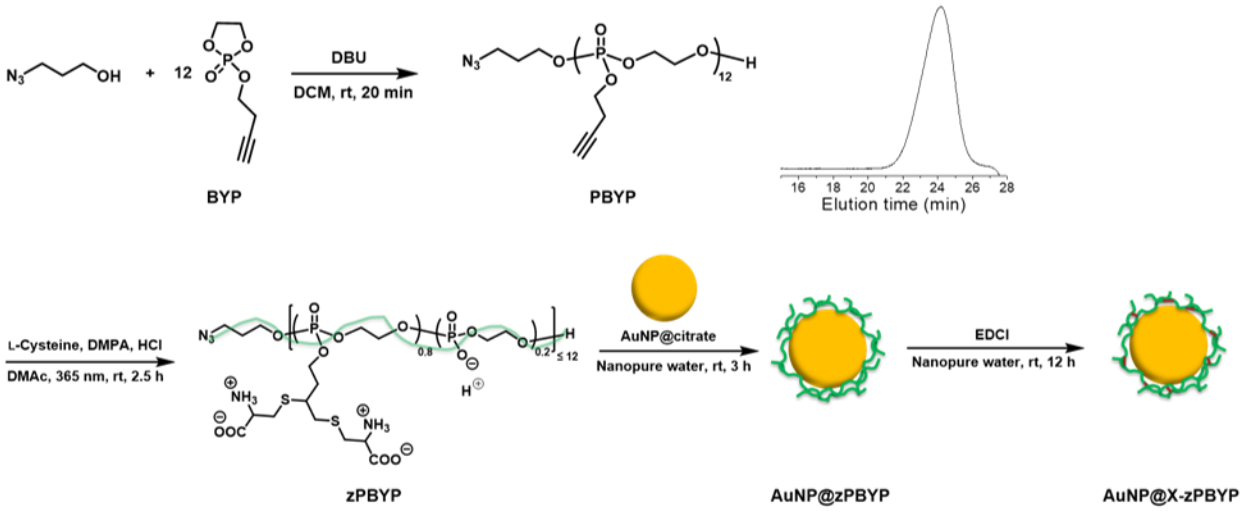

Figure II.1. Synthesis of PBYP, followed by post-polymerization modification *via* a thiol-yne click reaction with L-cysteine to yield the zwitterionic polyphosphoester zPBYP, and the subsequent preparation of AuNP@zPBYP and AuNP@X-zPBYP. Inset: SEC trace of PBYP in DMF.

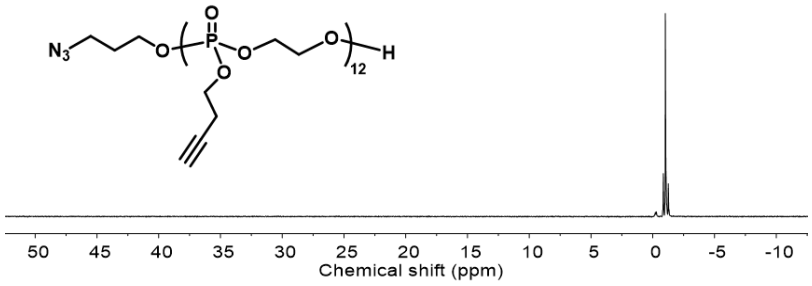

Figure II.2. ^{31}P NMR (202 MHz, $CDCl_3$) spectrum of PBYP.

The alkyne-functionalized homopolymer PBYP was synthesized by rapid organocatalyzed ring-opening polymerization (ROP) of the cyclic phosphotriester monomer BYP at rt in DCM with 3-azidopropanol as the initiator and DBU as the organocatalyst (Figure II.1). After 20 min, the reaction was quenched by addition of excess acetic acid. The ^{31}P NMR spectrum of the reaction aliquot showed almost complete conversion of the single cyclic monomer signal (resonating at 18.0 ppm) to several polymer ^{31}P resonance frequencies (between -0.2 to -1.9 ppm) (Figure II.2). Size exclusion chromatography (SEC) of the purified product (Figure II.1 inset) revealed a monomodal molar mass distribution with relatively narrow dispersity ($Đ$ = 1.22), consistent with the controlled character of organocatalyzed ROP to yield well-defined polymers. The number-average molar mass (M_n) and degree of polymerization (DP_n) were calculated from the ^{1}H NMR spectrum of PBYP (Figure II.3), by comparing the integration of the proton resonances from the initiator (3.4 ppm) with those of the polymer side chain proton resonances (2.6 - 2.5 ppm).

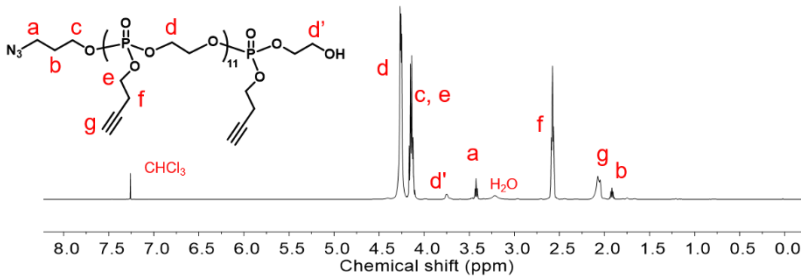

Figure II.3. ^{1}H NMR (500 MHz, $CDCl_3$) spectrum of PBYP.

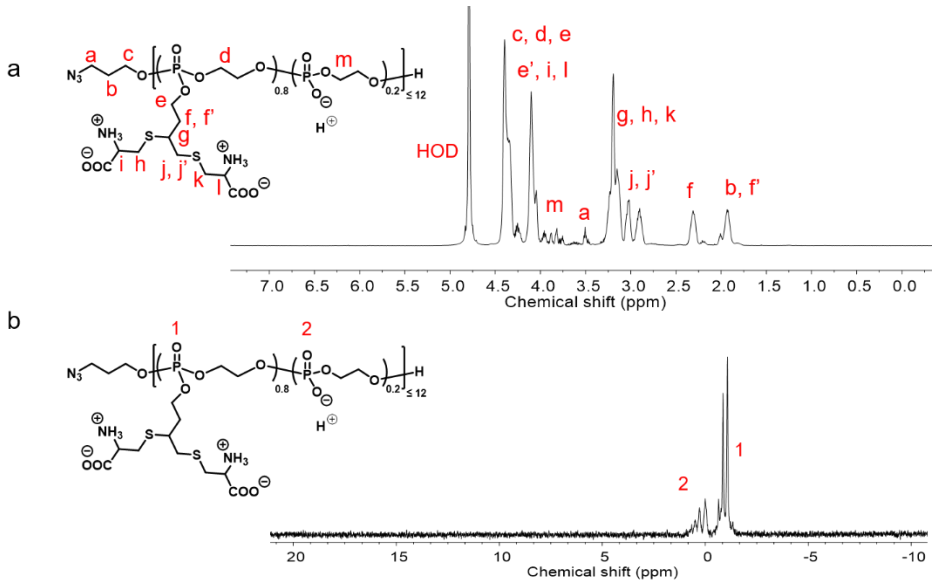

Figure II.4. NMR spectroscopy of zPBYP in D_2O: (a) ^{1}H NMR (500 MHz) and (b) ^{31}P NMR (202 MHz) spectra.

The zwitterionic polymer, zPBYP, was synthesized by post-polymerization modification of PBYP *via* photoinitiated thiol-yne click reaction of PBYP with excess L-cysteine (10 eq. relative to alkyne groups), as shown in Figure II.1. The similar solubility of L-cysteines and zPBYP in a variety of solvents rendered purification by precipitation unfeasible, therefore, the reaction mixture was dialyzed against water acidified with HCl (pH = 3) at 4 °C for 1 d to remove excess thiol and photoinitiator, then lyophilized to afford zPBYP as a white solid in 61% yield. The appearance of signals for protons adjacent to the L-cysteine sulfur atom, resonating between 3.5 and 2.8 ppm, and the disappearance of the alkyne proton resonances (2.2-2.0 ppm) in the ^{1}H NMR spectrum indicated quantitative consumption of the alkynes (Figure II.4a). Following purification of zPBYP, the appearance of resonances between 1.1 and -0.4 ppm in the ^{31}P NMR spectrum (Figure II.4b) indicated partial degradation, despite measures to inhibit degradation, *i.e.*, acidification of the dialysis solution to protonate the cysteine amines to reduce their

nucleophilicity. Nevertheless, given that the polymer was obtained in *ca*. 60% yield, which would presumably be substantially lower if the polymer had degraded into oligomers and been removed by dialysis, the degradation is assumed to occur predominantly by cleavage of side chains or near the chain ends. The extent of degradation was determined to be *ca.* 20%, by comparing the integration of resonances of the phosphate groups between 1.1 and -0.4 ppm to the total integration of phosphorus resonances, *i.e.*, from 1.1 to -1.7 ppm. The multiple resonances from 4.0 to 3.7 ppm in the ^{1}H NMR spectrum were assigned to the backbone protons in the anionic repeat units, consistent with our previously-reported NMR spectroscopy results on PPE ionomers.[54] While degradation of zPBYP during purification was difficult to avoid, the presence of anionic groups was not anticipated to be detrimental to the stabilization of AuNPs. Taken together, the introduction of large amounts of zwitterionic L-cysteine groups onto biocompatible and degradable PPEs yielded promising PEG-alternative coating materials, which were then investigated for their ability to stabilize AuNPs and reduce immunotoxicity (*vide infra*).

2.3.2 Synthesis of AuNPs with different coatings

Citrate-coated AuNPs (AuNP@citrate) were prepared according to literature procedures,[51] in which strong reducing agents are added to solutions of gold salts with stabilizing agents to produce small-sized AuNPs. In a typical reaction, $HAuCl_4$ and sodium citrate were mixed in nanopure water, followed by the addition of a freshly-prepared solution of $NaBH_4$ in nanopure water (cooled in an ice bath prior to use) under vigorous stirring. The solution was then allowed to stir at rt for 30 min before purification by centrifugal filtration. Consistent with literature reports,[55-56] a characteristic absorption peak was observed in the UV-Vis spectrum

(Figure II.5, black trace) of AuNP@citrate at 510 nm, corresponding to the SPR of AuNPs. TGA showed minimal mass loss for AuNP@citrate upon heating up to 500 °C under Ar (Figure II.6), which is also consistent with literature reported results on citrate-coated AuNPs.[57]

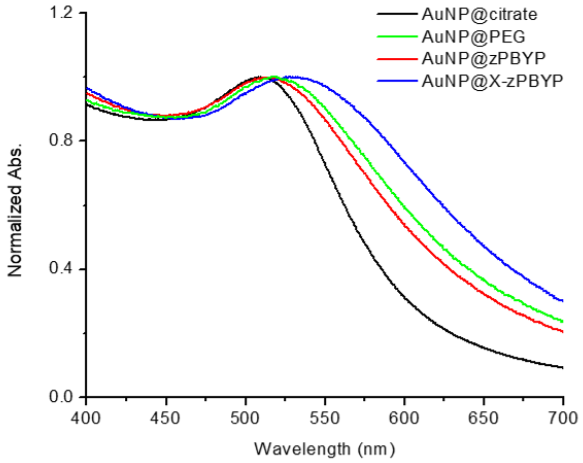

Figure II.5. Characterization of coated AuNPs in nanopure water by UV-Vis spectroscopy.

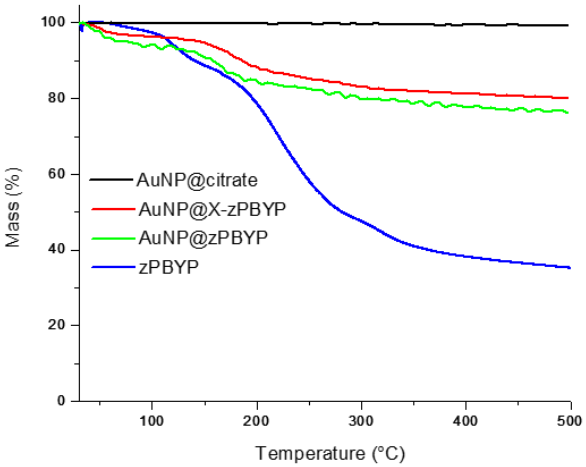

Figure II.6. TGA traces of AuNP@citrate (black trace), AuNP@X-zPBYP (red trace), AuNP@zPBYP (green trace), and zPBYP (blue trace), respectively.

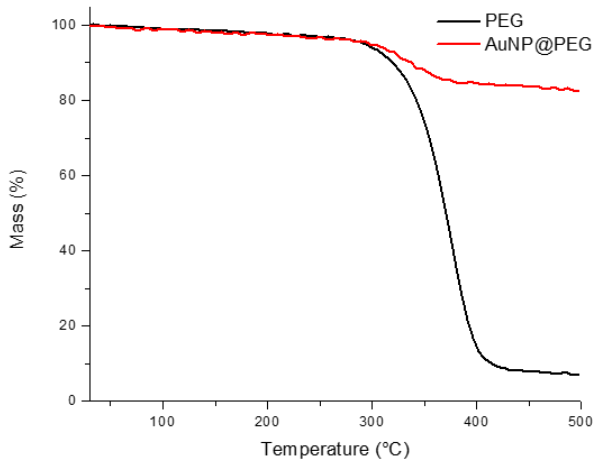

Figure II.7. TGA traces of TA-PEG-OMe (black trace), and AuNP@PEG (red trace), respectively.

Polymer-coated AuNPs, AuNP@zPBYP and AuNP@PEG, were prepared by addition of AuNP@citrate dropwise into polymer solutions while stirring. The reaction mixtures were stirred for 3 h at rt before purification by centrifugal filtration. While PEG (TA-PEG-OMe) was anchored to the AuNPs by bidentate ligation of TA moieties at the chain end to the AuNP surface, zPBYP is postulated to displace citrate ligands and coat AuNPs by multivalent interactions between the thioether, carboxylic acid/carboxylate, and amine/ammonium groups[58] of the side chains and Au atoms on the NP surface. The UV-Vis spectra of both AuNP@zPBYP and AuNP@PEG showed broadening and a small red shift of the SPR peak (to 514 nm and 518 nm, respectively), relative to AuNP@citrate (Figure II.5). In contrast to the negligible mass loss observed upon heating AuNP@citrate, the polymer coatings of AuNP@zPBYP and AuNP@PEG accounted for 26%, and 18% of the total mass, respectively, based on TGA (Figure II.6, 7). It is noteworthy that the AuNP@citrate composites destabilized upon freezing, and black solids were observed after lyophilization that could no longer be dissolved in aqueous solution. In contrast, both lyophilized AuNP@zPBYP and AuNP@PEG redispersed readily in aqueous

solution. These results indicated superior AuNP stabilization by the zPBYP and PEG coatings relative to citrate, attesting to the potential of these zwitterionic polymers as PEG-alternative coatings to enable storage and transport of therapeutically-relevant nanomaterials.

As our previous work demonstrated a remarkable improvement of polymer NP stability and biocompatibility upon crosslinking,[49] AuNPs with crosslinked polymer coatings, AuNP@X-zPBYP, were prepared by adding a solution of EDCI in nanopure water to a solution of AuNP@zPBYP to mediate amidation of the carboxylic and amine groups in the L-cysteine side chains of zPBYP. The solution was allowed to stir overnight before purification by centrifugal filtration with nanopure water. By controlling the stoichiometry of EDCI (12 eq. relative to each polymer chain), *ca*. half of the reactive functionalities of the polymer coatings were postulated to undergo carbodiimide-mediated amidation, to achieve a shell crosslinking extent that has been demonstrated with improved *in vivo* blood retention of nanostructures.[59] The UV-Vis spectrum of AuNP@X-zPBYP showed a broadened and further red-shifted absorption peak (528 nm) with respect to the uncrosslinked AuNP formulations (Figure II.5), attributed to a certain degree of inter-NP crosslinking to yield larger NPs. Yet, no discernible precipitation was observed from the solution of AuNP@X-zPBYP at 4 °C for over three weeks.

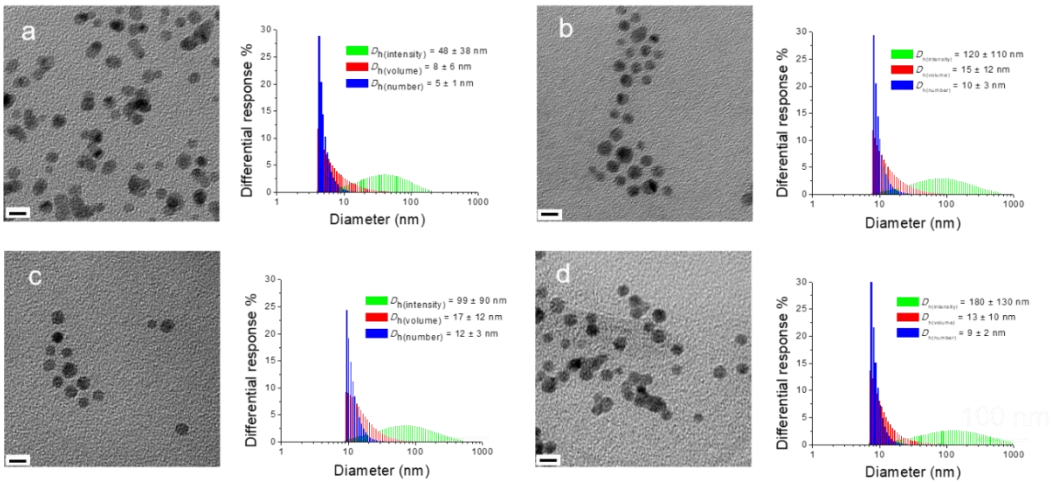

Figure II.8. TEM images and DLS size distributions of (a) AuNP@citrate, (b) AuNP@zPBYP, (c) AuNP@PEG, and (d) AuNP@X-zPBYP samples, scale bar = 5 nm. Number-, intensity- and volume-averaged hydrodynamic diameters were obtained by DLS in nanopure water.

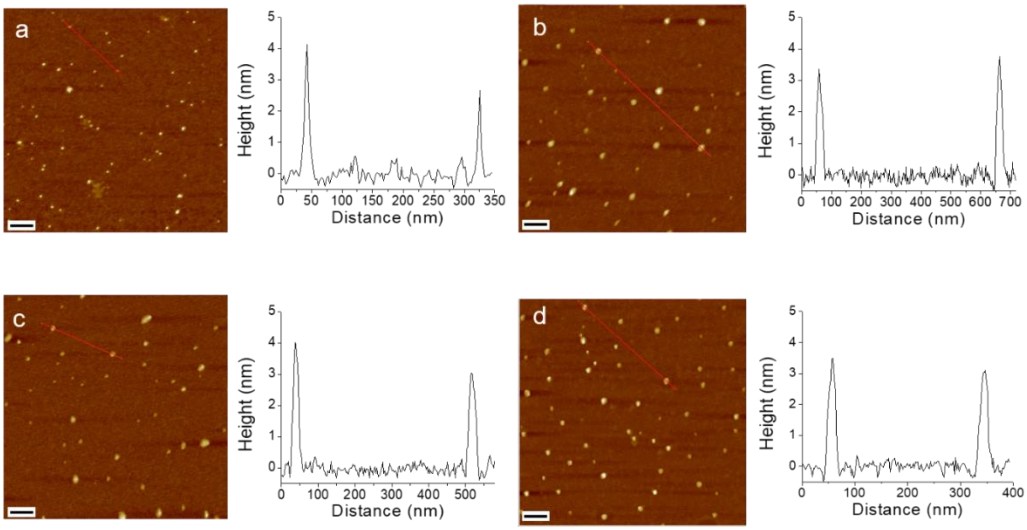

Figure II.9. AFM images and height profiles, plotting the height as a function of lateral distance along the red lines in the images, of (a) AuNP@citrate, H_{av} = 3.3 ± 0.7 nm, (b) AuNP@zPBYP, H_{av} = 3.6 ± 0.9 nm, (c) AuNP@PEG, H_{av} = 3.5 ± 0.6 nm, (d) AuNP@X-zPBYP H_{av} = 3.4 ± 0.8 nm. Samples were prepared by drop-casting AuNP solutions onto freshly-cleaved mica. Scale bar = 100 nm.

2.3.3 Evaluation of AuNP formulations by microscopy and light scattering

The sizes of the coated AuNPs were assessed by TEM, DLS, and AFM to obtain complementary information from nanoscale solid-state imaging and in-suspension analysis. As

depicted in Figure II.8, TEM images of AuNP@citrate, AuNP@zPBYP, AuNP@PEG, and AuNP@X-zPBYP suspensions showed circular shapes with narrow size distributions and average diameters (D_{av}) of 4.2 ± 0.6 nm, 3.9 ± 0.7 nm, 4.1 ± 0.6 nm, and 4.0 ± 0.6 nm, respectively, counting > 50 NPs. Aggregation of NPs on the TEM grid was observed in the AuNP@citrate sample (Figure II.8a, left), which likely occurred during sample preparation. In contrast, the increased spacing between the Au cores observed for the AuNP@PEG and AuNP@zPBYP samples is consistent with the larger polymer coatings (Figure II.8b, 8c, left), which effectively inhibited aggregation during sample drying on the TEM grid, further attesting to the superior stabilization abilities by these polymer coatings. TEM of the AuNP@X-zPBYP structures (Figure II.8d) revealed some aggregation, resulting from either inter-NP crosslinking or aggregation upon drying due to the consumption of hydrophilic zwitterionic moieties during the crosslinking reaction. DLS analyses (Figure II.8) revealed unimodal size distributions of all NP samples, indicative of the uniformity of these coating procedures. The number-average hydrodynamic diameter ($D_{h(number)}$) of the AuNP@citrate nanostructure was determined to be 5 ± 1 nm. After coating with zPBYP or TA-PEG-OMe, the $D_{h(number)}$ of the NPs increased to 10 ± 3 nm and 9 ± 2 nm, respectively. The similar hydrodynamic diameters of the NPs validate the comparability between zPBYP and PEG coatings. No significant increase was observed in the $D_{h(number)}$ of AuNP@X-zPBYP, indicating that the desired intra-NP shell crosslinking was dominant over inter-NP crosslinking.

AFM revealed globular structures from the AuNP@citrate, AuNP@zPBYP, AuNP@PEG, and AuNP@X-zPBYP samples (Figure II.9), with similar average heights of 3.3 ± 0.7 nm, 3.6 ± 0.9 nm, 3.5 ± 0.6 nm, and 3.4 ± 0.8 nm, respectively, counting > 50 NPs. Overall, the AFM-measured diameters were greater than the TEM-measured diameters and the AFM-

measured heights due to tip effects. However, the larger diameters (*ca.* 50 nm) of the structures observed in the images of the AuNP@zPBYP, AuNP@PEG, and AuNP@X-zPBYP samples relative to those (*ca.* 25 nm) of the AuNP@citrate sample, are attributed to the spreading of the polymer coatings on the polar mica substrate. Taken together, TEM, DLS, and AFM measurements indicate the successful, uniform coating of AuNPs with citrate and polymers, and these nanocomposites were further investigated to evaluate their immunotoxicity and cytokine adsorption as a function of coating composition *in vitro*.

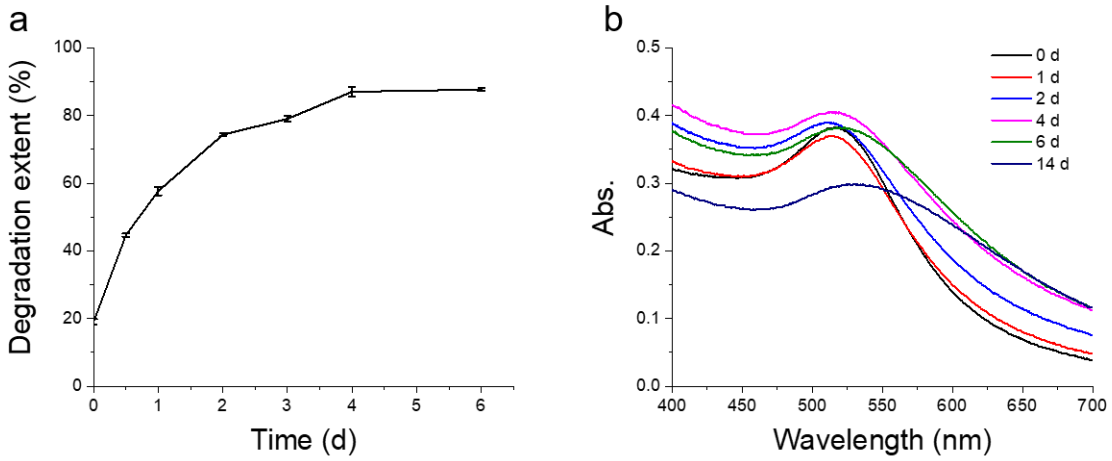

Figure II.10. Degradation kinetics of (a) zPBYP in D_2O at 37 ºC, evaluated by ^{31}P NMR spectroscopy, and (b) AuNP@zPBYP, evaluated by UV-Vis spectroscopy.

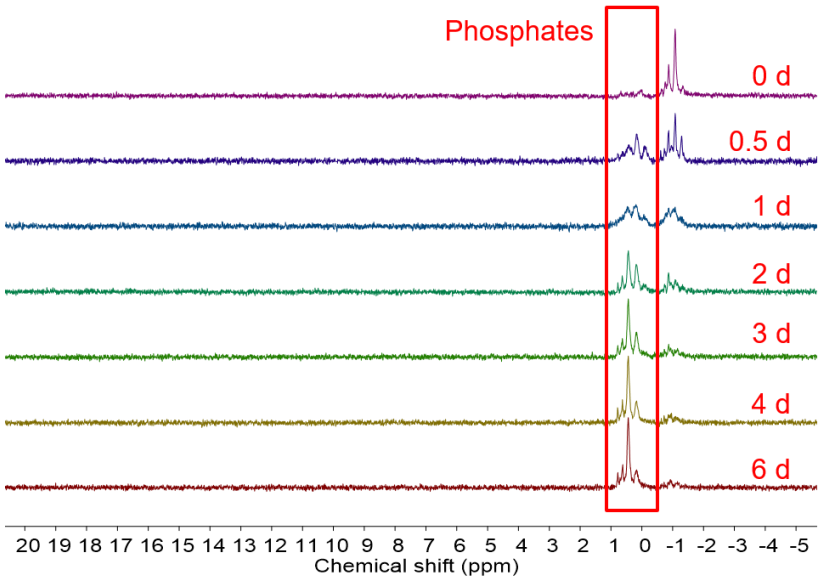

Figure II.11. Degradation of zPBYP in D_2O at 37 ºC, monitored by ^{31}P NMR spectroscopy.

2.3.4 Degradation studies of zPBYP and AuNP@zPBYP

Degradation kinetics of zPBYP were monitored by ^{31}P NMR spectroscopy in D_2O at 37 ºC, acquiring spectra at predetermined times (Figure II.10a, 11). These data showed that after 2 d, hydrolysis of side chain and backbone units proceeded to an extent of *ca.* 75% in nanopure water (pH 5-6). The formation of small-molecule products derived from the side-chain moieties and monomeric repeat units of zPBYP was confirmed by ESI-MS (Figure II.12). After the degradation extent reached *ca.* 90% by 6 d, as determined by ^{31}P NMR spectroscopy, the sample was dialyzed against nanopure water to remove small molecule products and lyophilized. Analysis of the material retained in the dialysis membranes indicated that 71 wt% of the polymer still existed as macromolecules after immersion in D_2O for 6 d.

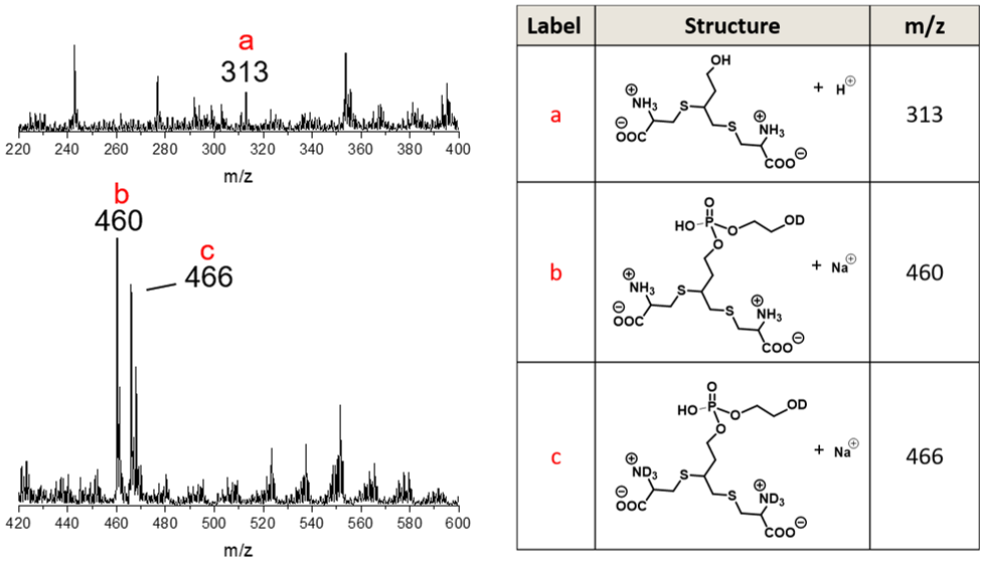

Figure II.12. Identification of the side-chain moiety, and monomeric repeat unit in the degradation products of zPBYP by ESI-MS analysis, after 2 d incubation in D_2O at 37 ºC and dilution with CH_3OH.

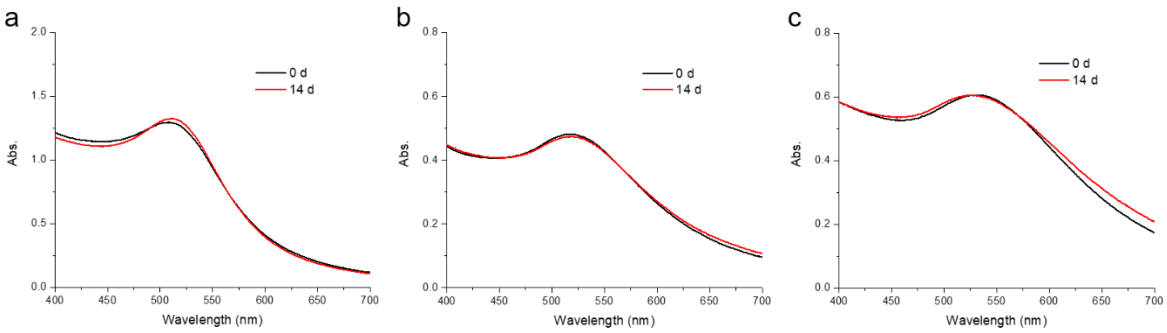

Figure II.13. UV/Vis spectra of (a) AuNP@citrate, (b) AuNP@PEG, and (c) AuNP@X-zPBYP, at 0 d and 14 d incubation in H_2O at 37 ºC, respectively.

Degradation of AuNPs with different coatings was also evaluated at 37 ºC, monitoring changes in the SPR peak by UV-Vis spectroscopy. From 0 h to 14 d, the SPR peak of the AuNP@citrate, AuNP@PEG, and AuNP@X-zPBYP did not change appreciably (Figure II.13), indicating the relative stability of these NPs. In comparison, the SPR peak of AuNP@zPBYP broadened slightly after 2 d, presumably due to degradation of the uncrosslinked zPBYP coating.

Continued monitoring of the uncrosslinked AuNP@zPBYP from 4 to 14 d showed the SPR peak to broaden further and red-shift significantly, indicating aggregation of the NPs (Figure II.10b). Small amounts of precipitate were observed after 14 d. These results demonstrate both the degradability of the zPBYP coatings and the effectiveness of shell-crosslinking to increase stability. The degradable coatings are expected to be particularly appealing in biomedical contexts by alleviating safety concerns associated with long-term accumulation of non-degradable macromolecular materials.

2.3.5 Evaluation of immunotoxicity and anti-biofouling properties

The immunotoxicity of the AuNP formulations was evaluated by incubating RAW 264.7 mouse macrophages with various formulations for 24 h, followed by measuring the expression levels of twenty-three cytokines using a previously established multiplexing assay.[44] The *in vitro* immunotoxicity was evaluated in terms of cytokine overexpression by cells exposed to NP formulations relative to that in those not exposed to NPs, indicative of the level of inflammatory immune response. No significant overexpression of any of the twenty-three tested cytokines was observed in the presence of all four AuNP formulations relative to the control (data not shown). These results demonstrated the low immunotoxicity of the coated AuNPs, suggesting the biocompatibility of these zPBYP coatings and supporting their viability as alternative coating materials to PEG.

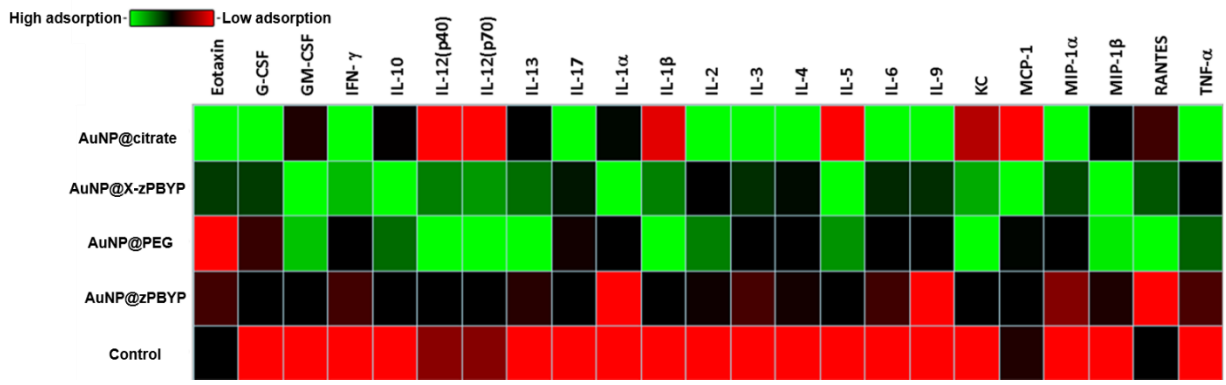

Figure II.14. Cytokine adsorption on the coated AuNP formulations, calculated based on apparent concentrations of cytokines measured after incubation with NPs and subsequent rinsing to remove unadsorbed material, as compared to the concentrations in a solution containing no NPs. The figure is the heatmap showing the concentrations of the various cytokines.

Adsorption of cytokines onto AuNPs was calculated based on the apparent concentration of cytokines measured after incubation with NPs and subsequent rinsing steps to remove unadsorbed cytokines, as compared to their concentrations in samples subject to the same procedures without NPs. The two-dimensional heatmap (values normalized to the control levels) in Figure II.14 shows the results of cytokine adsorption assay, where red squares indicate lower cytokine adsorption in heatmap (*i.e.* from red to green, adsorption becomes higher). Notably, the AuNP@zPBYP formulations exhibited the lowest cytokine adsorption out of all the NP formulations, while reduced adsorption was also measured for AuNP@PEG compared to AuNP@citrate, which displayed significant cytokine adsorption. While the crosslinked formulations demonstrated low immunotoxicity and higher stability, they exhibited higher cytokine adsorption compared to the uncrosslinked counterparts, probably due to the presence of larger NPs, as well as the consumption of charged moieties upon crosslinking, rendering the particles more hydrophobic and attractive to biomolecules. Future optimization of AuNP@X-

zPBYP constructs will involve lowering the crosslinking degree to achieve a balance between NP stability and reduced cytokine adsorption.

2.4 Conclusions

The zwitterionic PPE, zPBYP, was designed and synthesized to afford a promising alternative to PEG as an AuNP coating material, offering hydrolytic degradability, favorable immunotoxicity and antifouling properties. Organocatalyzed ROP of the cyclic phosphotriester monomer, BYP, with 3-azidopropanol as the initiator, yielded the alkyne-functionalized PPE with a monomodal molar mass distribution. Functionalization of the alkynes in the side chains of the polymer with L-cysteine *via* thiol-yne click reactions yielded zPPEs. Despite minor degradation of the polymer during purification by dialysis, the installation of large amounts of zwitterions in the side chains yielded highly hydrophilic polymers, which were coated successfully onto AuNPs through multivalent interactions between the thioether, carboxylic acid/carboxylate, and amine/ammonium groups of the polymer side chains and the Au surface of the NPs. AuNP@citrate was synthesized by addition of $NaBH_4$ to a solution of $HAuCl_4$ and sodium citrate, then AuNP@zPBYP and AuNP@PEG were prepared by coating the polymers onto AuNP@citrate, followed by crosslinking of AuNP@zPBYP cysteines to form AuNP@X-zPBYP. Morphological analysis of the coated AuNPs revealed similarly sized cores of *ca.* 4 nm, and increased hydrodynamic diameters of the polymer-coated AuNPs relative to the citrate-coated AuNPs. Degradation studies indicated hydrolysis of side chain and backbone units proceeded to an extent of *ca.* 75% over 2 d in nanopure water (pH 5-6), together with broadening and red-shifting of the SPR peak of AuNP@zPBYP over time. The coated NPs exhibited negligible immunotoxicity, as demonstrated by incubating RAW 264.7 mouse macrophages with

the four AuNP formulations, followed by measuring the levels of twenty-three cytokines relative to those in cells incubated without NPs. Cytokine adsorption studies showed AuNP@zPBYP had the best antifouling performance. While the crosslinked AuNP@X-zPBYP nanostructures showed higher cytokine adsorption compared to their uncrosslinked counterparts, the low immunotoxicity of these materials suggests the biocompatibility of the crosslinking strategy. Future optimization of crosslinking degree will be conducted to balance NP stability and antifouling properties.

CHAPTER III

CHEMICAL DESIGN OF BOTH A GLUTATHIONE-SENSITIVE DIMERIC DRUG GUEST AND GLUCOSE-DERIVED NANOCARRIER HOST TO ACHIEVE ENHANCED OSTEOSARCOMA LUNG METASTATIC ANTICANCER SELECTIVITY*

3.1 Introduction

Nanomedicine holds great potential to offer effective treatment against devastating diseases, by providing sustained release of significant quantities of therapeutic agents, especially when the route of administration allows for direct access to the diseased tissues.[3, 7, 60-62] Yet, rational design of the chemical structures of the drug and drug carrier are still needed to overcome several challenges influencing the success of *in vivo* studies, such as potential adverse effects of long-term accumulations of the nanocarriers, off-target toxicity of the therapeutics to normal tissues, and the limited ability of nanomedicines to penetrate tumor tissues at a potentially lethal concentration.[2, 63-65]

OS is the most common primary cancer of bone in children and adolescents aged 10-20 years and the third most common cancer overall in adolescents, with no proven etiology and a high fatality rate (70% survival at 5 years for non-metastatic patients, and less than 30% for those presenting with metastasis).[27-28] The predominant site of metastasis is the lung, followed by other

* Reprinted (adapted) with permission from "Chemical design of both a glutathione-sensitive dimeric drug guest and glucose-derived nanocarrier host to achieve enhanced osteosarcoma lung metastatic anticancer selectivity" by Su, L.; Li, R.; Khan, S.; Clanton, R.; Zhang, F.; Lin, Y. -N.; Song, Y.; Wang, H.; Fan, J.; Hernandez, S.; Butters, A.; Akabani, G.; MacLoughlin, R.; Smolen, J.; Wooley, K. L., *J. Am. Chem. Soc.* 2018, *140,* 1438-1446. Copyright 2018 American Chemical Society.

bones. Once micrometastases grow into recurrent, overt disease, tumors are often resistant to conventional chemotherapy, and unresectible recurrent disease is fatal.[26, 66] Therefore, innovative strategies for prevention and treatment of the metastatic disease are of critical need. Recently, our group employed PTX-loaded polyphosphoester (PPE)-based polymeric micelles and shell cross-linked knedel-like nanoparticles (SCKs) as nanotherapeutics to treat OS lung metastases *via* aerosol-based delivery.[16] The strategy could provide distribution of nanocarriers throughout the lungs and achieve sufficient pulmonary drug concentrations while avoiding dilutional and systemic effects seen in intravenous (*i.v.*) administration, with prolonged drug release and extended lung retention of the SCKs, owing to their crosslinked structure. However, safety concerns regarding the PPE degradation products, limited tissue and cell penetration ability and off-target toxicity remained as key challenges. Therefore, in this report, an anticancer drug delivery system with optimized chemical structures was designed and developed, where the chemistry of each component is tailored to accomplish specific tasks. This system improves selectivity, enhances tumor penetration ability, and facilitates drug release in response to conditions associated with tumor microenvironment.

Nanoparticles derived from biodegradable polymers, such as polyesters,[67] polypeptides,[9] PPEs,[14, 16, 68] and polycarbonates,[12, 69] have gained increasing interest for nanomedicines, which reduce the potential for long-term accumulation and associated adverse effects. Recently, our group employed functional glucose-derived polycarbonates (PGCs) to construct nanostructures with tunable sizes, surface charges, and morphologies, and that are, notably, capable of degradation into natural products, *e.g.*, glucose, carbon dioxide, ethanol.[20, 47] We expected that leveraging the PGC-derived nanostructures as nanocarriers would circumvent potential drawbacks of our previous PPE system,[15] namely the production of ethylene glycol and

phosphoric acid upon hydrolytic degradation, while maintaining the advantages of degradability, biocompatibility, and versatile functionality, such as for dye-labeling.[16] Furthermore, the steric bulk and increased hydrophobicity of the PGC backbone, relative to those of PPEs, were anticipated to enable extended drug release.

In order to access tumors for intracellular delivery within lung tissue *via* inhalation, the nanocarriers need to be capable of penetrating the diffusion and absorption barriers of the airway mucus,[70] lung epithelium,[71] and tumor stroma.[72] The diffusion/penetration capacity of drug carriers across these barriers is known to depend on the chemical composition, shape, and, in particular, the size and surface properties of the nanocarriers,[1, 65] and in this work these attributes were tuned to achieve optimal effects. Chan and coworkers reported the tumor permeation of PEGylated gold nanoparticles (GNPs)[73] and tiopronin-modified GNPs[74] to depend strongly on the size of the nanoparticles, where larger nanoparticles localized near the vasculature, while smaller nanoparticles diffused rapidly throughout the tumor matrix. Similarly, diffusion across respiratory mucus has been shown to be greatly restricted for particles larger than 100 nm.[75] Given the vital influence of particle size on their penetration ability, we targeted nanocarriers with desirable diameters of less than 30 nm.[3] Meanwhile, cationic charges were also shown to improve tumor penetration, due to nanoparticle-induced necrosis and resultant tumor cell density reduction,[13, 76-78] which could be conveniently imparted into the PGC constructs *via* a facile thiol-yne click reaction. To mitigate undesirable characteristics of cationic polymers, including mucus binding and non-specific cell toxicity,[67] PEG was conjugated as a hydrophilic shell.[79]

As the concentration of GSH in cancer cells can be several times higher than that in normal cells,[80-81] redox-responsive linkages have been extensively exploited in designing drug delivery vehicles and pro-drugs capable of controlled, sustained drug release with reduction of

off-target release and associated toxicity. For instance, disulfide-linked dimeric pro-drugs of camptothecin,[82] doxorubicin[82] and PTX[83-84] were recently encapsulated within amphiphilic polymers (*i.e*., methoxy poly(ethylene glycol)-*block*-polylactide) or PEGylated phospholipids to formulate pro-drug-loaded micelles. Advantageous properties were observed with these constructs, including reducing agent DTT-triggered *in vitro* drug release, enhanced anticancer efficacy, and reduced adverse effects. Therefore, disulfide-linked dimeric diPTX pro-drugs were anticipated to allow for enhanced containment by the PGC-based nanocarrier, relative to PTX, owing to the larger size and redox-triggered sustained release. The cationic charges installed between the hydrophilic shell and hydrophobic core of the PGC nanocarriers, were further anticipated to provide better access of the negatively-charged GSH to the core domain and diPTX.

Co-assembly of the redox-responsive diPTX pro-drug with the cation- and PEG-modified PGCs yielded nanocarriers that facilitated precise control of intracellular drug delivery, which holds great potential to finely tune drug release kinetics for beneficial anticancer activity with minimal undesired release in normal tissue. The anticancer efficacy as inhaled chemotherapeutics was evaluated both *in vitro* and *in vivo*, and the host-guest constructs exhibited improved tumor penetration and significant inhibition of tumor cell growth towards OS lung metastases with minimal side effects. These results demonstrate the promise of diPTX@CPGC as anticancer therapeutic agents for treatment of OS lung metastases.

3.2 Materials and methods

3.2.1 Materials

Bicyclic glucose carbonates, GC(EPC) and GC(EC),[20] and pro-drug diPTX[85] were synthesized according to previously reported procedures. Dichloromethane (DCM) and *N*,*N*-dimethylformamide (DMF) were purified by passing through a solvent purification system (J. C. Meyer Solvent Systems, Inc., Laguna Beach, CA). 1,5,7-Triazabicyclo[4.4.0]dec-5-ene (TBD) was dried over CaH_2 in tetrahydrofuran (THF), concentrated under vacuum and stored in a glovebox under Ar atmosphere. Other chemicals and reagents were used as received from Sigma-Aldrich, Co. (St. Louis, MO) unless otherwise noted. Dialysis membrane tubing with a molecular weight cut-off (MWCO) of 6-8 kDa was purchased from Spectrum Laboratories, Inc. (Rancho Dominguez, CA) and soaked for 5 min in nanopure water at room temperature before use. MC3T3 mouse osteoblast precursor cells, Dulbecco's Modified Eagle's Medium (DMEM) and Minimum Essential Medium alpha (MEMα) medium were obtained from the American Type Culture Collection (Manassas, VA), with media additives (fetal bovine serum, penicillin/streptomycin) were purchased from Sigma-Aldrich (St. Louis, MO). Osteosarcoma cells (SJSA-1) were provided by Dr. Hughes at MD Anderson Medical Center. Cell culture 96-well round bottom plates were purchased from Corning Costar Co. (Corning, NY).

In order to establish an orthotopic xenograft mouse model of osteosarcoma, NOD/SCID IL2-R-gamma -/- mice (The Jackson Laboratory) aged 4-6 weeks (males and females) were injected in their left tibias while under isoflurane anesthesia (1-2% v/v in pure O_2) with a 10 µL PBS suspension of 50,000 SJSA-1 cells (ATCC) constitutively labeled *via* lentiviral transfection with firefly luciferase and GFP, for tracking the tumor progression *in vivo* and location for

histology *ex vivo*. For this procedure, a 27 Ga syringe needle was drilled into the proximal epiphysis of the tibia and guided down the tibia about mid-way to the diaphysis, where the suspension was injected. Five days following engraftment, the mice were given intraperitoneal injections of 0.15 mL of 30 mg/mL D-luciferin potassium salt (Bioworld) and imaged for optical signal 15 minutes later using a small-animal imaging cabinet (Xtreme *In Vivo*, Bruker). X-ray images of the mice were also taken to provide anatomical reference. Baseline metastatic burdens in the lungs were then determined by measuring the signal intensity in the chest region of each mouse. The mice were then assigned to one of three groups, determined randomly but matching for similar average baseline lung signals among groups.

3.2.2 Instrumentation

^{1}H NMR, ^{31}P ^{1}H NMR and ^{13}C NMR spectra were recorded on a Varian Inova 500 spectrometer interfaced to a UNIX computer using VnmrJ software. Chemical shifts were referenced to the solvent resonance signals.

FT-IR spectra were recorded on an IR Prestige 21 system (Shimadzu Corp., Japan), equipped with an ATR accessory, and analyzed using IRsolution v. 1.40 software.

Size exclusion chromatography (SEC) eluting with THF was conducted on a Waters Chromatography, Inc. (Milford, MA) system equipped with an isocratic pump (model 1515), a differential refractometer (model 2414), and column set comprised of a PLgel™ 5 μm guard column (50 × 7.5 mm), a PLgel™ 5 μm Mixed C column (300 × 7.5 mm, Agilent Technologies) and two Styragel® columns (500 Å and 104 Å, 300 × 7.5 mm, Waters Chromatography, Inc.). The system was operated at 40 °C with a flow rate of 1 mL/min. Data were analyzed using Breeze software (Waters Chromatography, Inc., Milford, MA). Molecular weights were

determined relative to polystyrene standards (300-467,000 Da) purchased from Polymer Laboratories, Inc. (Amherst, MA). Polymer solutions were prepared at a concentration of *ca.* 3 mg/mL with 0.05 vol% toluene added as a flow marker, and an injection volume of 200 μL was used.

Thermogravimetric analysis (TGA) was performed under Ar atmosphere using a Mettler-Toledo model TGA/DSC 1 with a heating rate of 10 °C/min. Glass transition temperatures (T_g) were measured by differential scanning calorimetry (DSC) on a Mettler-Toledo DSC822® (Mettler-Toledo, Inc., Columbus, OH) under $N_{2(g)}$. DSC measurements were performed with a heating rate of 10 °C/min and analyzed using Mettler-Toledo Star^e v. 10.00 software. The T_g was taken as the midpoint of the inflection tangent of the second heating scan.

Inductively coupled plasma-mass spectrometry (ICP-MS) was performed on a PerkinElmer SCIEX ICP mass spectrometer ELAN DRC II, equipped with high-speed quadrupole, dynamic reaction cell (DRC) and axial field technology (AFT) to eliminate polyatomic interferences, using 1% HNO_3 as the matrix and rhodium as the internal standard.

Transmission electron microscopy (TEM) images were collected on a JEOL 1200EX operated at 100 kV, and micrographs were recorded using a SIA-15C CCD camera. Samples for TEM were prepared as follows: 10 μL of dilute polymer solution in nanopure water was deposited onto a carbon coated copper grid, and after 1 min, excess solution was quickly wicked away by a piece of filter paper. The samples were then negatively stained with a 1 wt% phosphotungstic acid (PTA) aqueous solution (10 μL). After 30 s, excess staining solution was quickly wicked away by a piece of filter paper and the samples were left to dry under ambient conditions over night.

Atomic force microscopy (AFM) was performed using a Multimode 8 system (Bruker) using a ScanAsyst-Air Silicon Nitride probe (k = 0.4 N/m, f_0 = 70 kHz, Bruker). AFM images were assessed with Nanoscope Analysis (Bruker). For AFM sample preparation, the solution of nanoparticles in nanopure water (50 µL) at 0.1 mg/mL was deposited on the mica surface. After 1 min, the excess of the solution was quickly wicked away by a piece of filter paper, and the mica surface was allowed to dry in the air flow.

Dynamic light scattering (DLS) measurements were conducted using a Delsa Nano C instrument from Beckman Coulter, Inc. (Fullerton, CA) equipped with a laser diode operating at 658 nm. Scattered light was detected at 165° and analyzed using a log correlator over 70 accumulations for a 0.5 mL of sample in a glass size cell (0.9 mL capacity). The photomultiplier aperture and attenuator were adjusted automatically to obtain a photon counting rate of *ca.* 10 kcps. The particle size distribution and distribution averages were calculated using CONTIN particle size distribution analysis routines in Delsa Nano 2.31 software. The peak averages of intensity, volume and number distributions from 70 accumulations were reported as the average diameter of the particles. All measurements were repeated 10 times.

The zeta potentials of the nanoparticles were determined by a Delsa Nano C particle analyzer (Beckman Coulter, Fullerton, CA) equipped with a 30 mW dual laser diode (658 nm). The zeta potential of the particles in suspension was obtained by measuring the electrophoretic movement of the charged particles under an applied electric field. Scattered light was detected at a 30 ° angle at 25 °C. The zeta potential was measured at five regions in the flow cell and a weighted mean was calculated. These five measurements were used to correct for electroosmotic flow induced in the cell due to the surface charge of the cell wall. All measurements were repeated 3 times, and the zeta potential was reported as the average and standard deviation.

The concentrations of PTX, PTX-SH and diPTX were determined by high performance liquid chromatography (HPLC) on a Shimadzu Prominence system equipped with an SPD-20AV prominence UV-Vis detector set to 227 nm and a Waters X Bridge C8 column (4.6 × 150 mm, 5 µM, 100 Å) eluting in 60% acetonitrile and 40% 20 mM ammonium acetate buffer in isocratic mode. The flow rate was set to 1 mL/min with a run time of 20 min, and the column temperature was set to 40 °C. The HPLC method employed an external calibration of PTX, PTX-SH and diPTX.

To measure the tumor-killing efficacy of the treatments, the tumor spheroids were imaged at 200× magnification on a laser scanning confocal microscope (FV-1000, Olympus) with laser lines of 488 nm (calcein-AM "live" stain), 543 nm (ethidium homodimer-1 "dead" stain), and 635 nm (IRDye® 800CW conjugated to micelles) in depth scanning mode (step size = 10 µm) at a resolution of 256 × 256 pixels. Image analysis was performed in ImageJ (NIH, v. 1.50i) using the Bio-Formats package (v. 5.5.0). Maximum intensity z-stack projections of the fluorescent images were overlaid on their corresponding transmitted light images, which were also acquired on the confocal microscope using a transmitted light detection unit (Olympus) and the 635 nm laser. The cross-sectional area of each spheroid was determined by drawing a region of interest and using the measure function in ImageJ.

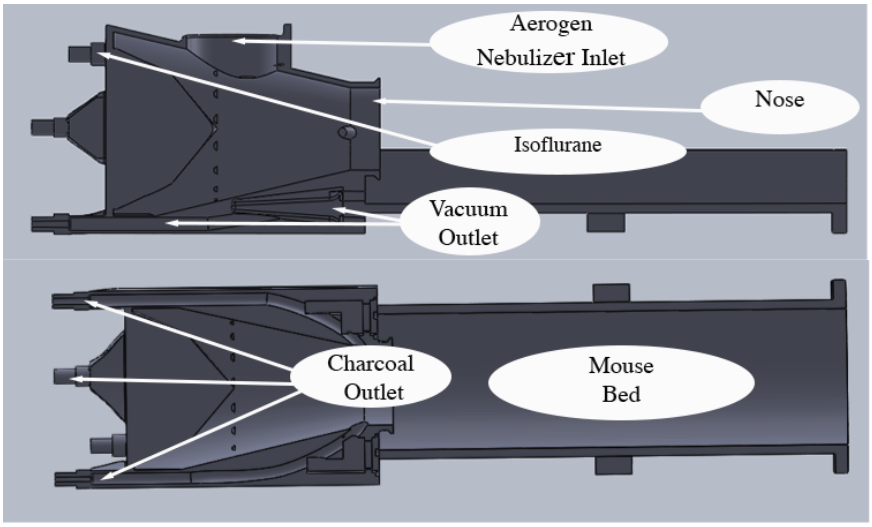

Figure III.1. Cross-sectional views of the custom nose-only mouse nebulizer system.

The mouse nose-only nebulization system was designed by Dr. Akabani's group in collaboration with Aerogen, Ltd using a prototype mesh nebulizer specifically designed for rodents (Figure III.1). The mesh nebulizer was characterized with a next-generation impactor and was shown to have a mass median aerodynamic diameter (MMAD) of 2.171 with a geometric standard deviation (GSD) of 2.037. Modeling was performed in Solidworks CAD software and exported as a stereolithography file (STL) (Figure III.1). The exported STL file was then sent to the engineering innovation center at Texas A&M University. The 3D printer chosen was the Stratasys EDEN 260V, which has a build volume of 255 × 252 × 200 mm (10.0 × 9.9 × 7.9 in.) with a 16-micron layer accuracy and 7-micron dimensional accuracy. The materials chosen were a soluble support material, which could be removed with ultrasonic bath and/or water-jet, along with Objet VeroWhite (Stratasys, Ltd.), which is a rigid opaque material with 1.1-1.5% water absorption. The nebulization system was made entirely from 3D printed VeroWhite Polyjet material.

A cylindrical mouse bed was designed to hold the nebulizer, which fit at the top where the flow was biased towards the mouse nose and mouth. This was accomplished by making the nebulizer holder cone-shaped and pushing isoflurane/O_2 gas mixture into the system *via* independent ports in the back and removing flow from the system *via* slits near the mouth of the mouse to be used for removal of excess aerosol buildup and preventing condensation. There were holes that would be capped in the front, on opposite sides of the nose to allow removal of soluble support material used in the 3D printing process. Vacuum was also used to prevent contamination of the area surrounding the mouse body, preventing fur contamination. There was a thin latex sheet with a slit near the front of the nebulizer system so that the mouse nose and throat tightly fit into the system.

All experiments were performed according to institutional guidelines provided by Texas A&M's Environmental Health and Safety committee. Experiments involving SJSA-1 and MC3T3 cell lines were performed according to guidelines provided by Texas A&M's Institutional Biosafety Committee for biosafety level 2 organisms (Protocol Approval Number IBC2014-075). Animal studies were approved by the Texas A&M University, Institutional Animal Care and Use Committee (IACUC Protocol # 2016-0100).

3.2.3 Experimental procedures

Synthesis of 2- Synthesis of PEG_{113}-*b*-[$PGC(EC)_{12}$-*co*-$PGC(EPC)_4$] (polymer 1). The polymerization was carried out using standard glovebox and Schlenk line techniques. Methoxy poly(ethylene glycol) ($mPEG_{113}$), GC(EPC), and GC(EC) were dried under vacuum over P_2O_5 for 3 days before transferring to a glovebox for storage under an inert atmosphere. Stock solutions were prepared in a glovebox under Ar atmosphere, while the ROP was conducted in a

-15 °C sodium chloride bath in a fume hood. To a solution of GC(EPC) (60.1 mg, 0.161 mmol), GC(EC) (175.4 mg, 0.4816 mmol), and $mPEG_{113}$ (200.7 mg, 0.04014 mmol) in 1.3 mL of DCM at -15 °C, was added organocatalyst TBD (2.8 mg, 0.020 mmol) in DCM (100 μL) under Ar atmosphere. After stirring for 10 min, the reaction vial was opened to air and quenched by addition of Amberlyst 15 H-form resin. The polymer was purified by precipitation from DCM into diethyl ether (3 ×) and dried under vacuum to afford the product as a white powder (404.6 mg, yield 93%). ^{1}H NMR (500 MHz, $CDCl_3$) δ ppm 5.40 - 5.17 (dd, *J* = 10, 10 Hz, C^3H), 5.01 (d, *J* = 6.5 Hz, C^1H), 4.90 - 4.77 (m, C^4H), 4.76 - 4.65 (m, C^2H, OCH_2CCH), 4.44 - 4.08 (m, C^6H_2, OCH_2CH_3 in sugar unit), 4.03 (s, C^5H), 3.63 (s, OCH_2CH_2 in PEG unit), 3.45 - 3.38 (m, OCH_3 in sugar unit), 3.37 (s, OCH_3 in PEG unit), 2.61 (s, OCH_2CCH), 1.28 (td, *J* = 7.0, 3.0 Hz, OCH_2CH_3 in sugar unit). ^{13}C NMR (126 MHz, DMSO-d_6) δ ppm 154.28, 153.95, 153.71, 96.17, 78.91, 77.70, 73.74, 73.41, 72.49, 71.74, 70.25, 70.04, 66.83, 66.36, 64.93, 64.88, 64.75, 58.49, 56.21, 55.42, 20.89, 14.30. FT-IR (ATR) 3290, 3026 - 2779, 1750, 1466, 1371, 1343, 1241, 1145, 1104, 1019, 962, 872, 841 cm^{-1}. T_g = -24, 98 °C. TGA in Ar, 180 - 311 °C, 42% weight loss; 311 - 441 °C, 47% weight loss. $M_{n\,(NMR)}$ = 10.9 kDa. $M_{n\,(SEC)}$ = 12.1 kDa. $Đ$ = 1.12.

Post-polymerization modification of PEG_{113}-*b*-[$PGC(EC)_{12}$-*co*-$PGC(EPC)_4$] with cysteamine hydrochloride *via* thiol-yne reaction to afford polymer 2. PEG_{113}-*b*-[$PGC(EC)_{12}$-*co*-$PGC(EPC)_4$] (200.5 mg, 18.41 μmol), cysteamine hydrochloride (167.2 mg, 1.473 mmol), and 2,2-dimethoxy-2-phenylacetophenone (DMPA, 47.2 mg, 0.184 mmol) were dissolved in anhydrous DMF (8 mL), deoxygenated under $N_{2(g)}$ for 30 min, and irradiated under UV light (365 nm) for 2 h. The resulting copolymer solution was transferred to dialysis tubing (MWCO *ca*. 6-8 kDa) and dialyzed against nanopure water at 4 ºC for 3 d to remove excess thiol and photoinitiator. The solution was then lyophilized to give the cationic polymer PEG_{113}-*b*-

[PGC(EC)$_{12}$-*co*-PGC(Cys)$_4$] as a white powder (205.2 mg, 95% yield). ^{1}H NMR (500 MHz, DMSO-d_6) δ ppm 7.88 (br, SCH$_2$CH$_2$N*H*$_3$Cl), 5.18 - 4.97 (m, C^1*H*, C^3*H*), 4.95 - 4.70 (m, C^2*H*, C^4*H*), 4.42 - 4.05 (m, C^5*H*, OC*H*$_2$CHS, and OC*H*$_2$CH$_3$ in sugar unit), 4.03 - 3.88 (m, C^6*H*), 3.50 (s, OC*H*$_2$C*H*$_2$ in PEG unit), 3.41 - 3.25 (m, OC*H*$_3$, and OCH$_2$C*H*S in sugar unit), 3.23 (s, OC*H*$_3$ in PEG unit), 3.14 - 2.56 (m, SC*H*$_2$C*H*$_2$NH$_3$Cl, OCH$_2$CHC*H*$_2$S), 1.19 (td, *J* = 7.0, 3.0 Hz, OCH$_2$C*H*$_3$ in sugar unit). ^{13}C NMR (126 MHz, DMSO-d_6) δ ppm 154.30, 153.97, 153.74, 96.19, 73.74, 73.39, 72.56, 71.75, 70.26, 70.06, 66.76, 64.96, 64.77, 64.25, 60.16, 58.52, 55.37, 43.95, 33.55, 29.35, 28.27, 15.07, 14.34. FT-IR (ATR) 3549 - 3328, 3027 - 2795, 1749, 1466, 1371, 1342, 1242, 1144, 1102, 1024, 962, 872, 841, 782 cm^{-1}. $M_{n\,(NMR)}$ = 11.8 kDa. T_g = -25, 92 °C. TGA in Ar, 180 - 311 °C, 43% weight loss; 311 - 441 °C, 51% weight loss.

Azide-alkyne Huisgen cycloaddition of PEG$_{113}$-*b*-[PGC(EC)$_{12}$-*co*-PGC(EPC)$_4$] with IRDye® 800CW azide to afford polymer 3. A flame-dried Schlenk flask containing a magnetic stir bar was charged with PEG$_{113}$-*b*-[PGC(EC)$_{12}$-*co*-PGC(EPC)$_4$] (17.1 mg, 1.58 μmol), IRDye® 800CW azide (2.0 mg, 1.6 μmol), *N*,*N*,*N*′,*N*′,*N*″-pentamethyldiethylenetriamine (PMDETA, 0.2 mg, 2 μmol) and 5 mL of DMAc. The reaction mixture was degassed by several freeze-pump-thaw cycles (>3), during which copper(I) bromide (0.2 mg, 2 μmol) was added. The flask was allowed to return to room temperature after the final cycle and stirred for an additional 4 h under N_2. The solution was subsequently filtered through a neutral alumina column and dialyzed in nanopure water containing Chelex® 100 resin in presoaked dialysis tubing (MWCO *ca*. 6-8 kDa) for 4 d to remove copper ions, followed by lyophilization to yield PEG$_{113}$-*b*-[PGC(EC)$_{12}$-*co*-PGC(EPC)$_3$-*co*-PGC(Dye)$_1$] as a green powder (18.1 mg, 95% yield). ICP-MS confirmed that less than 10 ppm copper was present in the polymer. ^{1}H NMR (500 MHz, DMSO-d_6) δ ppm 8.12 (s), 7.87 - 7.58 (m), 7.37 - 7.26 (m), 7.11 (d, *J* = 7.5 Hz), 6.27 - 6.14 (m), 5.80 (s), 5.11 (dd,

J = 10, 10 Hz), 5.01 (d, *J* = 15.5 Hz), 4.83 (d, *J* = 15.5 Hz), 4.75 (s), 4.51 (s), 4.24 (s), 4.15 - 4.08 (m), 3.99 (s), 3.79 (s), 3.49 (s), 3.38 - 3.26 (m), 3.22 (s), 2.70 (s), 2.03 (d, *J* = 8.5 Hz), 1.92 (s), 1.76 (s), 1.63 (s), 1.51 (s), 1.30 (s), 1.18 (dt, *J* = 14.0, 7.0 Hz). ^{13}C NMR (126 MHz, DMSO-d_6) δ ppm 172.41, 154.48, 154.30, 153.95, 153.71, 150.30, 141.09, 137.87, 126.43, 125.95, 96.11, 76.12, 73.68, 73.36, 72.46, 71.72, 70.23, 69.59, 69.10, 68.52, 67.91, 67.55, 66.80, 66.36, 64.88, 64.75, 64.44, 64.23, 58.49, 55.36, 27.68, 27.64, 26.22, 21.08, 20.62, 14.39. FT-IR (ATR) 3632 - 3295, 3026 - 2773, 1754, 1466, 1398, 1371, 1342, 1241, 1168, 1099, 1060, 1019, 962, 873, 841, 784 cm^{-1}. $M_{n\,(NMR)}$ = 12.1 kDa.

Preparation of diPTX-loaded nanoparticles with PEG-*b*-[PGC(EC)$_{12}$-*co*-PGC(Cys)$_4$] and PEG-*b*-[PGC(EC)$_{12}$-*co*-PGC(EPC)$_4$]. In a typical experiment, diPTX (1.0 mg), a mixture of cationic polymer PEG-*b*-[PGC(EC)$_{12}$-*co*-PGC(Cys)$_4$] and non-ionic polymer PEG-*b*-[PGC(EC)$_{12}$-*co*-PGC(EPC)$_4$] (10.1 mg) at a specific mass ratio, were dissolved in DMSO (100 μL). This solution was then added dropwise into 9.9 mL nanopure water with vigorous stirring, to afford a series of diPTX-loaded nanoparticles. The diPTX loading was determined by HPLC, which employed an external calibration of diPTX concentration against the peak area, while the sizes, morphologies, and surface characteristics were characterized by DLS, AFM, TEM and electrophoretic light scattering (Figure III.11).

Determination of critical micelle concentrations (CMCs) for diPTX-loaded nanoparticles prepared with PEG-*b*-[PGC(EC)$_{12}$-*co*-PGC(Cys)$_4$] and PEG-*b*-[PGC(EC)$_{12}$-*co*-PGC(EPC)$_4$]. The CMCs of the nanoparticles were determined by using pyrene as the fluorescent probe following the protocol previously reported by our group. The sample solutions were prepared by mixing the micelle solution with the same volume of a pyrene aqueous stock solution (1.2×10^{-6} mol/L). Samples with polymer concentrations ranging from 0.005 - 0.05

mg/mL were prepared. All the sample solutions were stored at room temperature overnight to equilibrate the pyrene and the micelles. The fluorescence measurement was conducted at room temperature, in which the pyrene was excited at 334 nm and its emission spectrum was recorded at 370 nm and 381 nm, corresponding to the first and third vibrational peaks, respectively. All the measurements were repeated three times and the ratios of intensities of the first and third peaks were plotted against the total concentrations of the polymers in the sample solutions. The CMC was measured to be 0.035 mg/mL, as the intersection of the tangent to the curve at the inflection with tangent through the points at high polymer concentration.

Preparation of diPTX-loaded nanoparticles with PGC(EPC)-*b*-PGC(EC)-*g*-PEG$_{2k}$ (Figure III.2). In a typical experiment, diPTX (1.0 mg) and PGC(EPC)-*b*-PGC(EC)-*g*-PEG$_{2k}$ (10.1 mg) were dissolved in DMSO (100 μL). This solution was then added dropwise into 9.9 mL nanopure water with vigorous stirring to afford diPTX-loaded nanoparticles. The diPTX loading was determined by HPLC, while the size, morphology, and surface characteristic were characterized by DLS, TEM and electrophoretic light scattering (Figure III.2). Hydrodynamic diameters of the diPTX-loaded micelles in nanopure water were measured by DLS: $D_{h(intensity)}$ = 90 ± 53 nm, $D_{h(volume)}$ = 30 ± 16 nm, $D_{h(number)}$ = 19 ± 5 nm; zeta-potential: -6 ± 1 mV; diameter measured by TEM: 17 ± 4 nm.

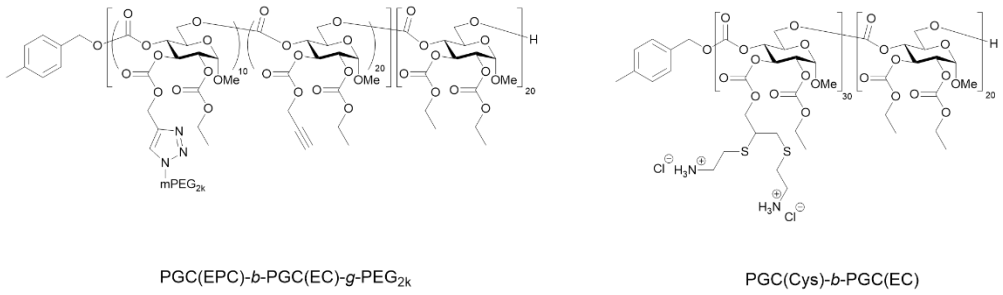

Figure III.2. The structures of the neutral polymer PGC(EPC)-*b*-PGC(EC)-*g*-PEG_{2k} and the cationic polymer PGC(Cys)-*b*-PGC(EC), employed in control studies.

***In vitro* drug release studies of the diPTX-loaded PGC micelles.** In a typical experiment, the diPTX-loaded micelle solution (3 mL) was transferred into a presoaked dialysis cassette (Slide-A-Lyzer, 10 kDa MWCO, Pierce Biotechnology, Rockford IL). The cassette was allowed to stir in 200 mL PBS (pH 7.4, 37 °C), containing either DTT (10 mM), GSH (10 mM), or no reducing agents. Aliquots (0.5 mL) of the surrounding PBS solution were taken at pre-determined times and analyzed by HPLC. PBS with the same volume and composition was added to the dialysis solution outside the cassette after removal of each sample. The release profiles of the diPTX-loaded micelles were obtained by monitoring the concentration increase of PTX, PTX-SH and diPTX over time in the surrounding PBS solution by HPLC. The release study was conducted in triplicate.

Preparation of formulations for cytotoxicity and SJSA-1 spheroid studies. In a typical experiment, diPTX pro-drug (1.0 mg), PEG-*b*-[$PGC(EC)_{12}$-*co*-$PGC(Cys)_4$] (8.1 mg), and PEG_{113}-*b*-[$PGC(EC)_{12}$-*co*-$PGC(EPC)_3$-*co*-$PGC(Dye)_1$] (2.1 mg) were dissolved in 100 µL DMSO with a PTX concentration of 10 mg/mL. Predetermined amounts of this solution were added dropwise into PBS or media to afford the stock solutions for cytotoxicity and spheroid studies.

2D cytotoxicity assays. Osteosarcoma cells SJSA-1 (5 x 10^3 cells/well) and mouse osteoblast precursor cells MC3T3-E1 (5 x 10^3 cells/well) were plated in 96-well plates in DMEM and MEMα media, respectively (10% fetal bovine serum, and 1% penicillin/streptomycin). Cells were incubated at 37 °C in a humidified atmosphere containing 5% CO_2 for 24 h. Culture medium was replaced with serial dilutions of the polymers (100 μL) in fresh medium (PTX final concentrations ranged from 8.7 nM - 18 μM). The PTX, diPTX, diPTX-loaded micelles and unloaded micelles ($f_{\text{polymer 1}}$ = 0.2) stock solutions were prepared in DMSO. The cells were incubated with the formulations for 72 h and then the medium was replaced with 100 μL of fresh medium prior to addition of 20 μL MTS combined reagent to each well (Cell Titer 96® Aqueous Non-Radioactive Cell Proliferation Assay, Promega Co., Madison, WI). The cells were incubated with the reagent for 2 h at 37 °C in a humidified atmosphere containing 5% CO_2 and were protected from light. Absorbance was measured at 490 nm on a SpectraMax M5 spectrometer (Molecular Devices Co., Sunnyvale, CA). The cell viability was calculated based on the relative absorbance to the control untreated cells. The 0% and 100% cell viabilities were considered as the control medium (no cells) and cells with no treatment, respectively. The IC_{50} values were calculated using the GraphPad Prism four-parameter fit (GraphPad Software, Inc., La Jolla, CA).

SJSA-1 Spheroid studies. Osteosarcoma cells (SJSA-1) were seeded in round-bottom, ultra-low attachment spheroid microplates (Corning) at a density of 500 cells per well in 100 μL DMEM/F-12 DMEM media supplemented with 10% fetal bovine serum and 100 U/mL penicillin, 200 μg/mL streptomycin and 0.25 μg/mL Fungizone. Spheroids were formed after incubating at 37 °C, 5% CO_2 overnight. An additional 50 μL of PTX, diPTX, diPTX-loaded micelles, or unloaded micelles ranging in final concentrations from 1.9 to 30 μM PTX equivalents

prepared in the same feeding media, was then added to the wells. In order to dissolve diPTX and PTX in media, 0.25 vol% DMSO was added. Following incubation for 7 d, the spheroids were stained with LIVE/DEAD® stain (calcein-AM with ethidium homodimer-1) per assay instructions.

***In vivo* and *ex vivo* studies.** The efficacy of the diPTX-loaded cationic PGC micelles as an inhaled chemotherapeutic agent was evaluated in an orthotopic mouse model of human OS. NOD/SCID IL2-R-gamma -/- mice (The Jackson Laboratory), aged 4-6 weeks, were injected with firefly-luciferase and GFP-expressing SJSA-1 cancer cells (50,000 cells/mouse) in their left tibias, which was then allowed to progress and metastasize over a period of 5 days. At 5 days post-injection, baseline bioluminescence signal in the lungs was measured (Bruker Xtreme *In Vivo*) for each mouse, which were then assigned randomly into 3 treatment groups: Sham Control (PBS), diPTX pro-drug (0.18 mg/mL in 95% PBS / 5% DMSO), and the diPTX-loaded cationic PGC micelles (0.18 mg/mL diPTX in PBS). To deliver the treatments, a custom-made nebulization/anesthesia chamber with a vibrating-mesh nebulizer (Aerogen) was used to produce a fine inhalable mist (~1 micron droplet size) that the mice breathed in while under isoflurane anesthesia (Figure III.1). The nebulized doses, 1 mL in volume exposed to the mice over a period of about 20 minutes per mouse, were administered starting six days after the tumor injection and repeated 1, 2, 3, 4, 6, 8, and 10 days thereafter. Fluorescence imaging of the mice *in vivo* (ex. 760 nm / em. 830 nm) was performed to verify the uptake of the nanoparticles into the lungs 1 day following the first nebulization. Further bioluminescence imaging was performed on days 12 and 19 after engraftment in order to track the progression of the lung metastatic burden. On day 19, the mice were euthanized *via* CO_2 asphyxiation and dissected to recover the lungs and other organs. The lungs were inflation fixed by intratracheal instillation of 4% neutral buffered

formalin for 30 minutes, followed by submersion in 15% sucrose in PBS and then 30% sucrose for an additional 30 minutes each. The lungs were then carefully dissected into their 5 distinct lobes, placed in cryomolds with O.C.T. media (Tissue-Tek®, Sakura® Finetek), imaged for fluorescence (ex. 760 nm / em. 830 nm), and then snap frozen in a dry-ice and 100% ethanol slurry for cutting and imaging using confocal microscopy.

For microscopic analysis, the frozen tissue was sliced into 20 micron sections using a cryostat (Cryotome, ThermoFisher Scientific) at -15 °C. The sections were mounted onto slides and coverslipped with optical medium (Fluoromount-G, ThermoFisher Scientific). For some slides, DAPI was added to visualize the cellular nuclei. Slides were stored at 4 °C until imaging.

Confocal-microscope imaging (Fluoview FV1000, Olympus) was performed in order to evaluate the distribution of nanoparticles within the lung tissue with reference to the GFP-labeled tumors. Images were acquired using a 10× air objective with laser excitations at 488 nm (GFP) and 635 nm (NIR) along with a transmission light detection unit and Nomarski DIC to visualize the lung structures in high detail. Imaging of the entire lung slices was achieved with a motorized XY stage (Prior Scientific) and the Olympus FV10 software. Mosaic stitches of the entire lung sections were analyzed for intensity using ImageJ.

3.3 Results and Discussion

3.3.1 Rational design of the diPTX-loaded PGC anticancer drug delivery system

Sugar-derived nanocarriers with near-infrared (NIR) labels and a cationic segment confined to either the interface between the hydrophilic shell and hydrophobic core or within the

core were synthesized and used to encapsulate diPTX pro-drugs with redox-responsive disulfide linkages (Figure III.3). In designing the nanocarrier structure to optimize cancer cell-specific drug delivery, PGC building blocks were selected due to their biocompatibility, degradability, functionality, and ability to assemble into versatile nanostructures with varied sizes, charges and functionalities.[20] Cationic moieties were incorporated within the PEG-protected nanocarriers to allow negatively-charged GSH to more readily access the core domain and to interact with the encapsulated diPTX, realizing preferential drug release in cancer cells with high GSH concentrations, while simultaneously increasing the tumor penetration ability and substantially reducing toxicity typically associated with cationic nanocarriers.[86-87] Once the disulfide bond in the diPTX pro-drug is cleaved by a reducing agent, the thiol-terminated PTX derivative (PTX-SH) undergoes hydrolysis to release the free drug.[85] In addition, the dimeric size of the pro-drug was expected to allow for enhanced containment by the nanocarrier to provide for sustained release. Co-assembly of non-ionic and cationic polymers was performed for the dual purposes of curtailing safety concerns associated with cationic polymers and tuning nanoparticle sizes.[86-87]

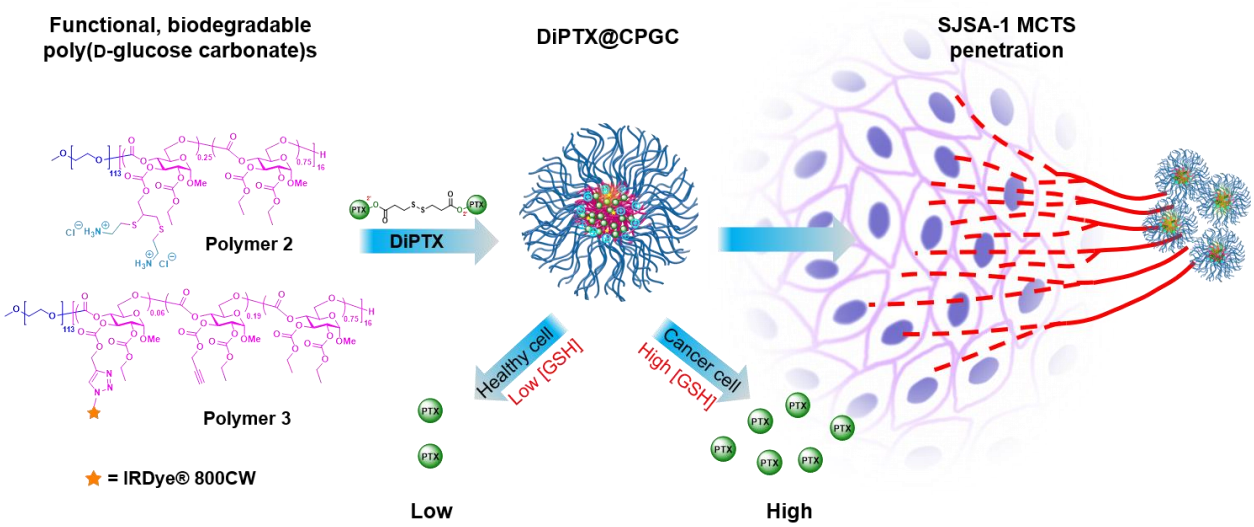

Figure III.3. Schematic illustration of the co-assembly of polymer 2 and polymer 3 with diPTX, and redox-responsive drug release to enable treatment of SJSA-1 multicellular tumor spheroids (MCTSs) with improved penetration, relative to free drug PTX, and pro-drug diPTX.

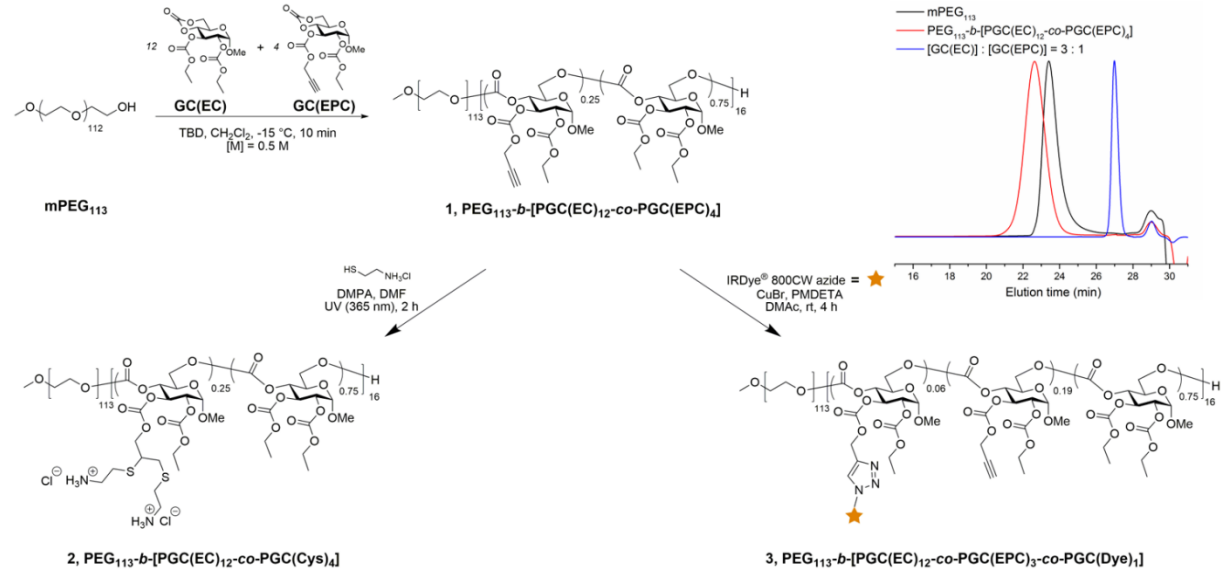

Figure III.4. Synthesis of polymer 1, PEG_{113}-*b*-[$PGC(EC)_{12}$-*co*-$PGC(EPC)_4$] by ROP of GC(EC) and GC(EPC), followed by post-polymerization modification *via* a thiol-yne click reaction with cysteamine hydrochloride to prepare the cationic polymer 2, PEG_{113}-*b*-[$PGC(EC)_{12}$-*co*-$PGC(Cys)_4$], or *via* CuAAC to afford NIR dye-labeled polymer 3, PEG_{113}-*b*-[$PGC(EC)_{12}$-*co*-$PGC(EPC)_3$-*co*-$PGC(Dye)_1$]. Inset: Normalized SEC traces of polymer 1, macroinitiator $mPEG_{113}$, and a mixture of the bicyclic carbonates GC(EC) and GC(EPC) with a molar ratio of 3:1 in THF.

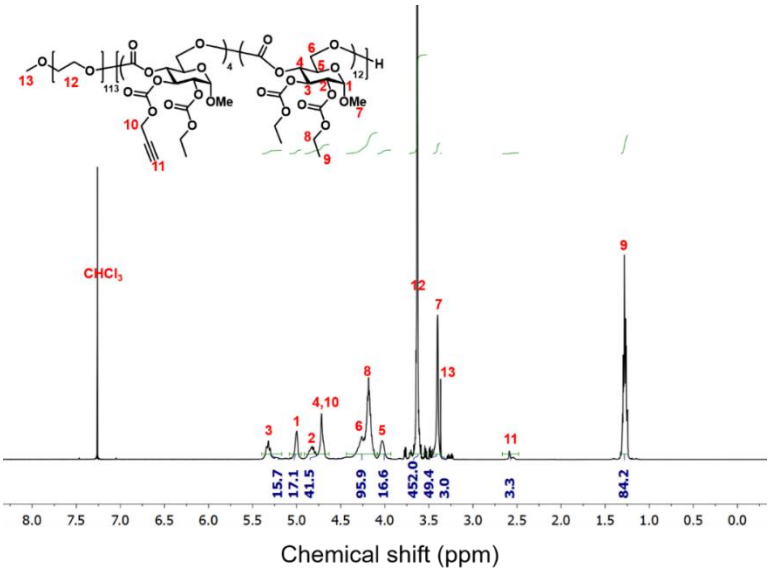

Figure III.5. ^{1}H NMR spectrum of PEG_{113}-*b*-[$PGC(EC)_{12}$-*co*-$PGC(EPC)_4$] (polymer **1**) (500 MHz, $CDCl_3$).

3.3.2 Synthesis and post-polymerization modification of PEG-*b*-PGCs

The functional and degradable diblock terpolymer **1**, PEG_{113}-*b*-[$PGC(EC)_{12}$-*co*-$PGC(EPC)_4$], was synthesized by rapid organocatalyzed ring-opening polymerization (ROP) of the bicyclic glucose carbonates methyl-2,3-*O*-ethyloxycarbonyl-4,6-*O*-carbonyl-α-D-glucopyranoside GC(EC) and methyl-2-*O*-ethyloxycarbonyl-3-*O*-propargyloxycarbonyl-4,6-*O*-carbonyl-α- D-glucopyranoside GC(EPC) at -15 °C in dichloromethane (DCM) with $mPEG_{113}$ as the macroinitiator and 1,5,7-triazabicyclo[4.4.0]-dec-5-ene (TBD) as the organocatalyst (Figure III.4). The monomer feed ratio [GC(EC)] : [GC(EPC)] was set to 3 : 1 to provide sufficient hydrophobicity and functionality. The reaction was quenched by addition of Amberlyst 15 H-form resin after 10 min, and size exclusion chromatography (SEC) (Figure III.4 inset) of the

crude product showed no remaining monomers, indicating quantitative conversions of both monomers. The lower retention time of polymer **1** relative to $mPEG_{113}$ confirmed the successful chain extension to afford the expected diblock terpolymer. SEC further revealed monomodal molecular weight distribution and low dispersity ($Đ$ = 1.12), demonstrating the well-defined structure of the diblock terpolymer. The number-average molecular weight (M_n) and degree of polymerization (DP_n) of each monomer were calculated from the ^{1}H NMR spectrum (Figure III.5) acquired after isolation of the polymer by precipitation, by comparing the integration of the CH_2CH_2O proton resonances (3.63 ppm) from the macroinitiator with the intensities of the resonances of protons attached to the anomeric carbons (5.01 ppm) and alkyne groups (2.59 ppm) in the PGC segment. Differential scanning calorimetry (DSC) revealed two glass transition temperatures (T_g) at -24 and 98 °C, corresponding to the mPEG and PGC segments, respectively.

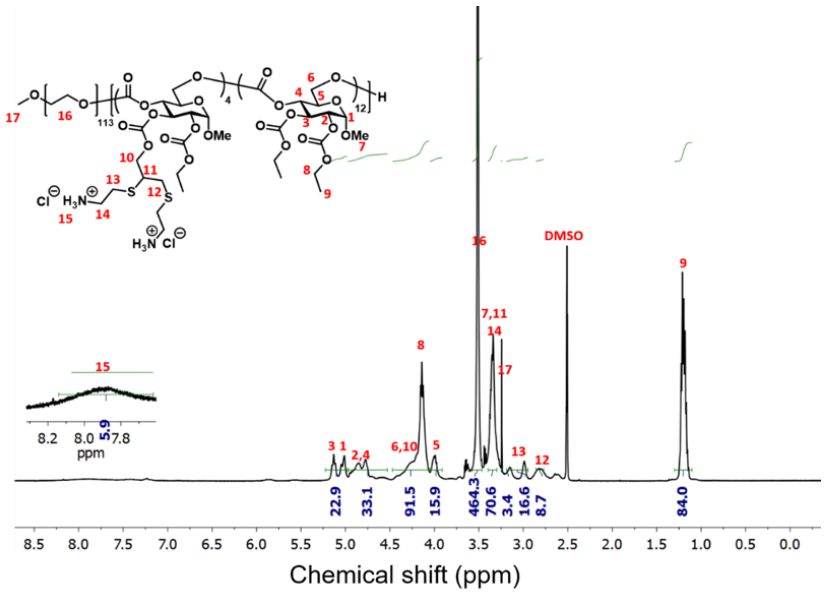

Figure III.6. ^{1}H NMR spectrum of PEG_{113}-*b*-[PGC(EC)$_{12}$-*co*-PGC(Cys)$_4$] (polymer **2**), with an inset showing an expansion of the region where the protonated amine resonance is observed (500 MHz, DMSO-d_6).

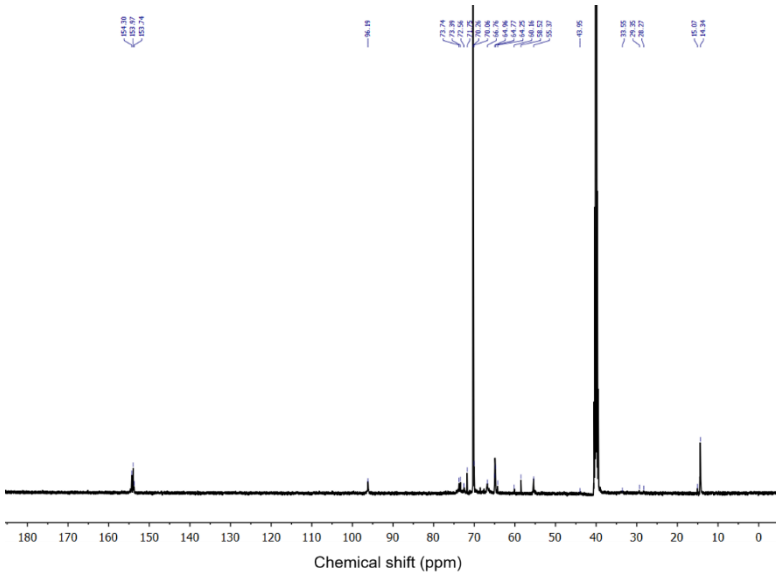

Figure III.7. ^{13}C NMR spectrum of PEG$_{113}$-*b*-[PGC(EC)$_{12}$-*co*-PGC(Cys)$_4$] (polymer **2**) (126 MHz, DMSO-d_6).

The cationic terpolymer **2**, PEG$_{113}$-*b*-[PGC(EC)$_{12}$-*co*-PGC(Cys)$_4$], was prepared by post-polymerization modification of **1** *via* photoinitiated thiol-yne click reaction with a large excess of cysteamine hydrochloride (20 equivalents relative to alkyne groups) (Figure III.4). The reaction mixture was dialyzed against nanopure water at 4 °C for 3 d to remove excess thiol and photoinitiator, then lyophilized to afford the product as a white powder in 95% yield. The presence of the cysteamine proton resonances at 2.66, 2.82, 2.99 and 7.88 ppm in the ^{1}H NMR spectrum and the disappearance of the alkyne carbon resonances at 78.91 and 77.70 ppm in the ^{13}C NMR spectrum indicated the consumption of the alkyne groups (Figure III.6, 7). Fourier transform infrared (FT-IR) spectroscopy further confirmed the consumption of the alkynes and the introduction of amine groups (Figure III.8). Glass transitions of polymer **2** were observed at -25 and 92 °C in DSC thermograms, suggesting that self-assembled nanostructures would possess flexibility within a PEG shell (T_g = -25 °C) and stability of the PGC-based core (T_g = 92 °C).

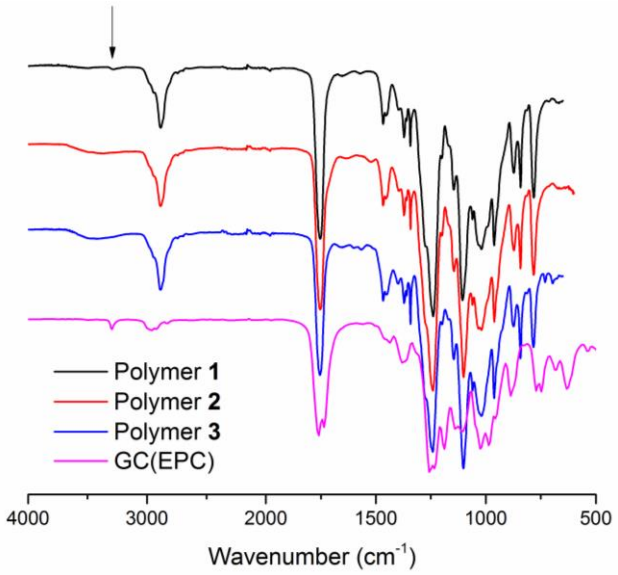

Figure III.8. FT-IR spectra of polymers **1**-**3** and bicyclic carbonate monomer **GC(EPC)** with alkyne C-H stretch highlighted.

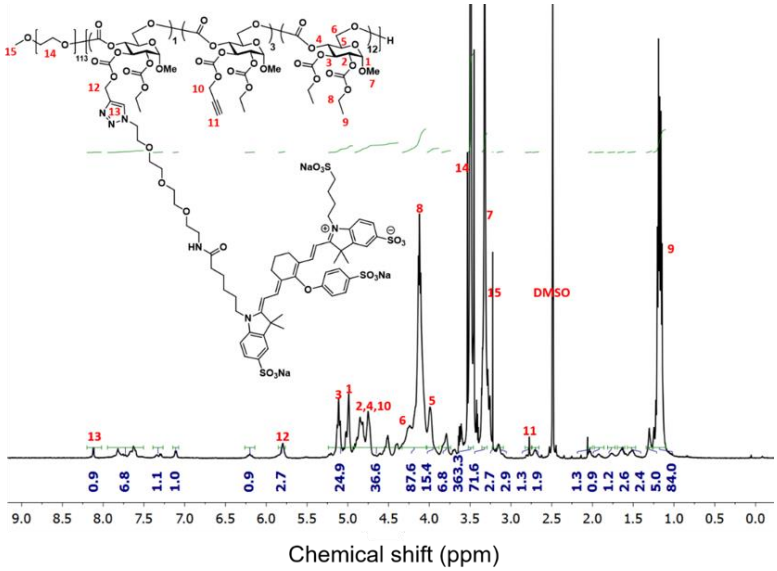

Figure III.9. ^{1}H NMR spectrum of PEG$_{113}$-*b*-[PGC(EC)$_{12}$-*co*-PGC(EPC)$_{3}$-*co*-PGC(Dye)$_{1}$] (polymer **3**), with the unassigned peaks attributed to IRDye® 800CW (500 MHz, DMSO-d_6).

The NIR-labeled polymer **3** was obtained by grafting the hydrophilic NIR dye, IRDye® 800CW azide, to polymer **1** *via* copper-catalyzed alkyne-azide coupling (CuAAC) in *N*,*N*-dimethylacetamide (Figure III.4). The reaction mixture was filtered through a neutral alumina

column and dialyzed against Chelex® 100 resin in nanopure water for 4 d to remove copper species. Inductively coupled plasma-mass spectrometry (ICP-MS) confirmed the mass fraction of residual copper to be less than 10 ppm. The appearance of a new resonance corresponding to the triazole proton at 8.12 ppm (Figure III.9) indicated successful conjugation of the IRDye® 800CW to the polymer.

3.3.3 Preparation of diPTX-loaded PGC nanoparticles

PGC nanoparticles loaded with diPTX was achieved utilizing the previously described nanoprecipitation method.[82, 88] Briefly, a series of mixtures of the non-ionic polymer **1** and cationic polymer **2** at predetermined mass ratios was first dissolved with diPTX (10 wt%) in DMSO, and then added dropwise into nanopure water with vigorous stirring to form diPTX-loaded nanoparticles (conc. (polymer) = 1 mg/mL) with 1 vol% DMSO. DiPTX loading was determined using high-performance liquid chromatography (HPLC), while the size, morphology, and surface charge were characterized by dynamic light scattering (DLS), atomic force microscopy (AFM), transmission electron microscopy (TEM) and electrophoretic light scattering (Figure III.10, 11).

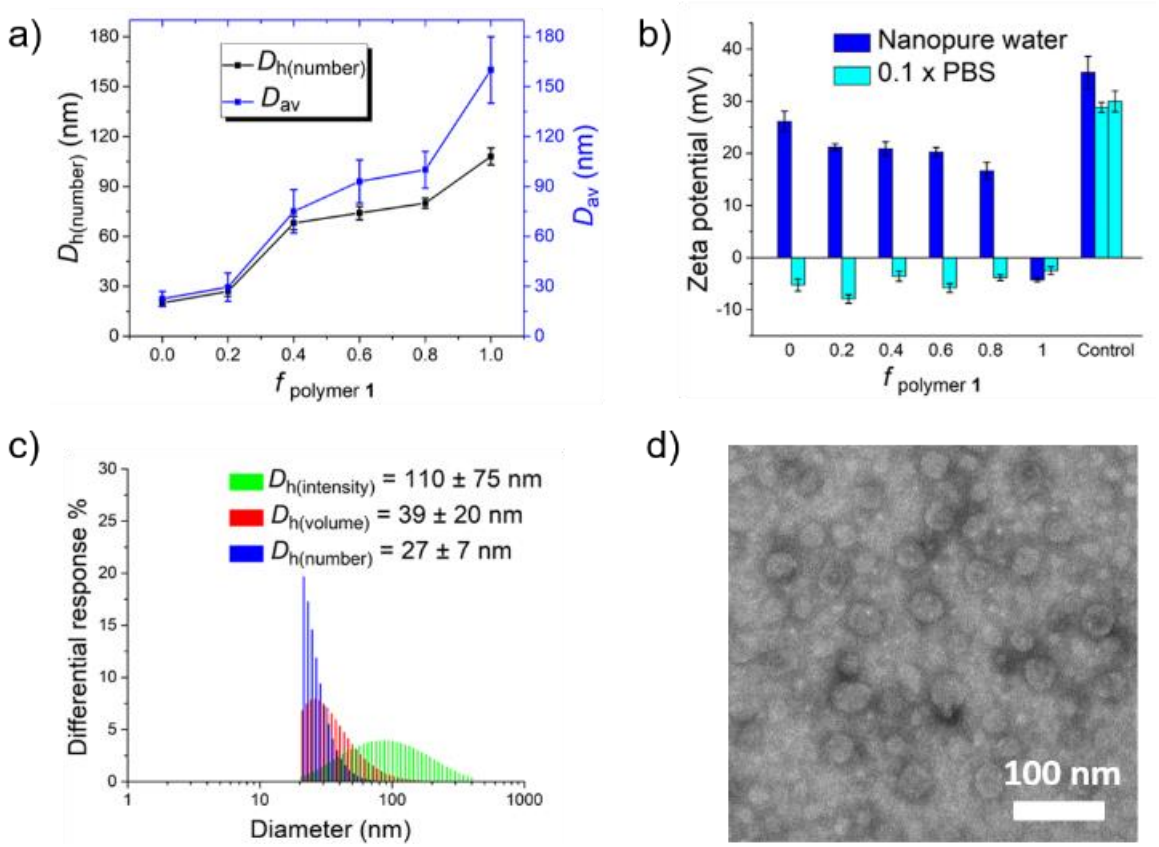

Figure III.10. Characterization of diPTX@CPGC. a) D_h and D_{av} as a function of $f_{\text{polymer 1}}$, determined from DLS and TEM, respectively. b) Zeta-potential of diPTX@CPGC in nanopure water and 0.1× PBS as a function of $f_{\text{polymer 1}}$. Controls zeta potential measurements were acquired on unloaded PGC(EC)-*b*-PGC(Cys) in nanopure water and 0.1× PBS, and on physical mixtures of PGC(EC)-*b*-PGC(Cys) with $mPEG_{113}$ in 0.1× PBS, from left to right. c) Number-, intensity- and volume-based hydrodynamic diameter of diPTX@CPGC ($f_{\text{polymer 1}}$ = 0.2) in nanopure water measured by DLS. d) TEM images of diPTX@CPGC ($f_{\text{polymer 1}}$ = 0.2) negatively stained by 1 wt% phosphotungstic acid (PTA) aqueous solution (10 µL).

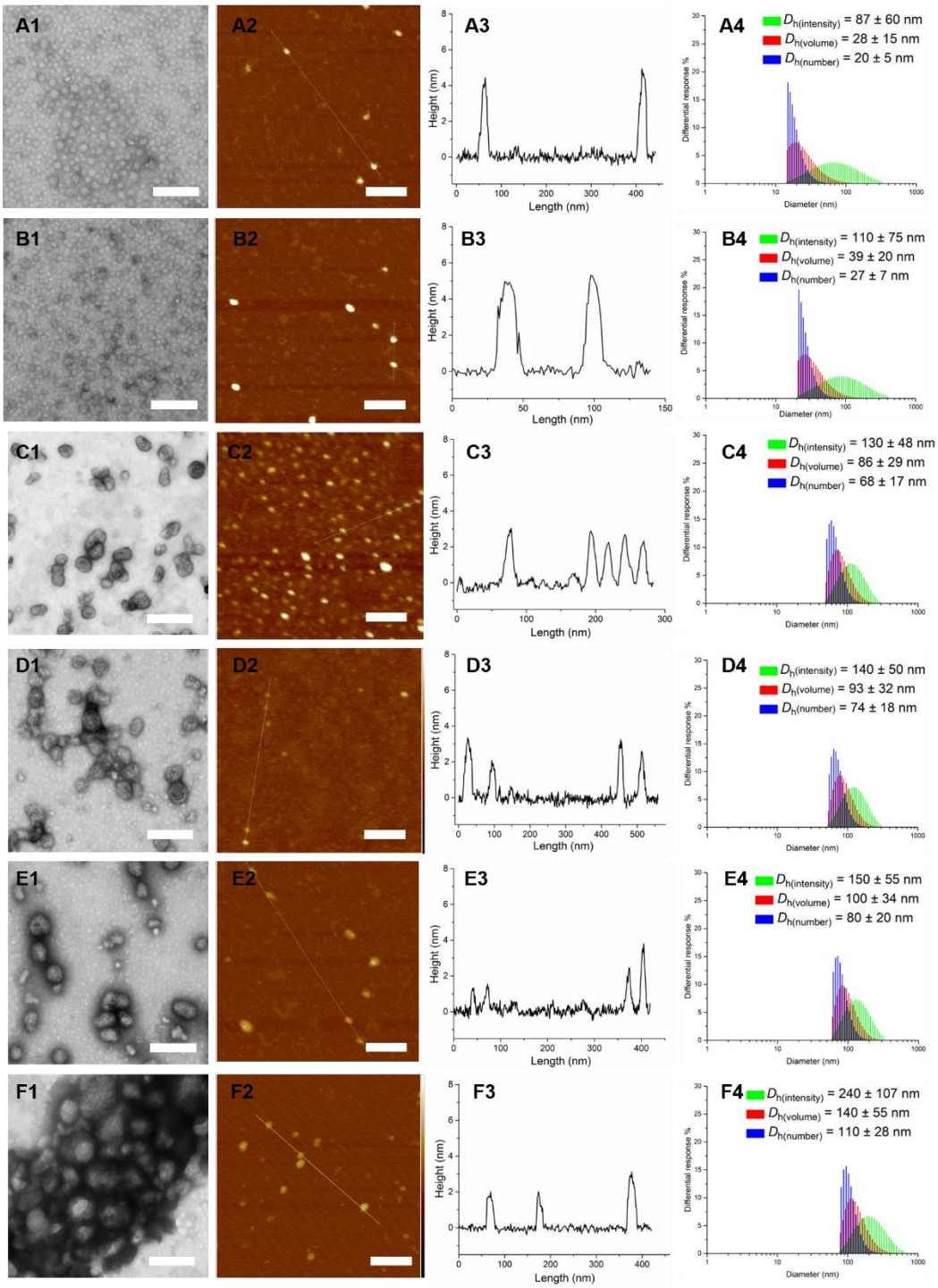

Figure III.11. Characterization of the nanoparticles prepared by loading diPTX in mixtures of polymers **1** and **2** by TEM (A1, B1, C1, D1, E1, and F1), AFM (A2, B2, C2, D2, E2, and F2), AFM height (A3, B3, C3, D3, E3, and F3) and DLS (A4, B4, C4, D4, E4, and F4) with $f_{\text{polymer }\mathbf{1}}$ to be 0, 0.2, 0.4, 0.6, 0.8 and 1 from top to bottom. The scale bars in the TEM images represent 200 nm, while those in the AFM images represent 100 nm.

HPLC revealed that the physical encapsulation of 10 wt% diPTX was highly effective, with efficiencies > 98%. Although this standard loading of 10 wt% diPTX was employed, preliminary experiments were found to allow for higher diPTX loading, to levels of *ca*. 40 wt%. As depicted in Figure III.11, DLS showed unimodal size distributions of all nanocarriers, suggesting the incorporation of polymer **1** and polymer **2** into the same nanostructures. The number-average hydrodynamic diameter ($D_{h(number)}$) of the diPTX-loaded nanoparticles increased from 20 ± 5 nm to 110 ± 28 nm (Figure III.10a) as the mass ratio of the non-ionic polymer **1** ($f_{\text{polymer 1}}$) increased from 0 to 1, owing to the increased hydrophobic content. TEM and AFM images of diPTX-loaded nanoparticles with $f_{\text{polymer 1}}$ of 0 and 0.2 showed circular structures with average diameters (D_{av}) of 23 ± 5 and 30 ± 8 nm, respectively (counting > 50 nanoparticles) and heights of 4 ± 1 and 5 ± 1 nm (counting > 50 nanoparticles), respectively, suggesting the formation of micellar structures. However, as the $f_{\text{polymer 1}}$ increased above 0.2, the morphology of the diPTX-loaded nanocarriers transformed from micelles to vesicles, indicated by the double layer structures observed in the TEM images, as well as the lower heights (3 ± 1 nm) in the AFM images (Figure III.11). The hydrophobic diPTX pro-drug was anticipated to be encapsulated in the core of the micelles or in the double layer of the vesicles. Zeta potential values (ξ) were characterized in nanopure water, 0.1× phosphate-buffered saline (PBS), and in 10 mM $NaCl_{(aq)}$. As shown in Figure III.10b, the ξ values measured for the five cationic nanocarriers were positive, ranging from 28 ± 2 mV to 16 ± 1 mV in nanopure water, while negative values of -5 ± 2 mV were obtained with the non-ionic nanoparticles, a common phenomenon observed for neutral polymer assemblies.[19, 89] In both 0.1× PBS and 10 mM $NaCl_{(aq)}$ (data not shown), all nanocarriers showed negative ξ (< -10 mV), indicating PEG-like surface characteristics. As a control, the cationic PGC block polymer PGC(EC)-*b*-PGC(Cys) without the PEG segment (Figure III.2)

showed positive ξ in all of these solutions, even when physically mixed with $mPEG_{113}$ at a mass ratio of 1:1, further confirming that the positively-charged segment was protected by PEG. Recent studies suggest that cancer nanomedicines with smaller sizes exhibit enhanced *in vivo* performance due to greater tumor penetration.[76] Thus, micelles with $f_{\text{polymer 1}} = 0.2$ were chosen for subsequent release and cytotoxicity studies, as their size was less than 30 nm and ξ was relatively small (Figure III.10c, 10d). Additionally, the small ratio of non-ionic, alkyne-functionalized polymer **1** provided the possibility for further modification or crosslinking.

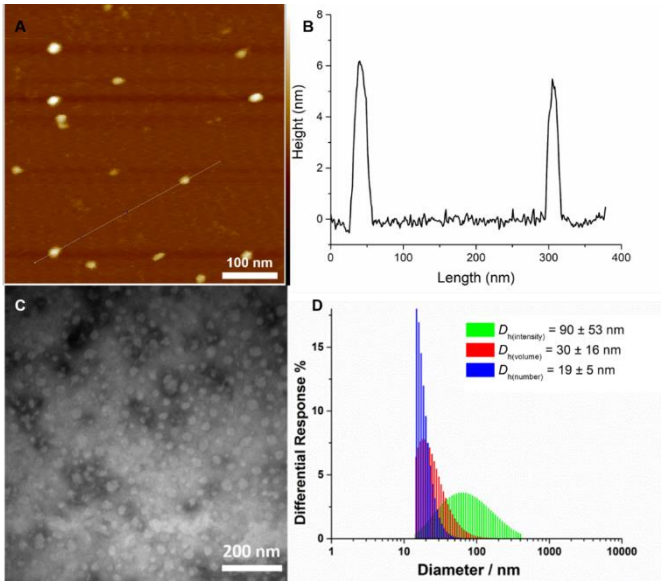

Figure III.12. Characterization of the nanoparticles with diPTX loaded in PGC(EPC)-*b*-PGC(EC)-*g*-PEG_{2k} by AFM (a), AFM height (b), TEM (c) and DLS (d).

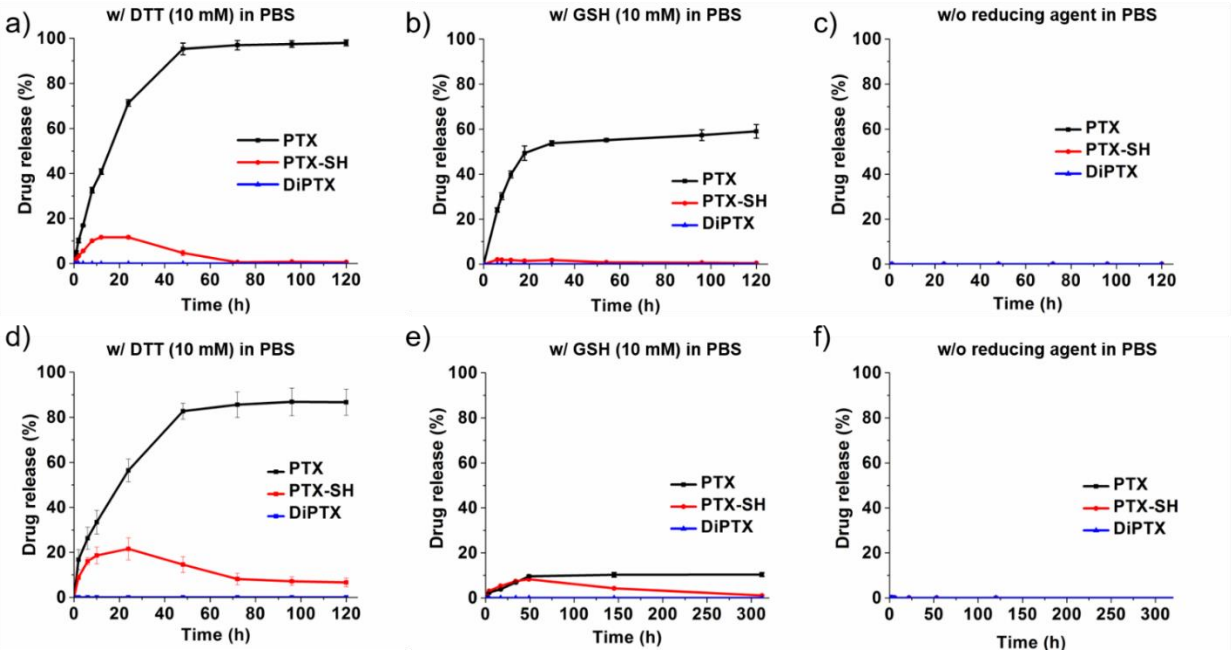

Figure III.13. Release of PTX, PTX-SH, and diPTX from (a, b, and c) diPTX-loaded cationic micelles ($f_{\text{polymer 1}}$ = 0.2), and (d, e, and f) diPTX-loaded PGC(EPC)-*b*-PGC(EC)-*g*-PEG_{2k} micelles at 37 °C in PBS containing (a and d) 10 mM DTT, (b and e) 10 mM GSH, and (c and f) no reducing agents, measured in triplicate. Error bars indicate standard deviation.

3.3.4 Evaluation of the drug release kinetics

The drug release profiles of diPTX@CPGC were investigated in PBS in the presence or absence of reducing agents. The non-ionic polymer PGC(EPC)-*b*-PGC(EC)-*g*-PEG_{2k} (Figure III.2) reported recently by our group[20] was utilized as a control to demonstrate the benefit of the positive charges residing at the core-shell interface on the diPTX release profile, as these nanocarriers exhibited similar sizes and physicochemical properties, as characterized by DLS, TEM, AFM (Figure III.12) and DSC. For the drug release studies, the micelle solutions were diluted to yield diPTX concentrations of *ca.* 100 µg/mL, which were confirmed by HPLC. The diPTX-loaded micelle solutions were then transferred into dialysis cassettes (MWCO 10 kDa) and dialyzed against PBS (pH 7.4, 37 °C) containing either 10 mM DTT, 10 mM GSH or no

reducing agent. The drug release profiles were obtained by monitoring the concentrations of PTX, PTX-SH, and diPTX in the surrounding PBS solution as a function of time, and the percent drug release was calculated based on the PTX equivalents determined by HPLC. As depicted in Figure III.13, no diPTX release was observed in any of the solutions, consistent with results recently reported for other dimeric pro-drugs.[82] No significant release of PTX or PTX-SH was observed from either the cationic (Figure III.13c) or non-ionic PGC micelles in the absence of reducing agents (Figure III.13f). In the presence of 10 mM DTT, diPTX@CPGC afforded sustained and controlled release of free PTX, which plateaued at almost complete drug release within 3 d, during which the concentration of PTX-SH increased initially and later dropped (Figure III.13a). Similar sustained and controlled release of free PTX was achieved in 10 mM $GSH_{(aq)}$, reaching a plateau at *ca*. 55% release in 2 d (Figure III.13b). The incomplete release may be due to reduced interaction of core-encapsulated diPTX with the relatively bulky reducing agent GSH. Yet, such release profiles, wherein relatively fast redox-responsive drug release over 2 d, followed by slower and more sustained drug release expected upon degradation of the nanoparticles in the human body, are anticipated to be quite beneficial for drug delivery. PTX release from the non-ionic PGC micelles in the presence of 10 mM DTT was slightly slower than that from diPTX@CPGC, reaching a plateau at *ca.* 85% release within 3 d and 50% release in *ca*. 20 h (Figure III.13d), slightly longer than the *ca.* 16 h required for 50% drug release from diPTX@CPGC. The PTX release rate from the non-ionic PGC micelles in the presence of 10 mM GSH, however, was much slower with only *ca.* 10% PTX release in 2 d and no significant increase over time (Figure III.13e), which may limit the potential of the non-ionic formulations as efficient drug delivery systems. Taken together, the structure with positive charges confined to either the core-shell interface or within the core of the nanocarriers showed advantageous

GSH-mediated drug release profiles over analogous non-ionic nanocarriers. Thus, diPTX@CPGC were investigated further to evaluate anticancer efficacy *in vitro*.

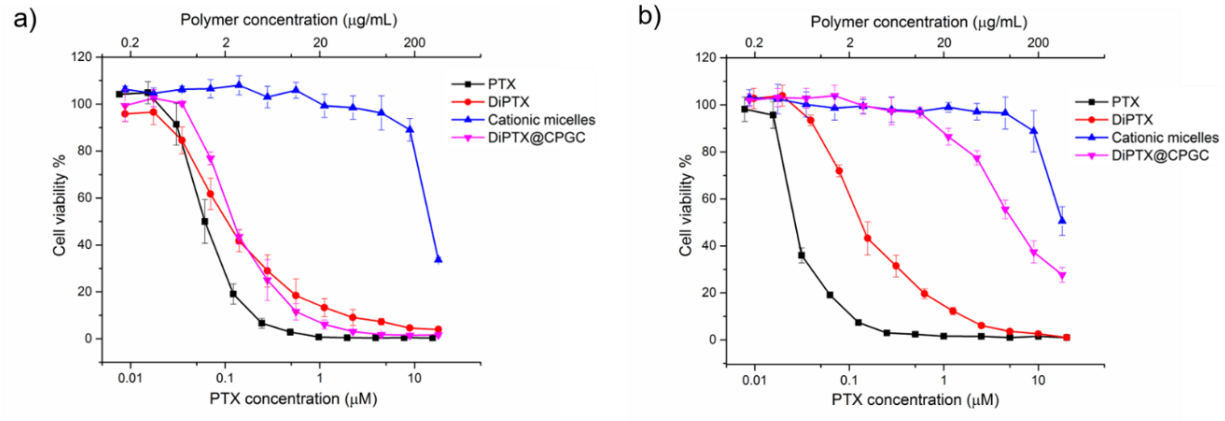

Figure III.14. Cytotoxicity of PTX, diPTX, cationic PGC micelles, and **diPTX@CPGC** in (a) SJSA-1 and (b) MC3T3 cells. Cell viabilities are reported as an average of three measurements, and error bars represent standard deviation.

3.3.5 Evaluation of nanoparticle toxicity

The *in vitro* cytotoxicity of diPTX@CPGC was evaluated in SJSA-1 and MC3T3 cell lines, and compared to PTX (as a Taxol-mimicking formulation; Cremophor EL and ethanol, 1:1 v/v), diPTX (prepared similarly to the PTX formulation, Cremophor EL and ethanol, 1:1 v/v), and cationic PGC micelles without diPTX (Figure III.14). The cationic micelles exhibited negligible toxicity in both cell lines below 0.2 mg/mL, indicating the protective effect of PEG, which has been reported to improve the biocompatibility of cationic nanoparticles.[19-20] In contrast, our earlier work with cationic PGC-based micelles, lacking a PEG shell, began showing reduction in cell viability at concentrations ranging from 0.05 to 0.1 mg/mL in RAW and MC3T3

cell lines.[20] In SJSA-1 cells (Figure III.14a), diPTX@CPGC exhibited similar cytotoxicity to diPTX, which was slightly less toxic than the Taxol-mimicking formulation. The reduced cytotoxicity of the diPTX formulations, in comparison with PTX, may be attributed to the relatively slow free drug formation and release. As a result of the redox-responsive drug release mechanism, the cytotoxicity difference between diPTX and PTX was higher in non-cancerous cells, which are expected to have a less reducing intracellular environment (Figure III.14b). Accordingly, a higher IC_{50} value (0.14 mM PTX) was observed for diPTX relative to that measured for PTX (0.03 mM) in MC3T3 cells. The toxicity of diPTX@CPGC was further reduced in the MC3T3 cells compared to unencapsulated diPTX and PTX, with an IC_{50} value of *ca*. 5 mM, demonstrating selectivity for killing cancer cells over non-cancerous cells. These studies, thus, confirm the advantages of diPTX@CPGC as cancer-selective agents and highlight the potential to reduce side effects in healthy cells without substantially sacrificing potency.

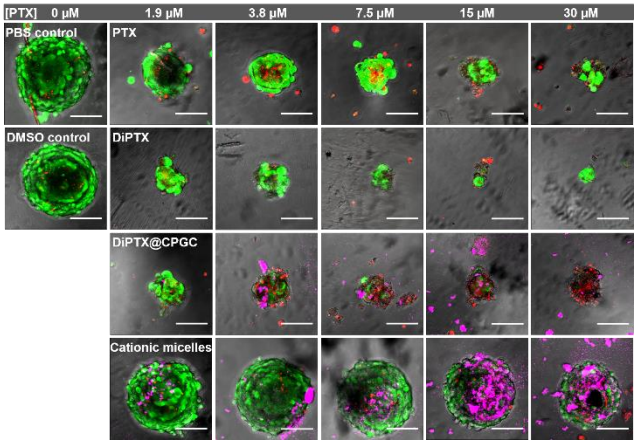

Figure III.15. CLSM images of SJSA-1 MCTSs after treatment with PTX, diPTX, diPTX@CPGC containing 1.9-30 μM PTX, and cationic PGC micelles with equivalent polymer concentrations as used for the diPTX@CPGC, and PBS and DMSO controls (green: live cells, red: dead cells, purple: micelles). Scale bars represent 100 μm.

3.3.6 Nanoparticle toxicity in SJSA-1 spheroids

Multicellular tumor spheroids (MCTSs) are versatile three-dimensional models for studying tumor biology and screening cancer therapeutics due to the MCTSs possessing a similar morphology, biological microenvironment, and response to chemotherapeutics as solid tumors *in vivo*.[90-92] To test the effects of diPTX@CPGC on MCTSs, SJSA-1 human OS cancer cell-derived MCTSs were established on low-binding U-shaped microplates, incubated with micelles or controls, and evaluated as an *in vitro* model to assess penetration capability and cell proliferation inhibition (Figure III.3, 15). The MCTS growth inhibition provided by the different formulations, *i.e.*, PTX, diPTX, diPTX@CPGC, and cationic PGC micelles (no drug/pro-drug), was monitored by confocal laser scanning microscopy (CLSM), and the concentrations of PTX in the drug/pro-drug formulations were determined by HPLC (Figure III.16). PTX showed significant antitumor efficacy at concentrations from 1.9-30 μM PTX, with MCTS sizes reduced to *ca*. 50% of the controls at 1.9 μM PTX and *ca*. 20% at 30 μM PTX. In comparison, the reduction of SJSA-1 MCTSs upon treatment with the diPTX pro-drug or diPTX@CPGC at 1.9 μM was similar, *ca*. 25% of the controls. At higher concentrations (3.8-30 μM PTX), the diPTX formulation reduced the MCTSs size to a greatest extent, achieving *ca*. 10% of the control tumor size with formulations containing 30 μM PTX, while the diPTX@CPGC reduced the MCTSs to a similar extent (*ca*. 20-25%) for all concentrations. However, the live/dead staining results demonstrated that the remaining MCTSs incubated with diPTX still contained live cells at even the highest concentrations. In contrast, diPTX@CPGC appeared to kill all cells at the highest concentration, likely resulting from improved penetration into the core of the MCTS. Thus, the best killing performance was achieved with diPTX@CPGC, compared with the other two

drug/pro-drug formulations. The cationic PGC micelles without diPTX exhibited only slight anti-MCTS effect at the highest polymer concentration of 0.28 mg/mL, in which the amount of polymer was equivalent to that in the 30 μM PTX formulation of diPTX@CPGC.

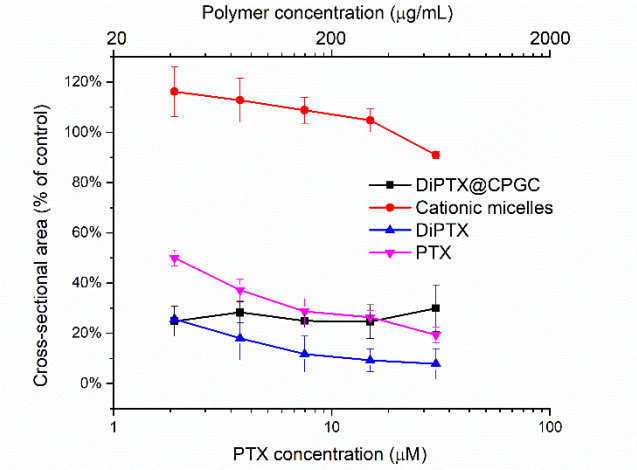

Figure III.16. Growth inhibition of the SJSA-1 MCTSs by PTX, diPTX, diPTX@CPGC and the cationic PGC micelles (no drug/pro-drug) 7 d after addition of the formulations. Cross sectional areas are reported as an average of four measurements, and error bars represent standard deviation.

3.3.7 Nanoparticle efficacy against OS lung metastases

An orthotopic xenograft mouse model was evaluated in order to determine the antitumor efficacy against OS lung metastases. NOD/SCID IL2-R-gamma -/- mice (aged 4-6 weeks) with established lung metastases were nebulized with different formulations, including Sham Control (PBS), diPTX pro-drug (0.20 mg/mL in 95% PBS / 5% DMSO), and diPTX@CPGC (0.20 mg/mL diPTX in PBS) (Figure III.1). DMSO was necessary in order to obtain a stable suspension for the diPTX pro-drug by itself, due to its highly hydrophobic nature. The lung

bioluminescence signal of mice treated with micelles showed a ~40% reduction in the growth of the lung metastases over the study, relative to control group, while the ones treated with free diPTX showed no reduction on the lung metastases (Figure III.17a). Possibly due to enhanced penetration and/or better retention in the lung, diPTX@CPGC exhibited a higher antitumor efficacy in the lung than did free diPTX. The micelles also had a non-significant trend towards lower tumor burden at the primary site of metastases over control and free diPTX (Figure III.17b).

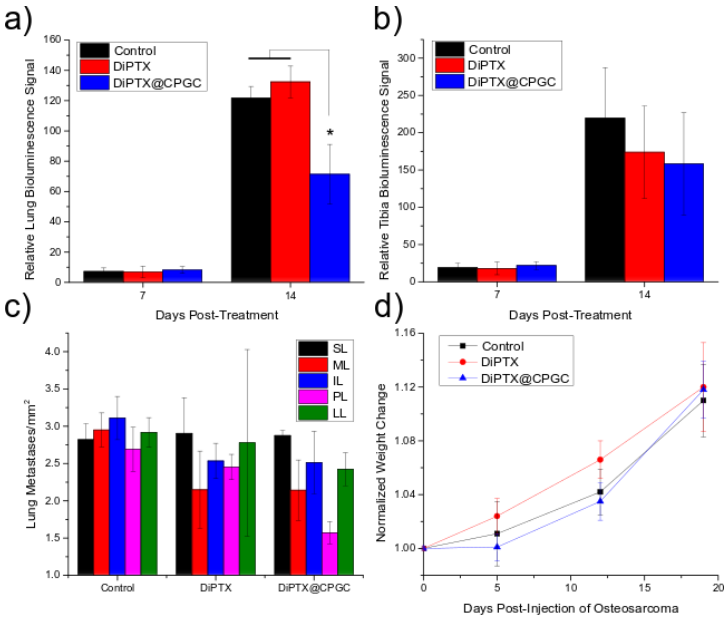

Figure III.17. Relative OS tumor burden as measured by bioluminescence imaging, normalized to the baseline signal for each mouse, from a) the lung metastases and b) the primary tumor in the tibia after 7 and 14 d from the start of treatment. A significant reduction in tumor progression was observed in the lungs for the mice treated with diPTX@CPGC ($p = 0.038$ vs. control, $p = 0.0114$ *vs*. diPTX, one-way ANOVA with Tukey's post-hoc comparison) but not with the free diPTX pro-drug ($p = 0.7839$). No significant differences were observed for the tumor burden in the tibia. c) Comparison of the metastases counted from histology of the different lung lobes *ex vivo* revealed a significant reduction in metastatic foci for the mice treated with diPTX@CPGC ($p = 0.02$ *vs*. control, two-way ANOVA with Tukey's post-hoc comparison). SL: superior lobe; ML: middle lobe; IL: inferior lobe; PL: post-caval lobe; LL: left lung. d) Tracking of the weight of the mice from the start of the study revealed no major differences among the groups.

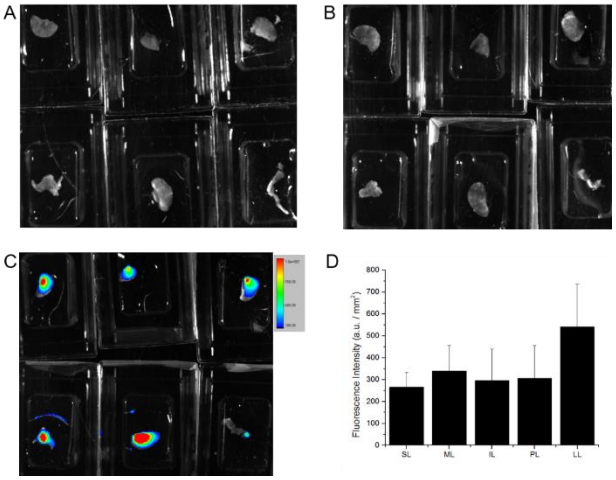

Figure III.18. *Ex vivo* fluorescence imaging showing the distribution of NIR signal (ex. 760 nm, em. 830 nm) in the lung lobes (from top left to bottom right: superior lobe, middle lobe, inferior lobe, and post-caudal lobe of right lung, left lung lobe, and trachea) following 14 days of nebulization treatments by control (A), diPTX pro-drug(B), and diPTX@CPGC (C). Signal was well distributed throughout lung lobes of mice administered with diPTX@CPGC, whereas mice given control and diPTX pro-drug showed no signal. Some signal was also found in the trachea, though it is not distributed throughout. Measurement of the signal per area (D) reveals that the left lung lobes tended to have the highest quantity of micelles. SL: superior lobe; ML: middle lobe; IL: inferior lobe; PL: post-caval lobe; LL: left lung.

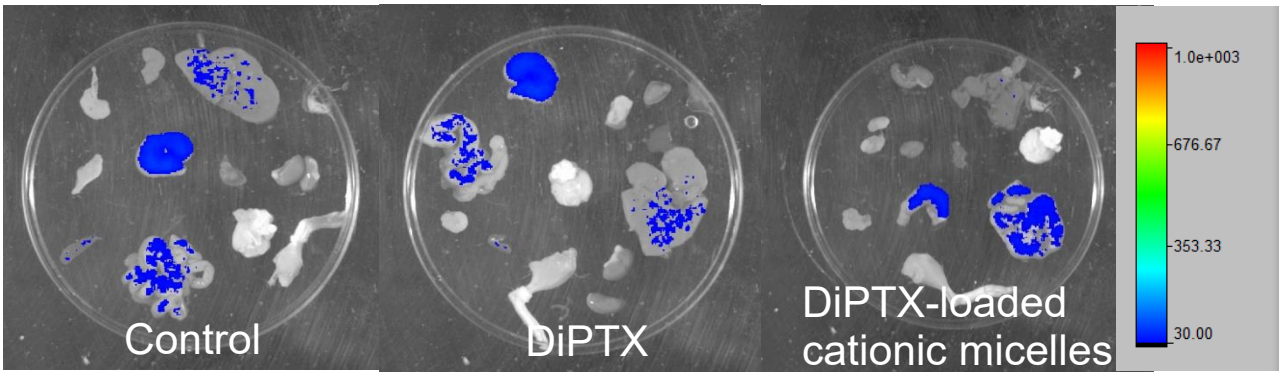

Figure III.19. *Ex vivo* fluorescence imaging showing the distribution of NIR signal (ex. 760 nm, em. 830 nm) in visceral organs and leg injected with tumor cells following 14 days of nebulization treatments. Some signal was found in the liver, stomach, and intestines, however this signal was found in all treatment groups and was likely background autofluorescence.

Thus, the diPTX@CPGC, appeared to predominantly exhibit a loco-regional anti-tumor effect in the lungs, with limited systemic effect. *Ex vivo* imaging supported this conclusion, as high concentrations of micelles were found in the lungs, but not other organs or primary tumor (Figure III.18, 19). While the lack of systemic antitumor effect may appear disadvantageous, we designed these nanocarriers for use as a potential replacement for the current osteosarcoma chemotherapy regimen, which is employed before and after surgical removal of the primary tumor in the bone.[93] Currently, systemic chemotherapy is employed regardless of detection of metastases and typically consists of high-dose methotrexate, cisplatin, and doxorubicin.[93] Systemic chemotherapeutic regimens, however, are associated with acute and chronic toxic effects,[94] including secondary malignancies.[95] Use of lung-specific anti-cancer therapy may allow for a reduction in systemic chemotherapy, and thus a reduction in these adverse effects.[96]

The *in vivo* bioluminescence data were supported by *ex vivo* measurements of the number of metastases per mm^2 of lung tissue (Figure III.17c) after the mice were euthanized 19 d from the injection of the SJSA-1 cells. Overall, diPTX@CPGC reduced the metastatic foci among the various lung segments ($p = 0.02$, two-way ANOVA with Tukey's post-hoc comparison). Individual analysis of each lung segment revealed that some lung sections displayed a greater reduction than others, with the superior lobe of the right lung showing the least reduction. This lobe also appeared to receive the least amount of nanoparticles by lung area (Figure III.18). Finally, the weights of the mice for the duration of the study (Figure III.17d) showed no significant differences between the groups, suggesting that the diPTX pro-drug and micelle formulations were well tolerated.

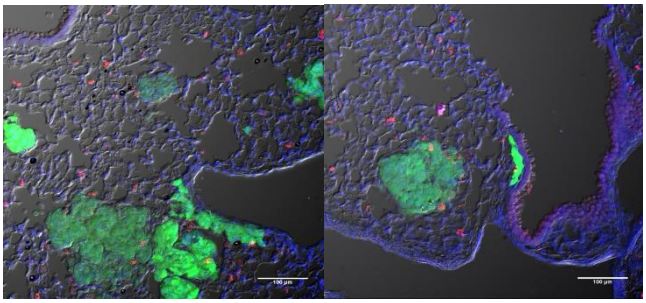

Figure III.20. CLSM images of lung histological sections of mice treated with diPTX@CPGC. NIR-labeled diPTX@CPGC (red) were found to reach the tumor sites and penetrate into the GFP-expressing SJSA-1 tumors (green). Additionally, diPTX@CPGC aggregates were found in the alveolar spaces, near blood vessels, and along the surfaces of the bronchioles, as revealed by DAPI nuclear staining (blue) and Nomarski DIC transmitted light imaging (greyscale).

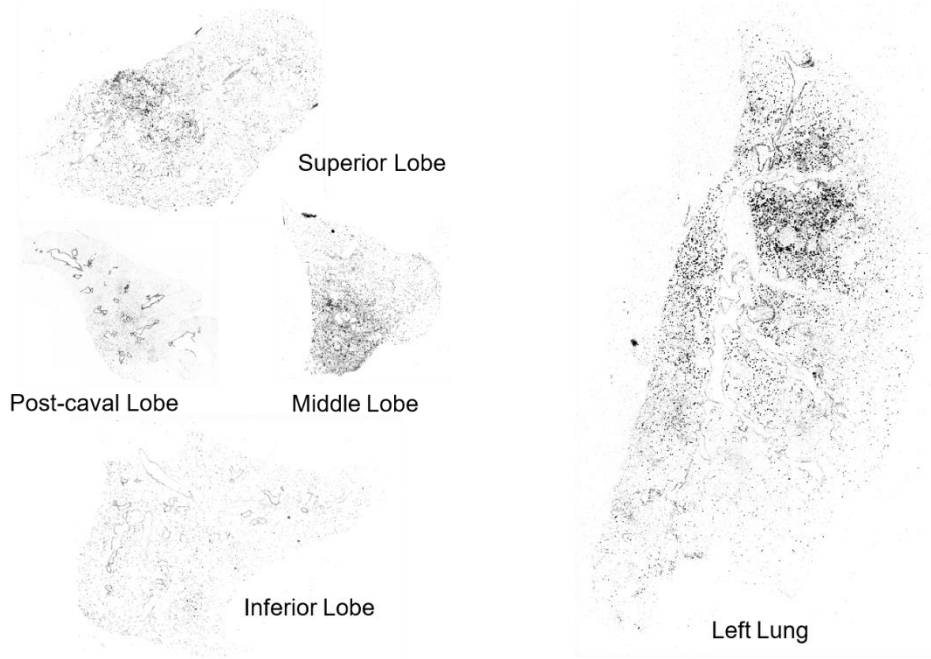

Figure III.21. CLSM mosaic images of the distribution of diPTX micelles in the various mouse lung lobes. Images were acquired using a 635 nm laser excitation source and automated scanning across the entire lobe. The image pixel values were inverted for contrast. Dark pixels represent areas with high fluorescence intensity. Most of the micelles appeared to accumulate near the main branching airways. However, micelles were able to reach deep into the lung as well.

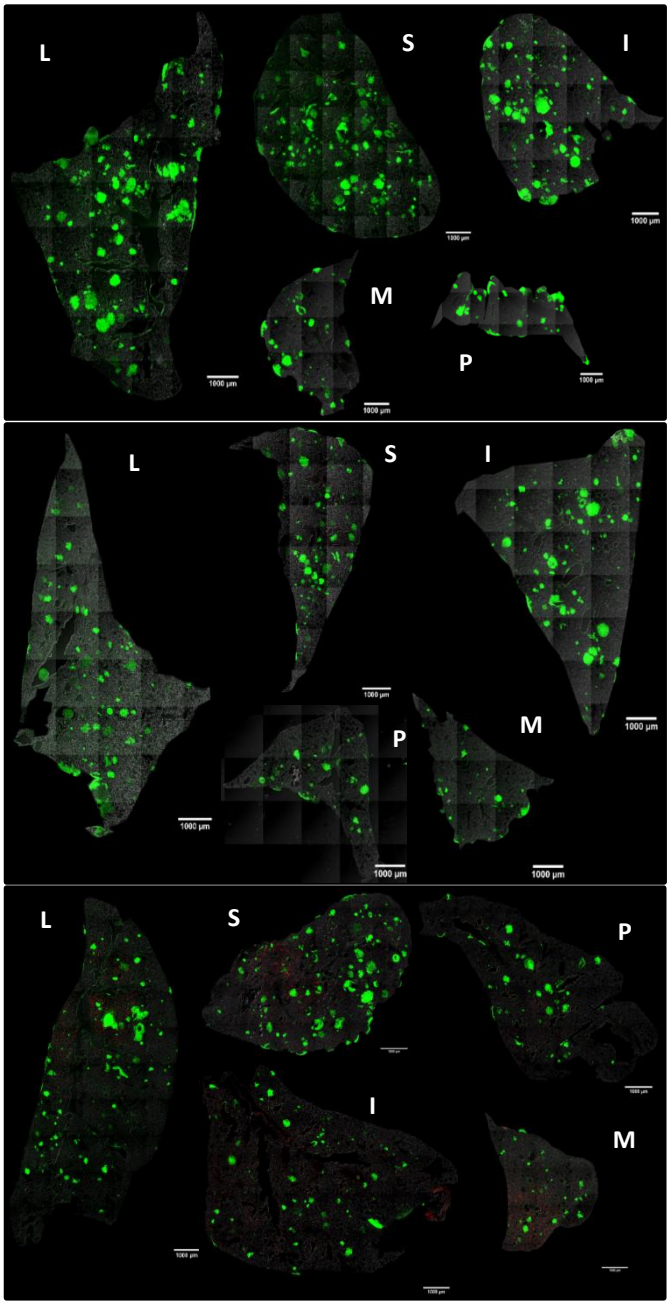

Figure III.22. CLSM mosaics of 20 μm slices from the various mouse lung lobes from mice administered control (top panel), diPTX (middle panel), or diPTX@CPGC (bottom panel). Fluorescence from the SJSA-1 tumors (green) and NIR labeled micelles (red) are overlayed on transmitted light images of the full lung sections. Distribution patterns of the nanoparticles showed higher abundance near the main branching airways. Additionally, nearby lung metastases appeared fewer in number and/or smaller in size, indicating a loco-regional activity. S: superior lobe; M: middle lobe; I: inferior lobe; P: post-caval lobe; L: left lung.

Evaluation of the NIR fluorescence signal for the lungs *ex vivo* (Figure III.18) revealed that a relatively higher dose of micelles reached the left lung lobe, as compared to the lobes in the right lung, though all lobes showed a discernible signal. Microscopic examination of 20 μm lung slices *via* CLSM revealed that the micelles were well distributed throughout the various structures of the lung, including alveolar spaces, bronchi, blood vessels, and penetrating into tumor sites (Figure III.20). Scans of the entire lung slices revealed that the micelles deposited primarily near the main branching airways, although micelles were found to extend to the periphery (Figure III.21, 22). Sections of the lungs with high deposition of nanoparticles also appeared to have fewer and/or smaller tumors, providing further evidence of localized anti-cancer effect. The deposition sites of the micelles appeared to show signs of aggregation (Figure III.20), with large spots of high micelle concentration relative to the measured size of individual particles. Similar aggregation patterns have been seen in other studies of lung delivery of nanoparticles.[4, 70, 97] The process and kinetics of this phenomenon, and whether it is specific to certain cell types, deserve further exploration. Importantly, the micelles did show an apparent ability to bypass the respiratory epithelium and access the tumors. Finally, only limited NIR signal was found in the other organs of the mice that were treated with micelle formulations (Figure III.19, 23), further confirming localized accumulation.

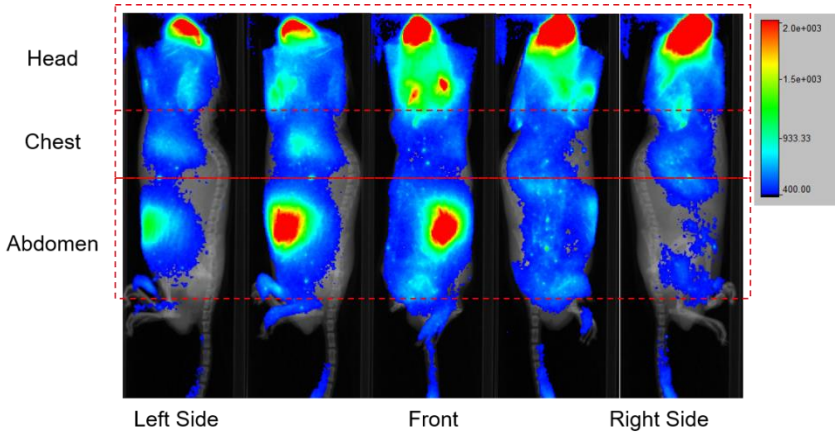

Figure III.23. *In vivo* fluorescence and x-ray imaging of diPTX@CPGC distribution 1 day following the first nebulized dose (ex. 760 nm, em. 830 nm). A high proportion of micelles was found near the nares and head of the mice, as well in what appeared to be the digestive tract, likely indicating that some of the nanoparticles were swallowed.

3.4 Conclusions

Two PGC-based block polymers and one dimeric PTX pro-drug were designed to be co-assembled into degradable, functional nanocarriers, where the chemistry of each component was defined to accomplish important tasks. The well-defined diblock terpolymer PEG-*b*-PGC(EC)-*co*-PGC(EPC) was synthesized by rapid ROP of glucose-derived monomers, with good biocompatibility, degradability and versatile functionality. Cationic moieties were introduced by thiol-yne click modification of the PGC segment, to construct nanocarriers with enhanced tumor penetration ability, while undesirable characteristics of cationic polymers was mitigated by the PEG shell. Disulfide-linked diPTX pro-drug was designed to allow for redox-triggered release in cancer cells with high GSH concentration, where the negatively-charged GSH can readily interact with encapsulated diPTX due to confined cationic charges in the shell-core interface or within core domain. In addition, enhanced nanocarrier containment of diPTX was achieved,

relative to PTX, to provide for sustained release. A series of nanocarriers with different sizes, surface charges, and morphologies was constructed by tuning the mass ratio of the amphiphilic cationic PGC and an analogous NIR-labeled non-ionic polymer employed in co-assembly. Given their suitable size, zeta potential and nanostructure, cationic PEG-*b*-PGC micelles with $f_{\text{polymer 1}}$ = 0.2 were selected for *in vitro* studies, which showed controlled and sustained *in vitro* PTX drug release in the presence of GSH or DTT. Cytotoxicity assays confirmed the biocompatibility of diPTX@CPGC, and significant selectivity of diPTX@CPGC for killing cancer cells over healthy cells. Studies in SJSA-1 MCTSs demonstrated improved tumor penetration ability and anticancer efficacy of diPTX@CPGC relative to Taxol-mimicking formulations. Therefore, the anticancer efficacy of diPTX@CPGC as inhaled chemotherapeutics was further evaluated in an orthotopic mouse model of human OS, with free diPTX and PBS as control groups. The lung bioluminescence signal of mice 14 d after treatment with diPTX@CPGC was significantly lower relative to the PBS controls, demonstrating their capability to slow the growth of lung metastases. Throughout the duration of the study, no significant differences were observed in the weights of the mice in the treatment and control groups, indicating the tolerance of the diPTX pro-drug and the PGC micelles. The micelles distributed appreciably throughout various structures of the lung, demonstrated by the *ex vivo* studies. The *ex vivo* study results also confirmed a reduction of tumor growth after treatment with diPTX@CPGC, indicating the promise of diPTX@CPGC as optimized anticancer therapeutic agents for treatment of OS lung metastases.

CHAPTER IV

FACILE CONSTRUCTION OF WELL-DEFINED JANUS NANOPARTICLES FROM FUNCTIONAL POLYPHOSPHOESTER BASED TRIBLOCK POLYMERS FOR ADVANCED SILVER THERAPEUTIC RELEASE

4.1 Introduction

Polymeric nanoparticles have been extensively investigated for therapeutic delivery, due to their unique properties such as the nanoscale size, high surface-to-volume ratio, and tunable physiological characteristics realized by their favorable chemical structures. However, the translation of nanomedicine research into clinical use is technically challenging due to a few concerns, *e.g.* the high cost of industrial manufacture arising from the sophisticated chemistry, and possible batch-to-batch variation of the physical and chemical properties in large-scale production[5-6].

Despite the rapid development of modern pharmaceutical research, bacterial infections remain a great threat to human lives throughout the world[21, 98]. Significant morbidity or mortality can be caused by serious infections without proper treatment. According to the Centers for Disease Control and Prevention (CDC) of the United States, more than two million patients are infected with antibiotic-resistant bacteria each year, which directly results in at least 23000 deaths nationwide[24]. To overcome treatment failures and increased severity of infections associated with the continually evolving resistant pathogens, development of novel antimicrobial therapeutics and innovative delivery approaches is of critical need[25, 99-100].

Silver has been used as a bactericidal material for thousands of years. Silver cations are demonstrated to be an effective antimicrobial agent with low toxicity to human tissues, while rare documented cases of bacterial resistance are reported. Given the broad-spectrum antimicrobial activity, high efficacy and relatively low cost, various silver-based antimicrobial agents have been commercialized. As the *in vivo* application of silver cation is limited due to its inactivation by salts and other biomolecules in the physiological condition, our group has developed a series of polymeric nanoscopic platforms to improve the bioavailability and efficacy of silver-based therapeutics. Shell crosslinked knedel-like nanoparticles (SCKs) comprised of poly(acrylic acid)-*block*-polystyrene (PS-*b*-PAA) were first investigated for the delivery of silver cations, which, though showing lower efficacy *in vitro*, exhibited significantly enhanced antimicrobial efficacy *in vivo* as compared to the free drug[101]. Furthermore, degradable and biocompatible polyphosphoester (PPE)-based nanocarriers were synthesized, which could reduce long-term accumulation of the polymers in the human body, while retaining the improved antimicrobial activity and lower toxicity in comparison to the free drug[15, 102]. However, the production of ethylene glycol upon hydrolytic degradation remained a safety concern for these PPE systems synthesized from common five-membered ring phosphotriester monomers.

4.2 Materials and methods

4.2.1 Materials

Dichloromethane (DCM) and tetrahydrofuran (THF) were purified by a solvent purification system (J. C. Meyer Solvent Systems, Inc., Laguna Beach, CA). 1,5,7-Triazabicyclo[4.4.0]dec-5-ene (TBD) was dried over CaH_2 in THF, concentrated under vacuum

and stored in a glovebox under Ar atmosphere. Methoxy poly(ethylene glycol)$_{45}$ (mPEG$_{45}$) was purchased from RAPP POLYMERE (Tuebingen, Germany). All other chemicals and reagents were used as received from Sigma-Aldrich, Co. (St. Louis, MO) unless otherwise noted. Slide-A-Lyzer dialysis cassettes (10 kDa MWCO) were purchased from Pierce Biotech. (Rockford, IL). Nanopure water (18 MΩ·cm) was acquired from a Milli-Q water filtration system, Millipore Corp. (Bedford, MA). RAW 264.7 mouse macrophage, Dulbecco's Modified Eagle's Medium (DMEM) were obtained from the American Type Culture Collection (Manassas, VA). Media additives (fetal bovine serum, penicillin/streptomycin) were obtained from Sigma-Aldrich (St. Louis, MO). Cell culture 96-well round bottom plates were purchased from Corning Costar Co. (Corning, NY).

4.2.2 Instrumentation

^{1}H NMR, ^{31}P NMR and ^{13}C NMR spectra were acquired on a Varian Inova 500 spectrometer interfaced to a UNIX computer using VnmrJ software. Chemical shifts in the ^{1}H NMR and ^{13}C NMR spectra were referenced to the residual solvent resonance signals, while those in the ^{31}P NMR spectra were referenced to an external standard, 85% H_3PO_4 in D_2O. Fourier-transform infrared spectroscopy (FT-IR) spectra were recorded on an IR Prestige 21 system (Shimadzu Corp., Japan), equipped with an attenuated total reflectance (ATR) accessory, and analyzed using IRsolution v. 1.40 software.

Size exclusion chromatography (SEC) eluting with THF was conducted on a Waters Chromatography, Inc. (Milford, MA) system equipped with an isocratic pump (model 1515), a differential refractometer (model 2414), and a four-column set, including a PLgel™ 5 μm guard column (50 × 7.5 mm), a PLgel™ 5 μm Mixed C column (300 × 7.5 mm, Agilent Technologies)

and two Styragel® columns (500 Å and 104 Å, 300 × 7.5 mm, Waters Chromatography, Inc.). The system was equilibrated at 40 °C with the flow rate set to 1.0 mL/min. Data collection and analysis were performed with Breeze software (Waters Chromatography, Inc., Milford, MA). Molecular weights were determined relative to polystyrene standards (300-467,000 Da) purchased from Polymer Laboratories, Inc. (Amherst, MA). Polymer solutions were prepared at a concentration of *ca.* 3 mg/mL with 0.05 vol% toluene added as a flow marker, and an injection volume of 200 μL was used.

Thermogravimetric analysis (TGA) was performed under Ar atmosphere using a Mettler-Toledo model TGA/DSC 1 with a heating rate of 10 °C/min. Glass transition temperatures (T_g) were measured by differential scanning calorimetry (DSC) on a Mettler-Toledo DSC822® (Mettler-Toledo, Inc., Columbus, OH) under $N_{2(g)}$. DSC measurements were performed with a heating rate of 10 °C/min and analyzed using Mettler-Toledo Star^e v. 10.00 software. The T_g was taken as the midpoint of the inflection tangent of the second heating scan.

Inductively coupled plasma-mass spectrometry (ICP-MS) was performed on a PerkinElmer SCIEX ICP mass spectrometer ELAN DRC II, equipped with a high-speed quadrupole, dynamic reaction cell (DRC) and axial field technology (AFT) to eliminate polyatomic interference, using 1% HNO_3 as the matrix and rhodium as the internal standard.

Transmission electron microscopy (TEM) images were collected on a JEOL 1200EX operated at 100 kV, and micrographs were recorded using a SIA-15C CCD camera. High-resolution scanning transmission electron microscopy (STEM) and elemental mapping were conducted on a FEI Tecnai G^2 F20 FE-TEM coupled with energy-dispersive X-rays (EDX), operating at a voltage of 200 kV and equipped with a Gatan CCD camera. Samples for TEM were prepared as follows: 10 μL of a sample solution in MOPS buffer was deposited onto a

carbon coated copper grid, and after 1 min, excess solution was quickly wicked away by a piece of filter paper. Samples of the silver-loaded nanoparticles were imaged with no staining. And the sample of empty nanoparticles was negatively stained with a 1 wt% phosphotungstic acid (PTA) aqueous solution (10 µL). After 30 s, excess staining solution was quickly wicked away by a piece of filter paper. The samples were then left to dry under ambient conditions overnight.

Atomic force microscopy (AFM) was performed using a Multimode 8 system (Bruker) in PeakForce® tapping mode using a ScanAsyst-Air Silicon Nitride probe ($k = 0.4$ N/m, $f_0 = 70$ kHz, Bruker). AFM images were processed with Nanoscope Analysis 8.15 software (Bruker). Samples were prepared by deposition of a solution of nanoparticles in MOPS buffer (50 µL) onto freshly cleaved mica substrates. After 1 min, excess solution was wicked away by a piece of filter paper, and the mica surface was allowed to dry in air.

Dynamic light scattering (DLS) measurements were conducted using a Delsa Nano C instrument from Beckman Coulter, Inc. (Fullerton, CA) equipped with a laser diode operating at 633 nm. Scattered light from 0.5 mL samples in a disposable polystyrene cell (0.9 mL capacity) was detected at 165° and averaged over 70 accumulations. The photomultiplier aperture and attenuator were adjusted automatically to obtain a photon count rate of *ca.* 10 kcps. The particle size distribution and distribution averages (*i.e.*, the intensity-, volume-, and number-average hydrodynamic diameters) were calculated using CONTIN particle size distribution analysis routines in Delsa Nano 2.31 software. All measurements were repeated 10 times.

Electrospray ionization mass spectrometry (ESI-MS) experiments were performed using a Thermo Scientific LCQ-DECA instrument. The sample was directly infused at a flow rate of 6 µL/min. The spray voltage was set to -4.5 kV, and the sheath gas and auxiliary gas flow rates

were set to 50 and 10 arbitrary units, respectively. The transfer capillary temperature was held at 250 °C. Xcalibur 2.0 software was used for data acquisition and processing.

All experiments were performed according to institutional guidelines provided by Texas A&M's Environmental Health and Safety committee. Experiments involving mouse derived cell lines (RAW 264.7) were performed according to guidelines provided by Texas A&M's Institutional Biosafety Committee for biosafety level 1 organisms (Protocol Approval Number IBC2014-075).

4.2.3 Experimental procedures

Synthesis of 2-ethoxy-4-vinyl-1,3,2-dioxaphospholane-2-oxide (E4VP). To a solution of triethylamine (18.7 mL, 13.6 g, 0.135 mol) in 200 mL of anhydrous THF at 0 °C, a solution of ethyl dichlorophosphate (9.9943 g, 0.061337 mol) in 20 mL of anhydrous THF, and a solution of 3,4-dihydroxy-1-butene (5.4146 g, 0.061453 mol) in 20 mL of anhydrous THF were dropwise added. The reaction mixture was allowed to stir for 12 h. After the complete conversion of ethyl dichlorophosphate as confirmed by ^{31}P NMR, the reaction mixture was filtered and the filtrate was concentrated. The concentrated filtrate was purified by vacuum distillation to afford the pure product as a colorless liquid (5.9 g, 59.7 % yield). ^{1}H NMR (500 MHz, $CDCl_3$, ppm): δ 1.23 (m, 3H, $POCH_2CH_3$), 3.95-4.16, 4.35-4.53 (m, 2H, OCH_2CHO), 4.16-4.30 (m, 2H, $POCH_2CH_3$), 4.91-5.10 (m, 1H, OCH_2CHO), 5.38-5.59 (m, 2H, $CHCH_2$), 5.79-6.00 (m, H, $CHCH_2$); ^{13}C NMR (126 MHz, $CDCl_3$, ppm): δ 16.21, 65.17, 70.13, 78.68, 120.83, 132.34; ^{31}P NMR (202 MHz, $CDCl_3$, ppm): δ 16.32, 16.44. +ESI MS: calculated $[M+H]^+$ for $C_6H_{11}O_4P$: 179.04, found: 179.04.

One-pot synthesis of PEG_{45}-*b*-$PE4VP_{49}$-$PLLA_{20}$ (polymer 1). The polymerization was carried out using standard glovebox and Schlenk line techniques. The $mPEG_{45}$ and L-lactide were dried under vacuum over P_2O_5 for 3 days before being transferred to a glovebox for storage under an inert atmosphere. E4VP monomer was freshly prepared on the same day of polymerization. Stock solutions were prepared in a glovebox under Ar atmosphere, while the ROP was conducted in an -15 °C sodium chloride bath in a fume hood. To a solution of E4VP (1002.3 mg, 5.6294 mmol), and $mPEG_{45}$ (224.7 mg, 0.1124 mmol) in 2.0 mL of DCM at -15 °C, was added the organocatalyst TBD (15.6 mg, 0.112 mmol) in DCM (0.1 mL) under Ar atmosphere. After stirring for 30 min, additional DCM (3.0 mL) was added to dilute the reaction mixture. An aliquot of the reaction mixture was taken out and quenched by addition of acetic acid in DCM, which was characterized by ^{31}P NMR to determine the monomer conversion to be *ca*. 99%. The solution of L-lactide (323.6 mg, 2.245 mmol) in DCM (0.3 mL) was then added. After stirring for 5 min, the reaction vial was opened to air and quenched by addition of Amberlyst 15 H-form resin. The monomer conversion of L-lactide was determined to be *ca*. 100% by analyzing an aliquot of the crude reaction mixture with ^1H NMR. The polymer was purified by precipitation from DCM into a mixture of pentane and diethyl ether (v/v =1:1, 3 ×) and dried under vacuum to afford the product as a white solid (1.30 g, yield 84.2%). ^1H NMR (500 MHz, $CDCl_3$, ppm): δ 1.30-1.41 (br, $POCH_2CH_3$), 1.57-1.65 (br, $C(O)CHCH_3$), 3.40-3.42 (s, OCH_3), 3.65-3.74 (br, $CH_2OCH_2CH_2OCH_2$), 4.04-4.26 (br, $POCH_2CH_3$, OCH_2CHO), 4.90-5.10 (br, OCH_2CHO), 5.14-5.24 (br, $C(O)CHO$) 5.33-5.58 (br, $CH=CH_2$), 5.79-5.98 (br, $CH=CH_2$). ^{31}P NMR (126 MHz, $CDCl_3$, ppm): δ -4.0-0.0 (br). SEC (THF): M_n = 17.8 kDa, $Đ$ = 1.05

Post-polymerization modification of polymer 1 with 3-mercaptopropionic acid *via* thiol-ene reaction to afford polymer 2. PEG_{45}-*b*-$PE4VP_{49}$-*b*-$PLLA_{20}$ (171.3 mg, 0.0126 mmol), 3-mercaptopropionic acid (167.2 mg, 1.473 mmol), and 2,2-dimethoxy-2-phenylacetophenone (DMPA, 47.2 mg, 0.184 mmol) were dissolved in anhydrous DMAc (8 mL), deoxygenated under $N_{2(g)}$ for 30 min, and irradiated under UV light (365 nm) for 2 h. The product was purified by precipitation to remove the excess thiol and photoinitiator, followed by drying under vacuum to afford a viscous liquid (205.2 mg, 95% yield). ^{1}H NMR (500 MHz, DMSO-d_6, ppm): δ 1.35-1.46 (br, $POCH_2CH_3$), 1.95-2.15 (br, $C(O)CHCH_3$, $POCHCH_2CH_2$), 2.55-2.90 (br, $POCHCH_2CH_2$, $POCHCH_2CH_2SCH_2$, $POCHCH_2CH_2SCH_2CH_2$), 3.38-3.39 (s, OCH_3), 3.65-3.68 (br, $CH_2OCH_2CH_2OCH_2$), 4.13-4.42 (br, $POCH_2CH_3$, OCH_2CHO, OCH_2CH), 4.70-4.85 (br, C(O)CHO). ^{31}P NMR (126 MHz, DMSO-d_6, ppm): δ -4.0-0.0 (br). Yield: 91.7 %.

Cytotoxicity assays of polymer 2. RAW 264.7 mouse macrophages (2×10^4 cells/well) were plated in a 96-well plate in Dulbecco's Modified Eagle's Medium (DMEM) (10% fetal bovine serum and 1% penicillin/streptomycin). Cells were incubated at 37 °C in a humidified atmosphere containing 5% CO_2 for 24 h. Culture medium was replaced with a fresh medium prior to the addition of 120 µL serial dilutions of the polymer solutions (final concentrations ranging from 1.5-3000 µg/mL). The stock solution of the polymer was prepared in PBS. The cells were incubated with the polymer solutions for 72 h and then the medium was replaced with 100 µL of fresh medium prior to the addition of 20 µL MTS combined reagent to each well (Cell Titer 96® Aqueous Non-Radioactive Cell Proliferation Assay, Promega Co., Madison, WI). The cells were incubated with the reagent for 2 h at 37 °C in a humidified atmosphere containing 5% CO_2 protected from light. Absorbance was measured at 490 nm using SpectraMax M5 (Molecular Devices Co., Sunnyvale, CA). The cell viability was

calculated based on the relative absorbance to the control-untreated cells. The 0% and 100% cell viabilities were considered as the control medium (no cells) and cells with no treatment, respectively. The calculations of the IC_{50} values were performed using GraphPad Prism four-parameter fit (GraphPad Software, Inc., La Jolla, CA).

Synthesis of the Janus nanoparticles under UV irradiation. Into a 5 mL vial charged with a stir bar, a solution of polymer 2 (PEG-b-PE4VP-b-PLLA, 1.0 mg/mL) and AgOAc (0.17 mg/mL, 10 wt% of Ag relative to polymer 2) in MOPS buffer (pH = 7.4, 1 mL) was added and allowed to stir for 20 min. The solution was then irradiated under UV (365 nm, 500 μJ/cm^2) for 2 min, 4 min, 6 min, or 10 min, respectively, while stirring. The crude mixtures were characterized by TEM to investigate the reaction progress and product morphologies. Well-defined Janus nanoparticles were obtained as the product after 6 min UV irradiation, and the silver loading amount and efficiency was determined by ICP-MS. The product was then washed by MOPS buffer (pH = 7.4) thoroughly using centrifugal filters (N > 3) to remove the free silver ions for further studies.

Release of silver from the Janus nanoparticles. Typically, 3 mL of the Janus nanoparticle was transferred into a presoaked dialysis cassette (Slide-A-Lyzer, 10 kDa MWCO, Pierce Biotechnology, Rockford IL), which was allowed to stir in 4000 mL nanopure water at 37 °C. Aliquots (0.1 mL) of the nanoparticle solution were taken at pre-determined times and analyzed by ICP-MS. The release profiles of the silver-loaded micelles were obtained by monitoring the concentration decrease of silver in the cassettes over time. The release study was conducted in triplicate. A solution of silver acetate in MOPS buffer (pH = 7.4) was tested in the same manner as a control.

4.3 Results and Discussion

In this chapter, an amphiphilic triblock polymer was designed and synthesized based on a novel phosphotriester monomer, 2-ethoxy-4-vinyl-1,3,2-dioxaphospholane-2-oxide (E4VP), which was capable of avoiding the potential drawback of the degradation product. Silver-loaded Janus nanoparticles was then built based on the polymer with a well-defined morphology and optimized drug release profile, where the chemistry is facile, rapid and conveniently-controlled.

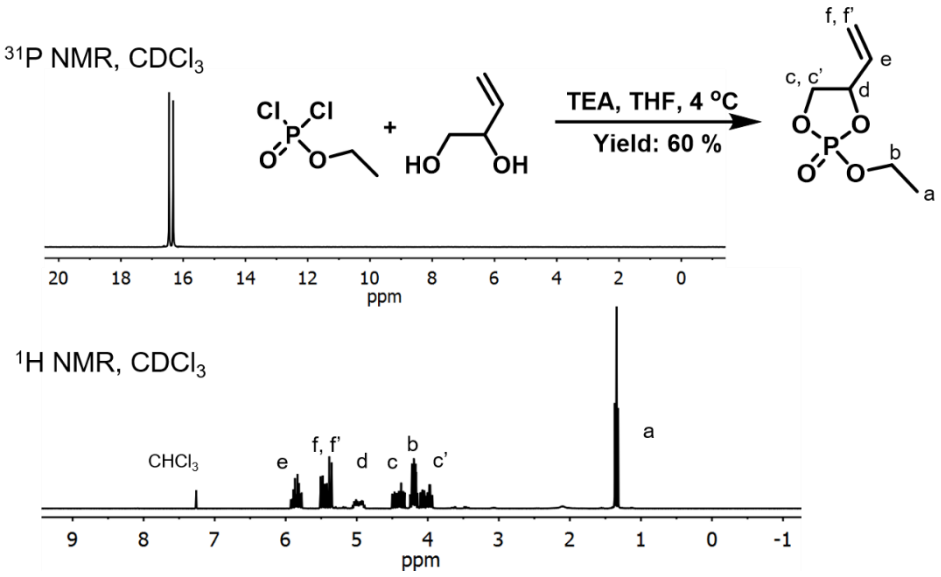

Figure IV.1. Synthesis of E4VP, and characterization by ^{31}P and ^{1}H NMR spectroscopy.

The functional cyclic phosphotriester monomer, E4VP, was designed with a vinyl group attached to the five-membered ring, which was synthesized by annulation of 3,4-dihydroxybutene with ethyl dichlorophosphate in the presence of triethylamine in tetrahydrofuran (THF) at 4 °C (Figure IV.1). The product was purified by distillation under reduced pressure to afford E4VP as a colorless liquid. The monomer was characterized by a

combination of analytical techniques including ^{1}H and ^{31}P NMR (Figure IV.1). Similar to reported cyclic phospholane structures, two resonances at 16.44 and 16.32 ppm were observed in the ^{31}P NMR spectrum of E4VP, attributed to geometric isomers arising from the 2-position ethoxy and 4-position vinyl groups.

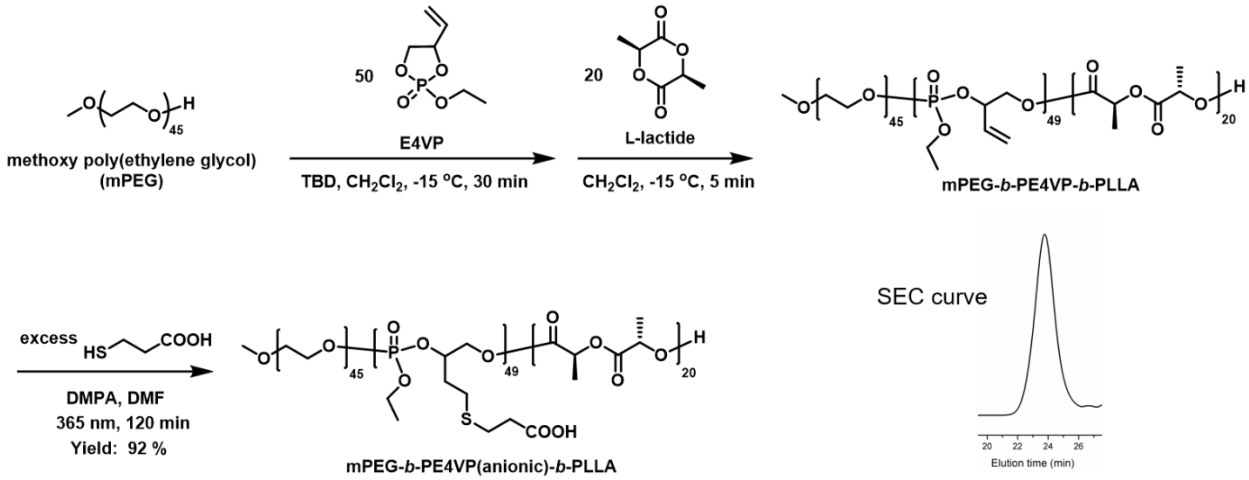

Figure IV.2. Synthesis of polymer 1, $mPEG_{45}$-*b*-$PE4VP_{49}$-*b*-$PLLA_{20}$, followed by post-polymerization modification *via* a thiol-ene click reaction with 3-mercaptopropionic acid to prepare the anionic polymer 2, $mPEG_{45}$-*b*-$PE4VP(anionic)_{49}$-*b*-$PLLA_{20}$. Inset: SEC trace of polymer 1 in THF.

The functional degradable triblock polymer 1, methoxy poly(ethylene glycol)-*block*-poly(2-ethoxy-4-vinyl-1,3,2-dioxaphospholane-2-oxide)-*block*-poly(L-lactide) ($mPEG_{45}$-*b*-$PE4VP_{49}$-*b*-$PLLA_{20}$) was then synthesized by a rapid organocatalyzed one-pot sequential ring-opening polymerization (ROP) of E4VP and L-lactide at -15 °C in dichloromethane (DCM) with $mPEG_{45}$ as the macroinitiator and 1,5,7 triazabicyclo[4.4.0]-dec-5-ene (TBD) as the organocatalyst (Figure IV.2). The feed ratio of monomers to the initiator [E4VP] : [L-lactide] :

[mPEG] was set to be 50 : 20 : 1 to provide sufficient hydrophobicity and versatile functionality. The E4VP monomer was first polymerized at a relatively high concentration in DCM. After nearly complete conversion (*ca*. 99%, monitored by ^{31}P NMR) of E4VP in 30 min, additional DCM was added to dilute the reaction mixture, followed by the addition of L-lactide for the chain extension. The reaction was quenched by addition of Amberlyst 15 H-form resin after 5 min, with the conversion of L-lactide to be *ca*. 100%, determined by ^{1}H NMR. SEC indicated monomodal molar mass distribution and low dispersity ($Đ$ = 1.05), demonstrating the well-defined structure of the triblock polymer. The number-average molar mass (M_n) of the polymer and degree of polymerization (DP_n) of each monomer were calculated from the ^{1}H NMR spectra (Figure IV.3) acquired after isolation of the polymer by precipitation, by comparing the integration of the CH_2CH_2O proton resonances (3.63 ppm) from the macroinitiator with the intensities of the resonances of protons in the methyl groups at and chemical shift in the PE4VP and PLLA segments, respectively.

The anionic polymer **2**, mPEG$_{45}$-*b*-PE4VP(anionic)$_{49}$-*b*-PLLA$_{20}$, was prepared by post-polymerization modification of **1** *via* a photoinitiated thiol-ene click reaction with an excess of 3-mercaptopropionic acid (10 equivalents relative to the alkene groups) (Figure IV.2). The polymer was purified by precipitation and dried under vacuum to afford a viscous liquid. The disappearance of the alkene proton resonances at 6.0 - 5.3 ppm in the ^{1}H NMR spectrum indicated the consumption of the alkene groups (Figure IV.4). T_g of polymer 2 was observed at – 28 °C in the DSC thermogram, suggesting the flexibility of the polymer chain.

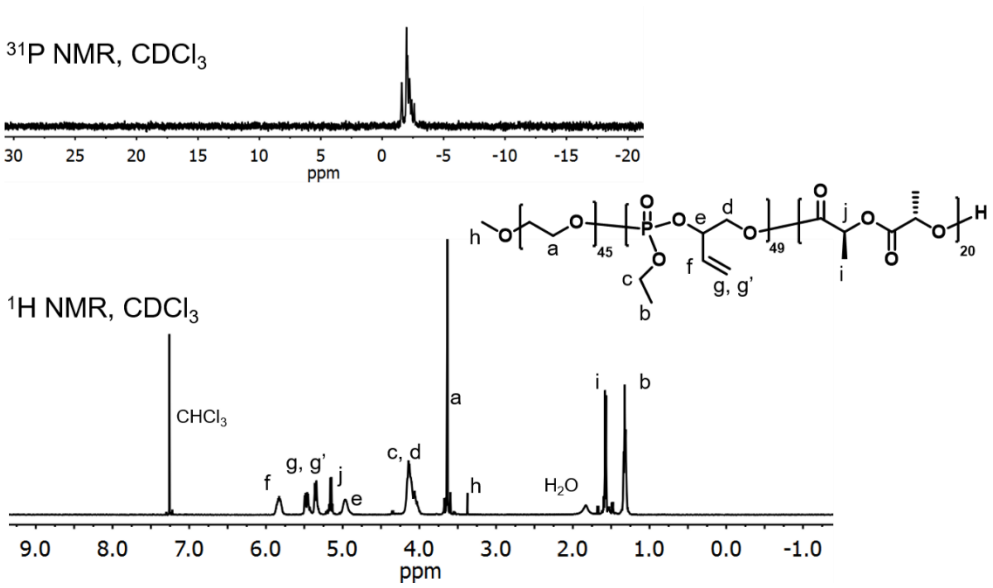

Figure IV.3. Characterization of polymer 1 by ^{31}P and ^{1}H NMR spectroscopy.

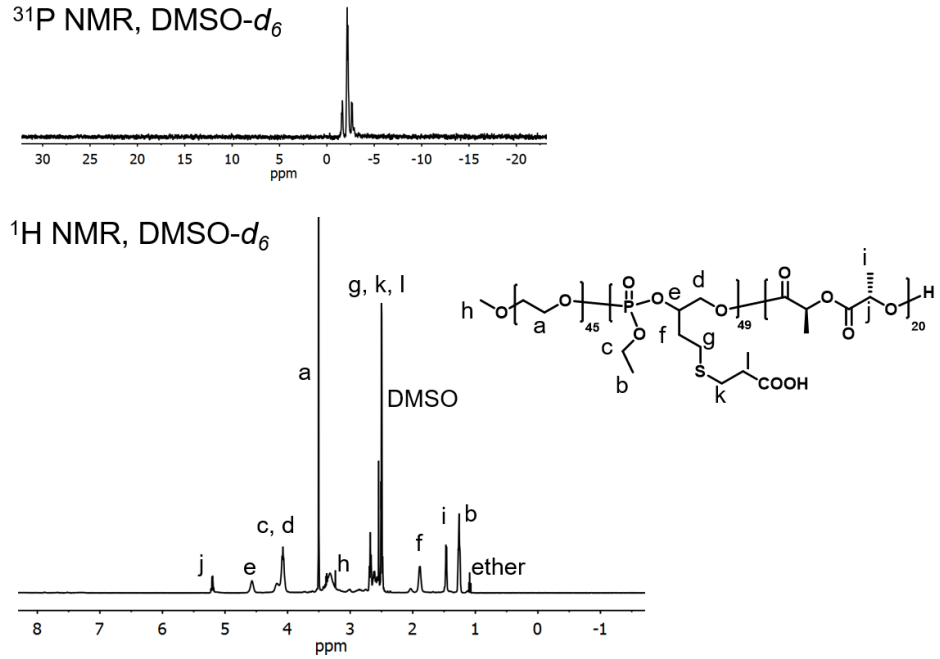

Figure IV.4. Characterization of polymer 2 by ^{31}P and ^{1}H NMR spectroscopy.

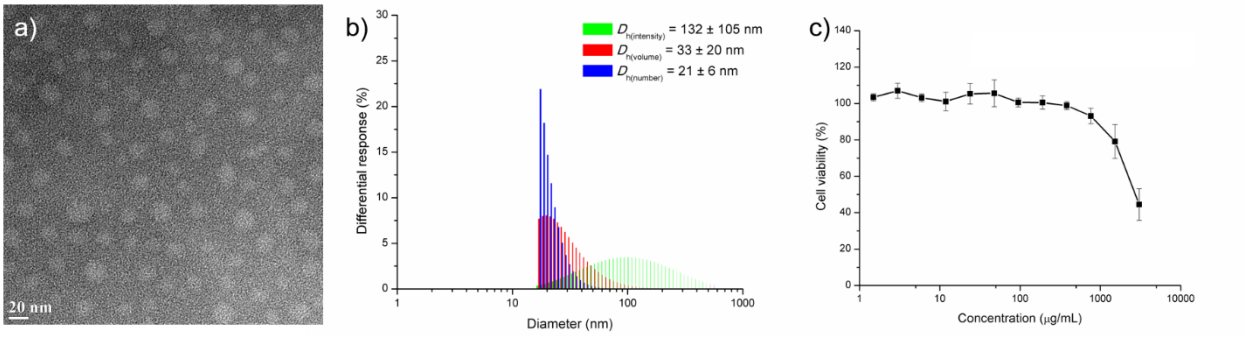

Figure IV.5. Characterization of the anionic PPE-based nanoparticles. a) The TEM image of the nanoparticles negatively stained by 1 wt% phosphotungstic acid (PTA) aqueous solution. b) Number-, volume- and intensity-average hydrodynamic diameters measured by DLS. c) Cytotoxicity of the nanoparticles in the RAW 264.7 cell line. Cell viabilities are reported as an average of three measurements, and error bars represent standard deviation.

Self-assembly of polymer **2** was investigated by directly dissolving polymer **2** into the MOPS buffer (pH = 7.4) to form anionic nanoparticles. As depicted in Figure IV.5a, transmission electron microscopy (TEM) images displayed circular structures of the nanoparticles with an average diameter (D_{av}) to be 17 ± 3 nm. Dynamic light scattering (DLS) showed a unimodal size distribution of the nanoparticles, with the number-average hydrodynamic diameter to be 21 ± 6 nm (Figure IV.5b). The anionic nanoparticles were then tested for their toxicity in the cancer cell line, RAW 264.7 mouse macrophage, at concentrations ranging from 1.5 to 3000 μg/mL. Similar to the previously reported anionic PPEs[19], the nanoparticles showed minimal cytotoxicity at concentrations below 750 μg/mL, while reduced toxicity at 3000 μg/mL was observed, confirming their biocompatibility for biomedical use (Figure IV.5c).

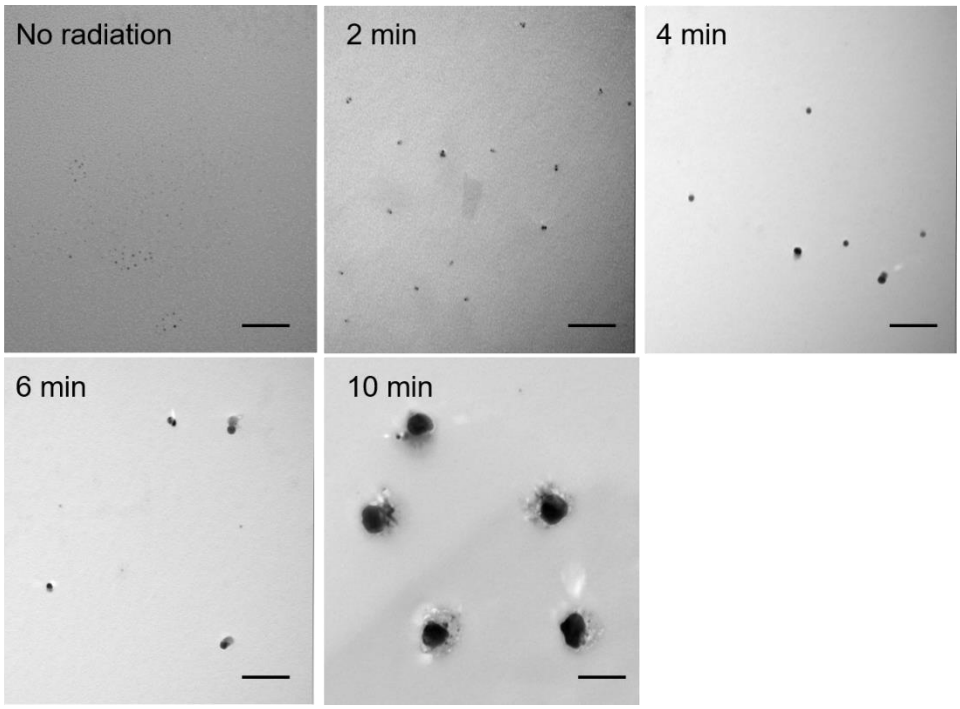

Figure IV.6. Characterization of the mixture of polymer 2 and silver acetate solutions in the MOPS buffer (pH = 7.4) after UV irradiation for different times by TEM. Scale bar: 100 nm.

Silver loading was subsequently conducted by directly mixing solutions of the anionic PPE-based nanoparticles and silver acetate (10 wt% Ag relative to the polymer). The TEM image of the crude mixture (no staining) indicated successful loading of silver into the nanoparticles with circular nanostructures (Figure IV.6). The mixtures were allowed to stir under UV irradiation (365 nm, 500 μJ/cm^2) for 2 min, 4 min, 6 min, and 10 min, respectively, which were then characterized by TEM (Figure IV.6). The TEM images revealed the formation of snowman-like Janus nanoparticles over time under the UV irradiation, until the appearance of large aggregates upon overexposure.

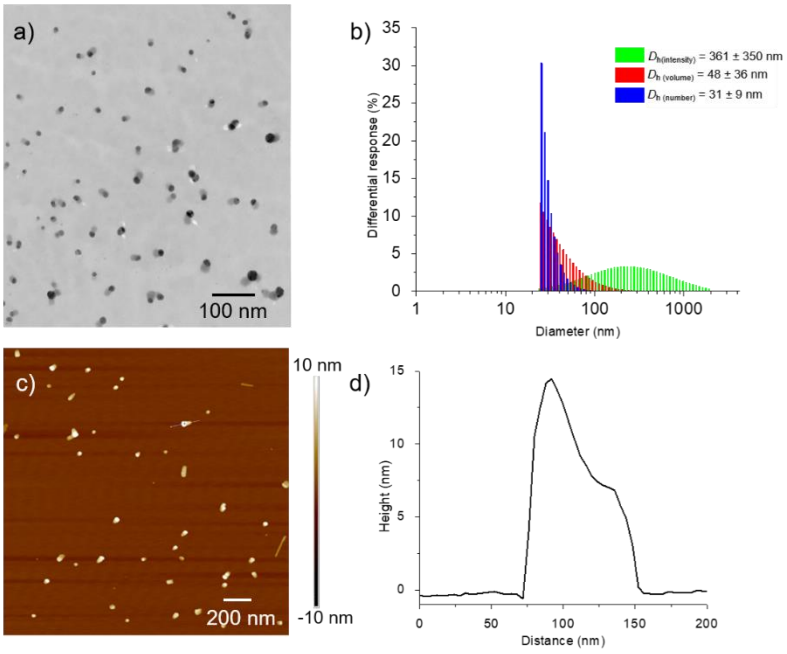

Figure IV.7. Characterization of the silver-loaded PPE-based Janus nanoparticles. a) The TEM image of the nanoparticles with no staining. b) Number-, volume- and intensity-average hydrodynamic diameters of the nanoparticles measured by DLS. c) The AFM image and d) AFM height of the nanoparticles.

As shown in Figure IV.7a, the Janus nanoparticles consisted of two circular parts, showing the similar D_{av} to be *ca*. 14 nm, with different contrast under TEM. It was inferred that the higher contrast part was the metallic silver nanoparticle reduced upon the UV irradiation, while the lower contrast part was the PPE-based micelle loaded with silver cations/cluster. The interactions between the PE4VP segment functionalities and the silver species allowed for partial reduction of the silver cations with a proper amount of UV irradiation. Due to the flexibility of the PPE-based polymer chains, it is hypothesized that the nucleation centers of the reduced silver were capable of joining each other and growing to a single spherical nanoparticle, to form the Janus nanostructure as a relatively stable state. The proposed Janus nanostructure was further confirmed by AFM images, which revealed average heights of the two parts to be 14 ± 4 nm and

6 ± 2 nm, respectively (Figure IV.7c, d). Compared to the empty micelles, DLS results indicated an increase of the number-average hydrodynamic diameter to be 31 ± 9 nm for the Janus nanoparticles (Figure IV.7b). In comparison, the solution of silver acetate in the MOPS buffer without addition of the polymer did not generate the well-defined snowman-like Janus nanoparticles (Figure IV.8), but showed a small amount of precipitates on the stir bar under similar conditions.

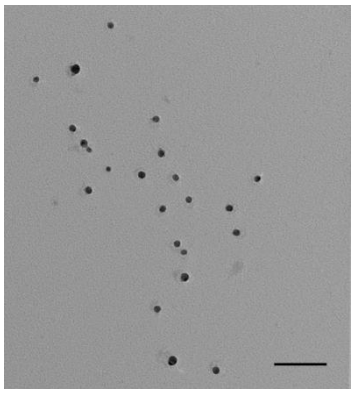

Figure IV.8. Characterization of the solution of silver acetate in the MOPS buffer (pH = 7.4) after irradiation under UV (365 nm, 500 μJ/cm^2) for 6 min by TEM. Scale bar: 100 nm.

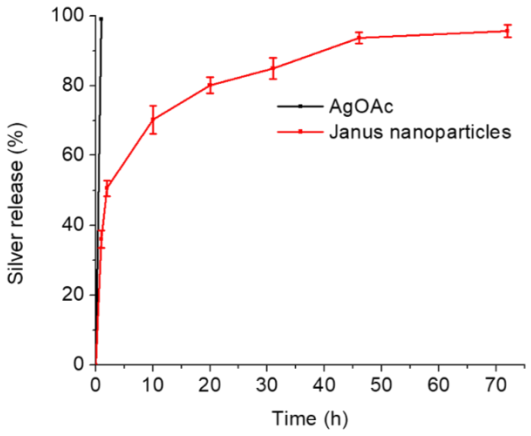

Figure IV.9. Drug release from the silver-loaded PPE-based Janus nanoparticles in nanopure water, with the solution of silver acetate as a control, measured in triplicate. Error bars indicate standard deviation.

The release of silver from the Janus nanoparticles was then evaluated, showing the improved drug release profile, with the solution of silver acetate utilized as a control. The solutions were transferred into presoaked dialysis cassettes (MWCO 10 kDa) and dialyzed against nanopure water. The drug release profiles were obtained by monitoring the decrease of silver concentrations in the cassettes as a function of time by inductively coupled plasma mass spectrometry (ICP-MS). As depicted in Figure IV.9, an initial burst release (*ca*. 50%) of silver from the PPE-based nanoparticles was observed within 2 h, followed by much more controlled and sustained release of the remaining silver over *ca*. 2 d. Such release profiles are anticipated to be quite beneficial for drug delivery, which also evidence our proposed mechanism for the Janus nanostructure. In comparison, complete release of silver from the silver acetate control solution was observed within 1 h.

4.4 Conclusions

A facile, rapid and conveniently-controlled approach to synthesize silver-loaded PPE-based Janus nanoparticles is reported. The novel functional phosphotriester monomer, E4VP, was designed and synthesized through a one-step annulation reaction to address the safety concern of previous PPE systems on their hydrolytic degradation product, ethylene glycol. The triblock polymer, mPEG-*b*-PE4VP-*b*-PLLA, was then afforded by a one-pot sequential polymerization of E4VP and L-lactide with mPEG as the initiator, followed by post-polymerization modification *via* a thiol-ene click reaction to introduce carboxylic acid functionalities. A mixture of the polymer and silver acetate solutions was irradiated under UV to achieve partial reduction of the silver cations. Interactions between the polymer and silver species allowed for the formation of well-defined Janus nanoparticles, as observed by TEM and

AFM, with the reaction progress controllable by the irradiation time. Within 2 h dialysis against nanopure water, *ca*. 50% of silver was released from the Janus nanoparticles, with the remaining silver released in a much slower manner over 40 h, which could be beneficial in treatment of bacterial infections. Based on the facile and controllable synthetic approach, the optimal drug release profile demonstrates the promise of these well-defined silver-loaded PPE-based Janus nanostructures as antimicrobial agents for clinical use.

CHAPTER V

CONCLUSIONS AND FUTURE WORK

5.1 Conclusions

This dissertation is focused on the rational design and synthesis of biocompatible polymers, based on polyphosphoesters (PPEs) and poly(glucose carbonate)s (PGCs), to formulate advanced nanostructures as molecular nanoprobes and nanomedicines. Towards the applications, two parts were highlighted: (1) preparation of degradable, biocompatible zwitterionic polymeric coating materials for metal nanoprobes, as discussed in Chapter II, and (2) development of degradable and biocompatible nanocarriers for anticancer therapeutics or antimicrobials, as described in Chapters III and IV.

In Chapter II, a zwitterionic PPE was designed and synthesized to achieve a promising alternative to PEG as an AuNP coating material, with hydrolytic degradability, favorable immunotoxicity and antifouling properties. PPE with a monomodal molar mass distribution was prepared, followed by functionalization of the alkynes in the side chains of the polymer with L-cysteine *via* thiol-yne click reactions to yield the zPPEs. The installation of large amounts of zwitterions in the side chains yielded highly hydrophilic polymers, which were coated successfully onto citrate-coated AuNPs through multivalent interactions between the thioether, carboxylic acid/carboxylate, and amine/ammonium groups of the polymer side chains and the Au surface of the NPs. Morphological analysis of the zPPE-coated and PEG-coated AuNPs revealed similarly sized cores of *ca.* 4 nm, and increased hydrodynamic diameters of the polymer-coated AuNPs relative to the citrate-coated AuNPs. Degradation studies of the zPPE-coated AuNPs were conducted, indicating hydrolysis of side chain and backbone units proceeded to an

extent of *ca.* 75% over 2 d in nanopure water (pH 5-6), together with broadening and red-shifting of the surface plasmon resonance (SPR) peak over time. Negligible immunotoxicity of the coated NPs was confirmed, as demonstrated by incubating RAW 264.7 mouse macrophages with the NPs, followed by measuring the levels of twenty-three cytokines relative to those in cells incubated without NPs. The optimal antifouling performance of zPPE-coated AuNPs was demonstrated by cytokine adsorption studies. The biocompatibility and advanced antifouling properties of the zPPE-coated AuNPs indicated the promise of zPPE as a novel coating material for metal nanostructures.

In Chapter III, degradable, functional nanocarriers were designed based on two PGC-based block polymers and one dimeric PTX (diPTX) pro-drug, where the chemistry of each component was defined to fulfill important tasks. The well-defined diblock terpolymer was synthesized by rapid ROP of glucose-derived monomers with PEG as the macroinitiator, which showed good biocompatibility, degradability and versatile functionality. Cationic moieties were introduced by thiol-yne click modification of the PGC segment, to achieve enhanced tumor penetration ability, while undesirable characteristics of cationic polymers was mitigated by the PEG shell. The diPTX pro-drug was designed with a disulfide linkage to allow for redox-triggered release in cancer cells with high GSH concentration, where the negatively-charged GSH can readily access the encapsulated diPTX due to the presence of cationic charges in the nanostructure. Nanocarriers was constructed by co-assembly of the amphiphilic cationic PGC and an analogous NIR-labeled non-ionic polymer, which showed controlled and sustained *in vitro* PTX drug release in the presence of reducing agents. The biocompatibility and significant cancer-killing selectivity of the diPTX-loaded cationic PGC micelles were confirmed by cytotoxicity assays. Improved tumor penetration ability and anticancer efficacy of

diPTX@CPGC relative to Taxol-mimicking formulations were further demonstrated by studies in SJSA-1 MCTSs. The diPTX@CPGC further exhibited its significant anticancer efficacy as inhaled chemotherapeutics in an orthotopic mouse model of human OS, with free diPTX and PBS as control groups. Throughout the study, the weights of the mice in the treatment and control groups did not change significantly, indicating the tolerance of the diPTX pro-drug and the PGC micelles. The *ex vivo* studies showed appreciable distribution of the micelles throughout various structures of the lung, which also confirmed a reduction of tumor growth after treatment with diPTX@CPGC. The anticancer selectivity of the formulation both *in vitro* and *in vivo* demonstrates its potential for treatment of OS lung metastases.

In Chapter IV, well-defined silver-loaded PPE-based Janus nanoparticles were developed from a facile, rapid and conveniently-controlled approach. A triblock polymer was first designed and synthesized, based on a novel functional phosphotriester monomer (E4VP), to address the safety concern of previous PPE systems on their hydrolytic degradation product, ethylene glycol. By a one-pot sequential polymerization of and L-lactide with mPEG as the initiator, the polymer was afforded, followed by post-polymerization modification *via* a thiol-ene click reaction to introduce carboxylic acid functionalities. Solutions of the polymer and silver acetate were allowed to mix and stir under UV irradiation to achieve partial reduction of the silver cations. Due to the interactions between the polymer and silver species, well-defined Janus nanoparticles were formed, as observed by TEM and AFM, with the reaction progress controllable by the irradiation time. Release studies were conducted for these Janus nanoparticles, and *ca*. 50% of silver release was observed within 2 h dialysis against nanopure water. The remaining silver was then released in a much slower manner over 40 h, which could be beneficial in treatment of bacterial infections.

5.2 Future Work

Degradable polymers hold great promise for the development of biomedical materials as nanoprobes and nanomedicines, with the advantage to avoid the safety concerns of non-degradable materials after long-term accumulation in the human body. Future work will include a deeper understanding of rational designs and synthetic strategies of these polymeric systems, to achieve optimized performance for the diagnosis and treatment of diseases threatening human health and lives. Moreover, the degradable polymers as well as the synthesis and characterization techniques developed in this work should not be limited to the biomedical field, but will also be explored for other potential applications, such as antifreeze agents, renewable plastics, *etc*., to address global challenges, including environment pollution and fossil resource depletion.

For all the nanoprobe and nanomedicines developed in this work, further studies will include introduction of target ligands *via* post-polymerization modification to improve the efficacy of diagnosis or treatment and reduce the off-target effects on healthy tissues. It is also desirable to load both imaging and therapeutic agents in the same nanoparticle system for theranostic applications. By introducing cationic charges into the nanostructures, nucleic acids could be loaded and delivered for gene therapy. Rational design of the structures of polymers and nanoparticles will be conducted to prepare materials with different responsiveness for better selectivity. Aside from applications in nanotechnology, the functional cyclic phosphotriester or glucose carbonate monomers developed in this work could also be used to prepare degradable

hydrogels, by polymerizations followed by crosslinking, which will be investigated for drug delivery and tissue engineering.

Zwitterionic polymers have been reported as advanced materials as antifreeze agents, which are capable of preventing or modifying the freezing behavior of water. Applications of these additives include the cryopreservation of blood and tissues, reducing corrosions of steel or concrete, and eliminating damage of crops in the agricultural industry. In Chapter II, the degradability and biocompatibility of zwitterionic PPEs have been confirmed as nanoparticle coating. These properties offer the potential of the zwitterionic polyphosphoesters as antifreeze agents for both medical and industrial applications, which will eliminate safety concerns and pollutions from the additives. A series of zwitterionic polymers can be afforded from the PPEs developed in Chapter II and IV. Effects of these zwitterionic PPEs on the freezing behavior of water will be explored, and the degradability and biocompatibility will be evaluated, to prepare antifreeze agents with the optimal antifreeze performance.

Based on the synthetic strategies and analytical techniques developed in Chapter III, sustainable sugar-derived plastics could be obtained from the renewable natural products. Investigation and application of these renewable plastics will help address the global challenge of depletion of fossil resources. By investigating the chemical structure and synthetic routes of the PGCs, it is expected to develop a library of low-cost sugar-derived polymers with degradability and tunable thermal and mechanical properties, which will not only reduce the global dependence on petroleum resources, but also eliminate pollutions to the environment.

REFERENCES

1. Lock, L. L.; Reyes, C. D.; Zhang, P.; Cui, H., Tuning Cellular Uptake of Molecular Probes by Rational Design of Their Assembly into Supramolecular Nanoprobes. *J. Am. Chem. Soc.* **2016**, *138*, 3533-40.

2. Shi, J.; Kantoff, P. W.; Wooster, R.; Farokhzad, O. C., Cancer nanomedicine: Progress, challenges and opportunities. *Nat. Rev. Cancer* **2017**, *17* (1), 20-37.

3. Sun, Q. H.; Zhou, Z. X.; Qiu, N. S.; Shen, Y. Q., Rational design of cancer nanomedicine: Nanoproperty integration and synchronization. *Adv. Mater.* **2017**, *29*, 1606628.

4. Taratula, O.; Kuzmov, A.; Shah, M.; Garbuzenko, O. B.; Minko, T., Nanostructured lipid carriers as multifunctional nanomedicine platform for pulmonary co-delivery of anticancer drugs and siRNA. *J. Control. Release* **2013**, *171*, 349-357.

5. Wicki, A.; Witzigmann, D.; Balasubramanian, V.; Huwyler, J., Nanomedicine in cancer therapy: Challenges, opportunities, and clinical applications. *J. Control. Release* **2015**, *200*, 138-157.

6. Juliano, R., Nanomedicine: Is the wave cresting? *Nat. Rev. Drug Discov.* **2013**, *12*, 171.

7. Elsabahy, M.; Heo, G. S.; Lim, S.-M.; Sun, G.; Wooley, K. L., Polymeric nanostructures for imaging and therapy. *Chem. Rev.* **2015**, *115*, 10967-11011.

8. Pelegri-O'Day, E. M.; Paluck, S. J.; Maynard, H. D., Substituted polyesters by thiol–ene modification: rapid diversification for therapeutic protein stabilization. *J. Am. Chem. Soc.* **2017**, *139*, 1145-1154.

9. Cameron, N.; Deming, T., Peptide-based materials for nanomedicine. *Macromol. Biosci.* **2015**, *15*, 7-8.

10. Schöttler, S.; Becker, G.; Winzen, S.; Steinbach, T.; Mohr, K.; Landfester, K.; Mailänder, V.; Wurm, F. R., Protein adsorption is required for stealth effect of poly(ethylene glycol)- and poly(phosphoester)-coated nanocarriers. *Nat. Nanotechnol.* **2016**, *11*, 372-377.

11. Steinbach, T.; Wurm, F. R., Poly(phosphoester)s: A new platform for degradable polymers. *Angew. Chem. Int. Ed.* **2015**, *54*, 6098-6108.

12. Brannigan, R. P.; Dove, A. P., Synthesis, properties and biomedical applications of hydrolytically degradable materials based on aliphatic polyesters and polycarbonates. *Biomater. Sci.* **2017**, *5*, 9-21.

13. Yim, H.; Park, S. J.; Bae, Y. H.; Na, K., Biodegradable cationic nanoparticles loaded with an anticancer drug for deep penetration of heterogeneous tumours. *Biomaterials* **2013**, *34*, 7674-82.

14. Zhang, F.; Khan, S.; Li, R.; Smolen, J. A.; Zhang, S.; Zhu, G.; Su, L.; Jahnke, A. A.; Elsabahy, M.; Chen, X.; Wooley, K. L., Design and development of multifunctional polyphosphoester-based nanoparticles for ultrahigh paclitaxel dual loading. *Nanoscale* **2017**, *9*, 15773-15777.

15. Zhang, F.; Smolen, J. A.; Zhang, S.; Li, R.; Shah, P. N.; Cho, S.; Wang, H.; Raymond, J. E.; Cannon, C. L.; Wooley, K. L., Degradable polyphosphoester-based silver-loaded nanoparticles as therapeutics for bacterial lung infections. *Nanoscale* **2015**, *7*, 2265-2270.

16. Zhang, F.; Zhang, S.; Pollack, S. F.; Li, R.; Gonzalez, A. M.; Fan, J.; Zou, J.; Leininger, S. E.; Pavía-Sanders, A.; Johnson, R., Improving paclitaxel delivery: *In vitro* and *in vivo* characterization of PEGylated polyphosphoester-based nanocarriers. *J. Am. Chem. Soc.* **2015**, *137*, 2056-2066.

17. Zhang, S.; Li, A.; Zou, J.; Lin, L. Y.; Wooley, K. L., Facile synthesis of clickable, water-soluble, and degradable polyphosphoesters. *ACS Macro Lett.* **2012**, *1*, 328-333.

18. Zhang, S.; Zou, J.; Elsabahy, M.; Karwa, A.; Li, A.; Moore, D. A.; Dorshow, R. B.; Wooley, K. L., Poly(ethylene oxide)-*block*-polyphosphester-based paclitaxel conjugates as a platform for ultra-high paclitaxel-loaded multifunctional nanoparticles. *Chem. Sci.* **2013**, *4*, 2122-2126.

19. Zhang, S.; Zou, J.; Zhang, F.; Elsabahy, M.; Felder, S. E.; Zhu, J.; Pochan, D. J.; Wooley, K. L., Rapid and versatile construction of diverse and functional nanostructures derived from a polyphosphoester-based biomimetic block copolymer system. *J. Am. Chem. Soc.* **2012**, *134*, 18467-74.

20. Su, L.; Khan, S.; Fan, J.; Lin, Y.-N.; Wang, H.; Gustafson, T. P.; Zhang, F.; Wooley, K. L., Functional sugar-based polymers and nanostructures comprised of degradable poly(D-glucose carbonate)s. *Polym. Chem.* **2017**, *8*, 1699-1707.

21. *Critically important antimicrobials for human medicine: Ranking of antimicrobial agents for risk management of antimicrobial resistance due to non-human use*; 9241512229; World Health Organization: 2017.

22. World Health Organization Cancer. http://www.who.int/news-room/fact-sheets/detail/cancer.

23. World Health Organization The top 10 causes of death. http://www.who.int/news-room/fact-sheets/detail/the-top-10-causes-of-death.

24. *Antibiotic resistance threats in the United States, 2013*; US Department of Health Human Services: 2013.

25. Luepke, K. H.; Suda, K. J.; Boucher, H.; Russo, R. L.; Bonney, M. W.; Hunt, T. D.; Mohr III, J. F., Past, present, and future of antibacterial economics: Increasing bacterial resistance, limited antibiotic pipeline, and societal implications. *Pharmacotherapy* **2017**, *37*, 71-84.

26. Bielack, S. S.; Kempf-Bielack, B.; Branscheid, D.; Carrle, D.; Friedel, G.; Helmke, K.; Kevric, M.; Jundt, G.; Kuhne, T.; Maas, R.; Schwarz, R.; Zoubek, A.; Jurgens, H., Second and subsequent recurrences of osteosarcoma: Presentation, treatment, and outcomes of 249 consecutive cooperative osteosarcoma study group patients. *J. Clin. Oncol.* **2009**, *27*, 557-565.

27. Meyers, P. A.; Schwartz, C. L.; Krailo, M. D.; Healey, J. H.; Bernstein, M. L.; Betcher, D.; Ferguson, W. S.; Gebhardt, M. C.; Goorin, A. M.; Harris, M.; Kleinerman, E.; Link, M. P.; Nadel, H.; Nieder, M.; Siegal, G. P.; Weiner, M. A.; Wells, R. J.; Womer, R. B.; Grier, H. E., Osteosarcoma: The addition of muramyl tripeptide to chemotherapy improves overall survival - A report from the Children's Oncology Group. *J. Clin. Oncol.* **2008**, *26*, 633-638.

28. Ottaviani, G.; Jaffe, N., *The Epidemiology of Osteosarcoma*. Springer: Dordrecht, 2009; Vol. 152, p 3-13.

29. Hu, Y.; Mignani, S.; Majoral, J.-P.; Shen, M.; Shi, X., Construction of iron oxide nanoparticle-based hybrid platforms for tumor imaging and therapy. *Chem. Soc. Rev.* **2018**, *47*, 1874-1900.

30. Elzoghby, A. O.; Hemasa, A. L.; Freag, M. S., Hybrid protein-inorganic nanoparticles: From tumor-targeted drug delivery to cancer imaging. *J. Control. Release* **2016**, *243*, 303-322.

31. Palui, G.; Aldeek, F.; Wang, W.; Mattoussi, H., Strategies for interfacing inorganic nanocrystals with biological systems based on polymer-coating. *Chem. Soc. Rev.* **2015**, *44*, 193-227.

32. Wang, W.; Ji, X.; Du, L.; Mattoussi, H., Enhanced colloidal stability of various gold nanostructures using a multicoordinating polymer coating. *J. Phys. Chem. C* **2017**, *121*, 22901-22913.

33. Karakoti, A. S.; Das, S.; Thevuthasan, S.; Seal, S., PEGylated inorganic nanoparticles. *Angew. Chem. Int. Ed.* **2011**, *50*, 1980-1994.

34. Joralemon, M. J.; McRae, S.; Emrick, T., PEGylated polymers for medicine: from conjugation to self-assembled systems. *Chem. Commun.* **2010**, *46*, 1377-1393.

35. Pelaz, B.; del Pino, P.; Maffre, P.; Hartmann, R.; Gallego, M.; Rivera-Fernandez, S.; de la Fuente, J. M.; Nienhaus, G. U.; Parak, W. J., Surface functionalization of nanoparticles with polyethylene glycol: Effects on protein adsorption and cellular uptake. *ACS Nano* **2015**, *9*, 6996-7008.

36. Armstrong, J. K.; Hempel, G.; Koling, S.; Chan, L. S.; Fisher, T.; Meiselman, H. J.; Garratty, G., Antibody against poly(ethylene glycol) adversely affects PEG-asparaginase therapy in acute lymphoblastic leukemia patients. *Cancer* **2007**, *110*, 103-111.

37. Gaberc-Porekar, V.; Zore, I.; Podobnik, B.; Menart, V., Obstacles and pitfalls in the PEGylation of therapeutic proteins. *Curr. Opin. Drug Discov. Devel.* **2008**, *11*, 242.

38. Li, L.; Chen, S.; Jiang, S., Protein interactions with oligo(ethylene glycol) (OEG) self-assembled monolayers: OEG stability, surface packing density and protein adsorption. *J. Biomater. Sci. Polym. Ed.* **2007**, *18*, 1415-1427.

39. Li, B.; Yuan, Z.; Zhang, P.; Sinclair, A.; Jain, P.; Wu, K.; Tsao, C.; Xie, J.; Hung, H. C.; Lin, X.; Bai, T.; Jiang, S., Zwitterionic nanocages overcome the efficacy loss of biologic drugs. *Adv. Mater.* **2018**, 1705728.

40. Liu, Q.; Singha, P.; Handa, H.; Locklin, J., Covalent grafting of antifouling phosphorylcholine-based copolymers with antimicrobial nitric oxide releasing polymers to enhance infection-resistant properties of medical device coatings. *Langmuir* **2017**, *33*, 13105-13113.

41. Chen, X.; Lawrence, J.; Parelkar, S.; Emrick, T., Novel zwitterionic copolymers with dihydrolipoic acid: Synthesis and preparation of nonfouling nanorods. *Macromolecules* **2012**, *46*, 119-127.

42. Zhang, C.; Li, H.-N.; Du, Y.; Ma, M.-Q.; Xu, Z.-K., $CuSO_4/H_2O_2$-triggered polydopamine/poly(sulfobetaine methacrylate) coatings for antifouling membrane surfaces. *Langmuir* **2017**, *33*, 1210-1216.

43. Chen, S.; Li, L.; Zhao, C.; Zheng, J., Surface hydration: Principles and applications toward low-fouling/nonfouling biomaterials. *Polymer* **2010**, *51*, 5283-5293.

44. Elsabahy, M.; Li, A.; Zhang, F.; Sultan, D.; Liu, Y.; Wooley, K. L., Differential immunotoxicities of poly(ethylene glycol)-vs. poly(carboxybetaine)-coated nanoparticles. *J. Control. Release* **2013**, *172*, 641-652.

45. Becker, G.; Ackermann, L.-M.; Schechtel, E.; Klapper, M.; Tremel, W.; Wurm, F. R., Joining two natural motifs: Catechol-containing poly(phosphoester)s. *Biomacromolecules* **2017**, *18*, 767-777.

46. Su, L.; Li, R.; Khan, S.; Clanton, R.; Zhang, F.; Lin, Y.-N.; Song, Y.; Wang, H.; Fan, J.; Hernandez, S., Chemical design of both a glutathione-sensitive dimeric drug guest and a glucose-derived nanocarrier host to achieve enhanced osteosarcoma lung metastatic anticancer selectivity. *J. Am. Chem. Soc.* **2018**, *140*, 1438-1446.

47. Song, Y.; Chen, Y.; Su, L.; Li, R.; Letteri, R. A.; Wooley, K. L., Crystallization-driven assembly of fully degradable, natural product-based poly(L-lactide)-*block*-poly(α-D-glucose carbonate)s in aqueous solution. *Polymer* **2017**, *122*, 270-279.

48. Elsabahy, M.; Wooley, K. L., Data mining as a guide for the construction of cross-linked nanoparticles with low immunotoxicity *via* control of polymer chemistry and supramolecular assembly. *Acc. Chem. Res.* **2015**, *48*, 1620-1630.

49. Elsabahy, M.; Zhang, S.; Zhang, F.; Deng, Z. J.; Lim, Y. H.; Wang, H.; Parsamian, P.; Hammond, P. T.; Wooley, K. L., Surface charges and shell crosslinks each play significant roles in mediating degradation, biofouling, cytotoxicity and immunotoxicity for polyphosphoester-based nanoparticles. *Sci. Rep.* **2013**, *3*, 3313.

50. Her, S.; Jaffray, D. A.; Allen, C., Gold nanoparticles for applications in cancer radiotherapy: Mechanisms and recent advancements. *Adv. Drug Deliv. Rev.* **2017**, *109*, 84-101.

51. Jana, N. R.; Gearheart, L.; Murphy, C. J., Seeding growth for size control of 5−40 nm diameter gold nanoparticles. *Langmuir* **2001**, *17*, 6782-6786.

52. Elsabahy, M.; Wooley, K. L., Reassessment of nanomaterials immunotoxicity. *Nano Today* **2018**, *20*, 10-12.

53. Zhao, Y.; Detering, L.; Sultan, D.; Cooper, M. L.; You, M.; Cho, S.; Meier, S. L.; Luehmann, H.; Sun, G.; Rettig, M.; Dehdashti, F.; Wooley, K. L.; DiPersio, J. F.; Liu, Y., Gold nanoclusters doped with ^{64}Cu for CXCR4 positron emission tomography imaging of breast cancer and metastasis. *ACS Nano* **2016**, *10*, 5959-70.

54. Zhang, S.; Wang, H.; Shen, Y.; Zhang, F.; Seetho, K.; Zou, J.; Taylor, J.-S. A.; Dove, A. P.; Wooley, K. L., A simple and efficient synthesis of an acid-labile polyphosphoramidate by

organobase-catalyzed ring-opening polymerization and transformation to polyphosphoester Ionomers by acid treatment. *Macromolecules* **2013**, *46*, 5141-5149.

55. Kabb, C. P.; Carmean, R. N.; Sumerlin, B. S., Probing the surface-localized hyperthermia of gold nanoparticles in a microwave field using polymeric thermometers. *Chem. Sci.* **2015**, *6*, 5662-5669.

56. Haiss, W.; Thanh, N. T.; Aveyard, J.; Fernig, D. G., Determination of size and concentration of gold nanoparticles from UV−Vis spectra. *Anal. Chem.* **2007**, *79*, 4215-4221.

57. Manson, J.; Kumar, D.; Meenan, B. J.; Dixon, D., Polyethylene glycol functionalized gold nanoparticles: The influence of capping density on stability in various media. *Gold Bull.* **2011**, *44*, 99-105.

58. Newman, J.; Blanchard, G., Formation of gold nanoparticles using amine reducing agents. *Langmuir* **2006**, *22*, 5882-5887.

59. Sun, G.; Hagooly, A.; Xu, J.; Nyström, A. M.; Li, Z.; Rossin, R.; Moore, D. A.; Wooley, K. L.; Welch, M. J., Facile, efficient approach to accomplish tunable chemistries and variable biodistributions for shell cross-linked nanoparticles. *Biomacromolecules* **2008**, *9*, 1997-2006.

60. Elsabahy, M.; Wooley, K. L., Design of polymeric nanoparticles for biomedical delivery applications. *Chem. Soc. Rev.* **2012**, *41*, 2545-2561.

61. Dai, Y.; Xu, C.; Sun, X.; Chen, X., Nanoparticle design strategies for enhanced anticancer therapy by exploiting the tumour microenvironment. *Chem. Soc. Rev.* **2017**, *46*, 3830.

62. Sun, T. M.; Zhang, Y. S.; Pang, B.; Hyun, D. C.; Yang, M. X.; Xia, Y. N., Engineered nanoparticles for drug delivery in cancer therapy. *Angew. Chem. Int. Ed.* **2014**, *53*, 12320-12364.

63. Chen, H.; Zhang, W.; Zhu, G.; Xie, J.; Chen, X., Rethinking cancer nanotheranostics. *Nat. Rev. Mater.* **2017**, *2*, 17024.

64. Wilhelm, S.; Tavares, A. J.; Dai, Q.; Ohta, S.; Audet, J.; Dvorak, H. F.; Chan, W. C. W., Analysis of nanoparticle delivery to tumours. *Nat. Rev. Mater.* **2016**, *1*, 16014.

65. Minchinton, A. I.; Tannock, I. F., Drug penetration in solid tumours. *Nat. Rev. Cancer* **2006**, *6*, 583-592.

66. Hughes, D. P. M., Novel agents in development for pediatric sarcomas. *Curr. Opin. Oncol.* **2009**, *21*, 332-337.

67. Zhou, J.; Liu, J.; Cheng, C. J.; Patel, T. R.; Weller, C. E.; Piepmeier, J. M.; Jiang, Z.; Saltzman, W. M., Biodegradable poly(amine-co-ester) terpolymers for targeted gene delivery. *Nat. Mater.* **2012**, *11* (1), 82-90.

68. McKinlay, C. J.; Waymouth, R. M.; Wender, P. A., Cell-penetrating, guanidinium-rich oligophosphoesters: Effective and versatile molecular transporters for drug and probe delivery. *J. Am. Chem. Soc.* **2016**, *138*, 3510-3517.

69. Ekladious, I.; Liu, R.; Zhang, H.; Foil, D. H.; Todd, D. A.; Graf, T. N.; Padera, R. F.; Oberlies, N. H.; Colson, Y. L.; Grinstaff, M. W., Synthesis of poly(1,2-glycerol carbonate)-paclitaxel conjugates and their utility as a single high-dose replacement for multi-dose treatment regimens in peritoneal cancer. *Chem. Sci.* **2017**, *8*, 8443-8450.

70. Schneider, C. S.; Xu, Q.; Boylan, N. J.; Chisholm, J.; Tang, B. C.; Schuster, B. S.; Henning, A.; Ensign, L. M.; Lee, E.; Adstamongkonkul, P.; Simons, B. W.; Wang, S.-Y. S.; Gong, X.; Yu, T.; Boyle, M. P.; Suk, J. S.; Hanes, J., Nanoparticles that do not adhere to mucus provide uniform and long-lasting drug delivery to airways following inhalation. *Sci. Adv.* **2017**, *3* (4), e1601556.

71. Carvalho, C. D. S.; Daum, N.; Lehr, C. M., Carrier interactions with the biological barriers of the lung: Advanced *in vitro* models and challenges for pulmonary drug delivery. *Adv. Drug Deliv. Rev.* **2014**, *75*, 129-140.

72. Chauhan, V. P.; Stylianopoulos, T.; Boucher, Y.; Jain, R. K., Delivery of molecular and nanoscale medicine to tumors: Transport barriers and strategies. *Annu. Rev. Chem. Biomol. Eng.* **2011**, *2*, 281-298.

73. Perrault, S. D.; Walkey, C.; Jennings, T.; Fischer, H. C.; Chan, W. C. W., Mediating tumor targeting efficiency of nanoparticles through design. *Nano Lett.* **2009**, *9*, 1909-1915.

74. Huang, K. Y.; Ma, H. L.; Liu, J.; Huo, S. D.; Kumar, A.; Wei, T.; Zhang, X.; Jin, S. B.; Gan, Y. L.; Wang, P. C.; He, S. T.; Zhang, X. N.; Liang, X. J., Size-dependent localization and penetration of ultrasmall gold nanoparticles in cancer cells, multicellular spheroids, and tumors *in vivo*. *Acs Nano* **2012**, *6*, 4483-4493.

75. Murgia, X.; Pawelzyk, P.; Schaefer, U. F.; Wagner, C.; Willenbacher, N.; Lehr, C.-M., Size-limited penetration of nanoparticles into porcine respiratory mucus after aerosol deposition. *Biomacromolecules* **2016**, *17*, 1536-1542.

76. Bugno, J.; Hsu, H.-J.; Pearson, R. M.; Noh, H.; Hong, S., Size and surface charge of engineered poly(amidoamine) dendrimers modulate tumor accumulation and penetration: A model study using multicellular tumor spheroids. *Mol. Pharm.* **2016**, *13*, 2155-2163.

77. Li, H.-J.; Du, J.-Z.; Liu, J.; Du, X.-J.; Shen, S.; Zhu, Y.-H.; Wang, X.; Ye, X.; Nie, S.; Wang, J., Smart superstructures with ultrahigh pH-sensitivity for targeting acidic tumor microenvironment: Instantaneous size switching and improved tumor penetration. *ACS Nano* **2016**, *10*, 6753-6761.

78. Punia, A.; Lee, K.; He, E.; Mukherjee, S.; Mancuso, A.; Banerjee, P.; Yang, N. L., Effect of relative arrangement of cationic and lipophilic moieties on hemolytic and antibacterial activities of PEGylated polyacrylates. *Int. J. Mol. Sci.* **2015**, *16*, 23867-23880.

79. Xu, Q. G.; Ensign, L. M.; Boylan, N. J.; Schon, A.; Gong, X. Q.; Yang, J. C.; Lamb, N. W.; Cai, S. T.; Yu, T.; Freire, E.; Hanes, J., Impact of surface polyethylene glycol (PEG) density on biodegradable nanoparticle transport in mucus *ex vivo* and distribution *in vivo*. *ACS Nano* **2015**, *9*, 9217-9227.

80. Diehn, M.; Cho, R. W.; Lobo, N. A.; Kalisky, T.; Dorie, M. J.; Kulp, A. N.; Qian, D.; Lam, J. S.; Ailles, L. E.; Wong, M.; Joshua, B.; Kaplan, M. J.; Wapnir, I.; Dirbas, F. M.; Somlo, G.; Garberoglio, C.; Paz, B.; Shen, J.; Lau, S. K.; Quake, S. R.; Brown, J. M.; Weissman, I. L.; Clarke, M. F., Association of reactive oxygen species levels and radioresistance in cancer stem cells. *Nature* **2009**, *458*, 780-783.

81. Estrela, J. M.; Ortega, A.; Obrador, E., Glutathione in cancer biology and therapy. *Crit. Rev. Clin. Lab. Sci.* **2006**, *43* (2), 143-81.

82. Cai, K.; He, X.; Song, Z.; Yin, Q.; Zhang, Y.; Uckun, F. M.; Jiang, C.; Cheng, J., Dimeric drug polymeric nanoparticles with exceptionally high drug loading and quantitative loading efficiency. *J. Am. Chem. Soc.* **2015**, *137*, 3458-61.

83. Pei, Q.; Hu, X.; Liu, S.; Li, Y.; Xie, Z.; Jing, X., Paclitaxel dimers assembling nanomedicines for treatment of cervix carcinoma. *J. Control. Release* **2017**, *254*, 23-33.

84. Han, X.; Chen, J.; Jiang, M.; Zhang, N.; Na, K.; Luo, C.; Zhang, R.; Sun, M.; Lin, G.; Zhang, R.; Ma, Y.; Liu, D.; Wang, Y., Paclitaxel-Paclitaxel Prodrug Nanoassembly as a Versatile Nanoplatform for Combinational Cancer Therapy. *ACS Appl. Mater. Interfaces* **2016**, *8* (49), 33506-33513.

85. Zou, J.; Zhang, F.; Zhang, S.; Pollack, S. F.; Elsabahy, M.; Fan, J.; Wooley, K. L., Poly(ethylene oxide)-block-polyphosphoester-graft-paclitaxel conjugates with acid-labile linkages as a pH-sensitive and functional nanoscopic platform for paclitaxel delivery. *Adv. Healthc. Mater.* **2014**, *3*, 441-8.

86. de Planque, M. R. R.; Aghdaei, S.; Roose, T.; Morgan, H., Electrophysiological Characterization of Membrane Disruption by Nanoparticles. *ACS Nano* **2011**, *5*, 3599-3606.

87. Leroueil, P. R.; Berry, S. A.; Duthie, K.; Han, G.; Rotello, V. M.; McNerny, D. Q.; Baker, J. R.; Orr, B. G.; Banaszak Holl, M. M., Wide varieties of cationic nanoparticles induce defects in supported lipid bilayers. *Nano Lett.* **2008**, *8*, 420-424.

88. Reis, C. P.; Neufeld, R. J.; Ribeiro, A. J.; Veiga, F., Nanoencapsulation I. Methods for preparation of drug-loaded polymeric nanoparticles. *Nanomed-nanotechnol.* **2006**, *2*, 8-21.

89. Su, L.; Zhang, W. Y.; Wu, X. L.; Zhang, Y. F.; Chen, X.; Liu, G. W.; Chen, G. S.; Jiang, M., Glycocalyx-Mimicking Nanoparticles for Stimulation and Polarization of Macrophages via Specific Interactions. *Small* **2015**, *11*, 4191-4200.

90. Lazzari, G.; Couvreur, P.; Mura, S., Multicellular tumor spheroids: A relevant 3D model for *in vitro* preclinical investigation of polymer nanomedicines. *Polym. Chem.* **2017**, *8*, 4947.

91. Friedrich, J.; Seidel, C.; Ebner, R.; Kunz-Schughart, L. A., Spheroid-based drug screen: considerations and practical approach. *Nat. Protoc.* **2009**, *4*, 309-324.

92. Mehta, G.; Hsiao, A. Y.; Ingram, M.; Luker, G. D.; Takayama, S., Opportunities and challenges for use of tumor spheroids as models to test drug delivery and efficacy. *J. Control. Release* **2012**, *164* (2), 192-204.

93. Harrison, D. J.; Geller, D. S.; Gill, J. D.; Lewis, V. O.; Gorlick, R., Current and future therapeutic approaches for osteosarcoma. *Expert Rev. Anticancer Ther.* **2018**, *18*, 39-50.

94. Hattinger, C. M.; Pasello, M.; Ferrari, S.; Picci, P.; Serra, M., Emerging drugs for high-grade osteosarcoma. *Expert Opin. Emerg. Drugs* **2010**, *15*, 615-634.

95. Janeway, K. A.; Grier, H. E., Sequelae of osteosarcoma medical therapy: A review of rare acute toxicities and late effects. *Lancet Oncol.* **2010**, *11*, 670-678.

96. Abdelaziz, H. M.; Gaber, M.; Abd-Elwakil, M. M.; Mabrouk, M. T.; Elgohary, M. M.; Kamel, N. M.; Kabary, D. M.; Freag, M. S.; Samaha, M. W.; Mortada, S. M.; Elkhodairy, K. A.; Fang, J.-Y.; Elzoghby, A. O., Inhalable particulate drug delivery systems for lung cancer therapy: Nanoparticles, microparticles, nanocomposites and nanoaggregates. *J. Control. Release* **2018**, *269*, 374-392.

97. Mastorakos, P.; da Silva, A. L.; Chisholm, J.; Song, E.; Choi, W. K.; Boyle, M. P.; Morales, M. M.; Hanes, J.; Suk, J. S., Highly compacted biodegradable DNA nanoparticles capable of overcoming the mucus barrier for inhaled lung gene therapy. *Proc. Natl. Acad. Sci. U. S. A.* **2015**, *112*, 8720-8725.

98. Richter, M. F.; Drown, B. S.; Riley, A. P.; Garcia, A.; Shirai, T.; Svec, R. L.; Hergenrother, P. J., Predictive compound accumulation rules yield a broad-spectrum antibiotic. *Nature* **2017**, *545*, 299.

99. Fisher, J. F.; Mobashery, S., Endless resistance, Endless antibiotics? *MedChemComm* **2016**, *7*, 37-49.

100. Piddock, L. J., Understanding drug resistance will improve the treatment of bacterial infections. *Nat. Rev. Microbiol.* **2017**, *15*, 639.

101. Shah, P. N.; Lin, L. Y.; Smolen, J. A.; Tagaev, J. A.; Gunsten, S. P.; Han, D. S.; Heo, G. S.; Li, Y.; Zhang, F.; Zhang, S., Synthesis, characterization, and in vivo efficacy of shell cross-

linked nanoparticle formulations carrying silver antimicrobials as aerosolized therapeutics. *ACS Nano* **2013**, *7*, 4977-4987.

102. Lim, Y. H.; Tiemann, K. M.; Heo, G. S.; Wagers, P. O.; Rezenom, Y. H.; Zhang, S.; Zhang, F.; Youngs, W. J.; Hunstad, D. A.; Wooley, K. L., Preparation and *in vitro* antimicrobial activity of silver-bearing degradable polymeric nanoparticles of polyphosphoester-block-poly (L-lactide). *ACS Nano* **2015**, *9*, 1995-2008.